Topology in SU(2) lattice gauge theory and parallelization of functional magnetic resonance imaging

Dissertation zur Erlangung des Doktorgrades der Naturwissenschaften
(Dr. rer. nat.) der Fakultät Physik der Universität Regensburg

vorgelegt von

Stefan Solbrig
aus
Regensburg

2008

Promotionsgesuch eingereicht am: 17. Mai 2008

Datum des Promotionskolloquiums: 01. Juli 2008

Die Arbeit wurde angeleitet von: Prof. Dr. Andreas Schäfer

Prüfungsausschuß:

Vorsitzender:	Prof. Dr. Ch. Strunk
1. Gutachter:	Prof. Dr. A. Schäfer
2. Gutachter:	Prof. Dr. T. Wettig
weiterer Prüfer:	Prof. Dr. I. Morgenstern

List of publications:

F. Belletti et al. “QCD on the Cell Broadband Engine.” *PoS*, LATTICE2007:039, 2007.

Falk Bruckmann et al. “Quantitative comparison of filtering methods in lattice QCD.” *Eur. Phys. J.*, A33:333–338, 2007.

Jochen Gattnar et al. “Center vortices and Dirac eigenmodes in SU(2) lattice gauge theory.” *Nucl. Phys.*, B716:105–127, 2005.

Christof Gattringer, E. M. Ilgenfritz, and Stefan Solbrig. “Cooling, smearing and Dirac eigenmodes: A comparison of filtering methods in lattice gauge theory.” 2006.

Christof Gattringer and Stefan Solbrig. “Remnant index theorem and low-lying eigenmodes for twisted mass fermions.” *Phys. Lett.*, B621:195–200, 2005.

Christof Gattringer and Stefan Solbrig. “Dependence of Dirac eigenmodes on boundary conditions for SU(2) lattice gauge theory.” *Nucl. Phys. Proc. Suppl.*, 152:284–287, 2006.

Christof Gattringer and Stefan Solbrig. “Low-lying spectrum for lattice Dirac operators with twisted mass.” *PoS*, LAT2005:127, 2006.

Stefan Solbrig et al. “Topologically non-trivial field configurations: Interplay of vortices and Dirac eigenmodes.” *PoS*, LAT2005:301, 2006.

Stefan Solbrig et al. “Smearing and filtering methods in lattice QCD - a quantitative comparison.” *PoS*, LATTICE:334, 2007.

Abstract

In this thesis, I discuss topological properties of quenched SU(2) lattice gauge fields. In particular, clusters of topological charge density exhibit a power-law. The exponent of that power-law can be used to validate models for lattice gauge fields. Instead of working with fixed cutoffs of the topological charge density, using the notion of a “watermark” is more convenient.

Furthermore, I discuss how a parallel computer, originally designed for lattice gauge field simulations, can be used for functional magnetic resonance imaging. Multi parameter fits can be parallelized to achieve almost real-time evaluation of fMRI data.

To my family.

Contents

Chapter 1

Foreword

“Topological objects in QCD” — the title of this thesis sounds quite exotic to the casual reader but intriguing to those involved in nuclear physics. As a start, I want to outline how topology in QCD fits into the framework of physics as we know it today.

The current understanding for the fundamental interactions in physics knows four fundamental forces. A full description of all those forces can fill many volumes of textbooks. I will just give a very broad overview without going into the details and potential shortcomings of the standard model.

Gravity is a long-range interaction. It is also the least understood fundamental force although the general theory of relativity gives us a excellent classical theory. It can be fully understood in the mathematical framework of Riemannian geometry. However, a comprehensive quantum theory of gravity is still not known. Several approaches exist, ranging from string theory to quantum loop gravity.

The electromagnetic interaction, frequently called Coulomb interaction, is classically described my the familiar Maxwell equations. On the quantum level, quantum electrodynamics (QED) provides a satisfying theory. QED was and is extremely successful in making predictions measurable quantities with high precision, like for the Lamb shift. Therefore, most physicists believe quantum field theories are generally well suited to describe fundamental interactions. All interaction of particles with electric charge are described by this theory. Like Gravity, the Coulomb interaction is a long-range interaction since its gauge particle, the photon, is massless. Most every-day phenomena, like chemical reactions, friction, heat transport and so on can, in principle, be described by QED.

The weak nuclear interaction is described by the GWS theory. It is named after Glashow, Weinberg and Salam who described this theory in 1967 and were awarded the Nobel Price in physics in 1979. This theory is also a gauge field theory, with $SU(2)$ as gauge group. Since its gauge group is not Abelian, it is quite different from QED. All spin-1/2 particles interact via the weak nuclear interactions. Since the gauge particles acquire a mass, this is a short-range interaction. The GWS theory explains nuclear decay phenomena like the β-decay.

The forth force is the strong nuclear interaction. Quantum chromo-dynamics, QCD for short, is most widely used to describe it. Like the GWS theory, it is a non-Abelian gauge field theory, with $SU(3)$ being its gauge group. The gauge particles, called gluons, interact with all particles that have color charge, that is only the quarks. The strong nuclear interaction is responsible for binding the quarks in to hadrons like the proton or the neutron and for binding those together into atomic nuclei. The strong nuclear interaction is also a short-range force, due to an effect called “confinement.” This term describes the effect that only color-neutral states can be observed directly. Since the gauge group of the strong interaction is non-Abelian, gauge fields can have a nontrivial topology. These topological objects may be connected to confinement, a property that makes QCD different from the other fundamental forces.

Chapter 2

Introduction

2.1 Gauge fields

Before I go into details about topology, I will briefly review gauge theories. Three of the fundamental forces can be described by gauge theories, and two of them – the weak and the strong nuclear interaction – use theories based on non-Abelian Yang-Mills theories.

2.1.1 Lie groups and Lie algebras

The main ingredient to non-Abelian Yang-Mills theories are Lie groups and their algebras. There is a wealth of literature about Lie groups. In the next section, I will pick out those facts that are relevant for a discussion of topology. In the following, "d" stands for the exterior derivative.

The general definition of a Lie group G is a manifold with a group structure. The tangent space to the neutral element $\mathbb{1} \in G$, that is $T_{\mathbb{1}}G$, is called the Lie algebra. A *one parameter subgroup* of a Lie group is a map g

$$\begin{aligned}&g : \mathbb{R} \to G \qquad t \mapsto g(t) \in G\\&\text{that is a differentiable homomorphism, i.e.,}\\&g(t+u) = g(t)\, g(u) = g(u)\, g(t)\end{aligned} \tag{2.1}$$

Take now the derivative of that equation with respect to u and let $u = 0$. We get:

$$\mathrm{d}\, g(t) = g(t)\, \mathrm{d}\, g(0) \tag{2.2}$$

If the g are matrices, we can solve Eq. (2.2):

$$g(t) = \exp\Big(t\, g(0)\Big) \tag{2.3}$$

If our Lie group is a matrix group, the exponential map $\exp(X)$ is also written as e^X. Now that Eq. (2.3) gives us a tool to map tangent vectors to our Lie group on the Lie group itself, we consider the special case where $g(0) = \mathbb{1}$. In that case, the equation reads $g(t) = e^{tX}$ with $X \in T_{\mathbb{1}}G$, i.e., X is a vector in the Lie algebra. This tells us that $e^{tX} \in G$ for any X in the Lie algebra and any $t \in \mathbb{R}$.

The really interesting question is the reverse: For a *given* $g \in G$, can we find a X in the Lie algebra and a $t \in \mathbb{R}$, such that $g = e^{tX}$? One can indeed find groups where that statement does not hold, for example the group $Sl(2, \mathbb{R})$ [1]. However, there is a theorem [1], that for any *compact* Lie group, it holds that

$$\begin{aligned}\exp : T_{\mathbb{1}}G &\longrightarrow G\\ X &\longmapsto e^X\end{aligned} \tag{2.4}$$

is a map that is *onto*, i.e., that covers all of G. In other words, for a given g in a compact Lie group G, we can always find a X in the Lie algebra such that $g = e^X$. Furthermore, it can be shown that the groups $SU(2)$ and $SU(3)$ are indeed compact. This explains the common term "generators" for the basis vectors of the Lie algebra: If the exponential map is onto, then every element in the group can be "generated" from the algebra via the exponential map.

As a side remark, I want to note that compactness of the Lie group is a sufficient criterion for the exponential map to be onto. However, compactness is not a necessary criterion. The group $L_+^\uparrow$ of proper orthochronous Lorentz transformations is not compact, but the exponential map for $L_+^\uparrow$ *is* onto.

2.1.2 The adjoint representation

We have to distinguish between the adjoint representation of the group and the adjoint representation of the algebra. The adjoint representation Ad is defined as

$$\begin{array}{rcccc} Ad & : & G & \longrightarrow & Gl(\mathfrak{g}) \\ & & g & \longmapsto & \mathrm{d}(g\,\cdots\,g^{-1})_{\mathbb{1}} \end{array} \tag{2.5}$$

Note it is this map that is called the adjoint representation, with $Gl(\mathfrak{g})$ being the linear maps from $\mathfrak{g}$ onto itself. It can be easily seen from the above equation, that the adjoint representation is just the trivial group i.e., the group $\{\mathbb{1}\}$) if G is Abelian. For a single $g \in G$ we get a map:

$$\begin{array}{rcccc} Ad(g) & : & \mathfrak{g} & \xrightarrow{\text{lin.}} & \mathfrak{g} \\ & & X & \longmapsto & \mathrm{d}(g\cdots g^{-1})_{\mathbb{1}}\,X \end{array} . \tag{2.6}$$

Now if G is already a matrix group, then g is already a linear map, and $\mathrm{d}\,g = g$. Then we can write

$$Ad(g)X = \frac{\mathrm{d}}{\mathrm{d}\,s}\left(g\,e^{sX}\,g^{-1}\right)\Big|_{s=0} = gXg^{-1}\ .$$

Thus,

$$\begin{array}{rcccc} Ad(g) & : & \mathfrak{g} & \xrightarrow{\text{lin.}} & \mathfrak{g} \\ & & X & \longmapsto & gXg^{-1} \end{array}$$

and

$$\begin{array}{rcccc} Ad & : & G & \longrightarrow & Gl(\mathfrak{g}) \\ & & g & \longmapsto & g\cdots g^{-1} \end{array}$$

where g acts on X via the ordinary matrix multiplication.

Since $Ad(g)$ is a linear map $\mathfrak{g} \to \mathfrak{g}$, we can identify $\mathfrak{g}$ with $\mathbb{R}^n$ (where n is the dimension of the group) and determine the matrix h so that the following diagram commutes:

$$\begin{tikzcd}
\mathfrak{g} \arrow[r, "Ad(g)", "\text{lin.}"'] \arrow[d, "\text{canonical}"'] & \mathfrak{g} \arrow[d, "\text{canonical}"] \\
\mathbb{R}^n \arrow[r, "h", "\text{lin.}"'] & \mathbb{R}^n
\end{tikzcd}$$

with

$$\begin{array}{rcccc} h & : & \mathbb{R}^n & \xrightarrow{\text{lin.}} & \mathbb{R}^n \\ & & \boldsymbol{x} & \longmapsto & h\boldsymbol{x} \end{array}$$

begin the ordinary matrix-vector multiplication. In the above diagram, “canonical” simply means that the i-th basis vector in $\mathfrak{g}$ is mapped to the i-th basis vector in $\mathbb{R}^n$. This can be done in the following way: Choose a scalar product $\langle\cdot,\cdot\rangle$ on $\mathfrak{g}$, and an orthonormal basis $\boldsymbol{E}$ in $\mathfrak{g}$. Then standard linear algebra tells us, that gE_sg^{-1} is the image of the s-th basis vector, and $\langle E_r,\, gE_sg^{-1}\rangle$ is the r-th element of this image. In other words:

$$\Big(h\Big)_{rs} = \Big\langle E_r,\, gE_sg^{-1}\Big\rangle\ . \tag{2.7}$$

From a physicist’s viewpoint, h is the adjoint representation of g. However, mathematically speaking this not quite correct, since the map Ad is the representation, not h. To be more precise, we may say that h is the matrix showing how g acts on $\mathfrak{g}$ via the adjoint representation.

The map Ad induces a map $Ad_* : \mathfrak{g} \to gl(\mathfrak{g})$ via the differential. We will write ad for Ad_* for brevity. This means

$$\begin{array}{rccc} ad : & \mathfrak{g} & \longrightarrow & gl(\mathfrak{g}) \\ & A & \longmapsto & \frac{\mathrm{d}}{\mathrm{d}\,t}\Big|_{t=0} Ad\left(e^{tA}\right) \end{array} \quad .$$

and

$$\begin{array}{rccc} ad(A) : & \mathfrak{g} & \xrightarrow{\text{lin.}} & \mathfrak{g} \\ & X & \longmapsto & \frac{\mathrm{d}}{\mathrm{d}\,t}\Big|_{t=0} Ad\left(e^{tA}\right)\, X \end{array}$$

It can be shown that

$$Ad\left(e^{A}\right) = e^{ad(A)} \; .$$

Again, if G is a matrix group, this map is easy to compute. Just write $g = e^{tA}$ with $A \in \mathfrak{g}$ and $t \in \mathbb{R}$. This is always possible, since we are working in the vicinity of the identical map. Then:

$$ad(A)X = \frac{\mathrm{d}}{\mathrm{d}\,t}\left(e^{tA}\,X\,e^{-tA}\right)\Big|_{t=0} = [A,\, X] \; .$$

with $[\cdot, \cdot]$ being the ordinary commutator. In other words:

$$\begin{array}{rccc} ad(A) : & \mathfrak{g} & \xrightarrow{\text{lin.}} & \mathfrak{g} \\ & X & \longrightarrow & [A,\, X] \end{array} \quad .$$

$$\begin{array}{rccc} ad : & \mathfrak{g} & \longrightarrow & gl(\mathfrak{g}) \\ & A & \longmapsto & [A, \cdot] \end{array}$$

Again, $ad(A)$ is a linear map, so when we identify $\mathfrak{g}$ with $\mathbb{R}^n$, we will get the matrix representing $ad(A)$. This can, again, be done by choosing a orthonormal basis in $\mathfrak{g}$ and choosing a suitable scalar product. Then,

$$\Big(B\Big)_{rs} = \langle E_r,\, [A,\, E_s]\rangle \tag{2.8}$$

Since this is a linear map, it is sufficient to know how $ad(A)$ operates on the basis vectors $\boldsymbol{E}$ of $\mathfrak{g}$ in order to fully know how the map operates. But $\langle E_i,\, [E_j,\, E_k]\rangle$ can be expressed as $\langle E_i,\, \kappa^l_{jk} E_l\rangle$ with some coefficients κ^l_{kj} that we will call the *structure constants.* Because the E_i already form an orthonormal basis, we get

$$\Big\langle E_i,\, [E_j,\, E_k]\Big\rangle = \Big\langle E_i,\, \kappa^l_{jk} E_l\Big\rangle = \kappa^l_{jk}\Big\langle E_i,\, E_l\Big\rangle = \kappa^l_{jk}\,\delta_{il} = \kappa^i_{jk}$$

with κ^i_{jk} being the structure constants of the Lie algebra. This is also a formula how to compute the structure constants if we already have an orthonormal basis of $\mathfrak{g}$. In other words,

$$\Big(ad(E_j)\Big)_{ik} = \Big(\kappa^{\,\cdot}_{j\,\cdot}\Big)^i_k = \kappa^i_{jk} \qquad .$$

The physicists' convention for groups $SU(N)$ and their algebras differs slightly from the convention used in mathematical texts. Since the algebras $\mathfrak{su}(N)$ are the anti-Hermitean

$N \times N$ matrices, the convention is to pull out a factor i, use an exponential map of the form

$$\begin{aligned} \exp : \mathfrak{su}(N) &\longrightarrow SU(N) \\ iA &\longmapsto e^{iA} \end{aligned} \tag{2.9}$$

with $A = \sum_a c_a T^a$, $c_a \in \mathbb{R}$ and the T^a being Hermitean. The T^a are then called the generators of the group $SU(N)$, but actually iT^a is a vector in the Lie algebra. The structure constants f are then defined via

$$[T^a, T^b] = i\, f_{abc}\, T^c \quad \text{with} \quad f_{abc} \in \mathbb{R} \tag{2.10}$$

I will now demonstrate the general formulas above on some useful examples for the group $SU(2)$. A basis for $\mathfrak{su}(2)$ can be constructed using the Pauli matrices. Denoting the generators with T^a,

$$T^1 = \frac{1}{2}\sigma_1 = \frac{1}{2}\begin{pmatrix} 0 & 1 \\ 1 & 0 \end{pmatrix} \qquad T^2 = \frac{1}{2}\sigma_2 = \frac{1}{2}\begin{pmatrix} 0 & -i \\ i & 0 \end{pmatrix} \qquad T^3 = \frac{1}{2}\sigma_3 = \frac{1}{2}\begin{pmatrix} 1 & 0 \\ 0 & -1 \end{pmatrix} \tag{2.11}$$

Note that the generators T^a are not in $\mathfrak{su}(2)$, but $i\,T^a$ are. As the scalar product, we use:

$$\begin{array}{ccccc} \langle\cdot,\cdot\rangle \;:\; \mathfrak{su}(2) \times \mathfrak{su}(2) & \longrightarrow & \mathbb{R} & & . \\ X,\, Y & \longmapsto & -2\,\mathrm{tr}\,(X\,Y) & \text{respective} & \\ iA,\, iB & \longmapsto & 2\,\mathrm{tr}\,(A\,B) & & \end{array} \tag{2.12}$$

The structure constants are given by:

$$\begin{aligned} &\Big[T^a,\, T^b\Big] = i\epsilon_{abc}T^c, \qquad \Big[iT^a,\, iT^b\Big] = -\epsilon_{abc}\, iT^c = -\kappa_{ab}^{c}\, iT^c \\ &f_{ijk} = \epsilon_{ijk} = -\kappa_{ab}^{c} \end{aligned} \tag{2.13}$$

The formula how to transform a "link variable" U in the fundamental representation to the matrix W in the adjoint representation is:

$$\Big(W\Big)_{ij} = -2\,\mathrm{tr}\left(\frac{i}{2}\sigma_i\, U\, \frac{i}{2}\sigma_j\, U^\dagger\right) = \frac{1}{2}\,\mathrm{tr}\left(\sigma_i\, U\, \sigma_j\, U^\dagger\right) \;. \tag{2.14}$$

Here, we have used Eq. (2.7) and the scalar product given in Eq. (2.12).

The formula how to translate fundamental gauge fields A in the continuum to the adjoint representation B is:

$$i\Big(B\Big)_{ij} = -2\,\mathrm{tr}\left(\frac{i}{2}\sigma_i\, \left[iA,\, \frac{i}{2}\sigma_j\right]\right) = \frac{i}{2}\,\mathrm{tr}\left(\sigma_i\, [A,\, \sigma_j]\right) \;. \tag{2.15}$$

We used Eq. (2.8) and the scalar product Eq. (2.12). Like in most physics textbooks, $iA \in \mathfrak{su}(2)$ such that A is Hermitean.

Some examples:

$$\begin{aligned} &ad(i\sigma_3) = ad\left(i\begin{bmatrix} 1 & 0 \\ 0 & -1 \end{bmatrix}\right) = \Big(f_3\Big)_i^{\;k} = \epsilon_{ik3} = \\ &2\begin{bmatrix} \epsilon_{113} & \epsilon_{123} & \epsilon_{133} \\ \epsilon_{213} & \epsilon_{223} & \epsilon_{233} \\ \epsilon_{313} & \epsilon_{323} & \epsilon_{333} \end{bmatrix} = \begin{bmatrix} 0 & 2 & 0 \\ -2 & 0 & 0 \\ 0 & 0 & 0 \end{bmatrix} \end{aligned}$$

$$Ad\left(\begin{bmatrix} \exp(i\theta) & 0 \\ 0 & \exp(-i\theta) \end{bmatrix}\right) = \begin{bmatrix} \cos(2\theta) & \sin(2\theta) & 0 \\ -\sin(2\theta) & \cos(2\theta) & 0 \\ 0 & 0 & 1 \end{bmatrix}$$

More generally, it can be shown that the adjoint representation of $SU(2)$ is isomorphic to SO(3), i.e., $Ad_{SU(2)} \cong SO(3)$, and that the map $Ad\ : SU(2) \to SO(3)$ is onto and $2:1$. Thus, $SU(2)$ is the 2-fold cover of the rotations in $\mathbb{R}^3$, so $SU(2)$ it is also called $Spin(SO(3))$. The fact that the map $Ad\ : SU(2) \to SO(3)$ is $2:1$ can also be understood in the following way: $SU(2) \cong S^3$, because any $g \in SU(2)$ can be written as

$$g = \begin{pmatrix} a & -\bar{b} \\ b & \bar{a} \end{pmatrix} \text{ with } a\bar{a} + b\bar{b} = 1 \ .$$

On the other hand, $SO(3)$ is isomorphic to re projective space $\mathbb{R}P^3$, which is the 3-sphere S^3 with antipodal points identified. This can be proven by using Cayley's map [2]

$$\begin{array}{rcl} C\ :\ \mathbb{R}^{n+1} & \longrightarrow & SO(m) \\ \xi & \longmapsto & B = (\xi_0 \mathbb{1} - \boldsymbol{\xi A})^{-1} (\xi_0 \mathbb{1} + \boldsymbol{\xi A}) \end{array}$$

with $n = m(m-1)/2$ and $\boldsymbol{A}$ being a basis for the $m \times m$ antisymmetric matrices. We see that every line $(\xi_0, \boldsymbol{\xi})$ is mapped to the same line in $\mathbb{R}^{n+1}$, since $C(\mu\xi_0, \mu\boldsymbol{\xi}) = C(\xi_0, \boldsymbol{\xi})$ for any $\mu \in \mathbb{R}\backslash 0$. (Another map is given in [3].)

2.1.3 Definitions

For a $\mathfrak{su}(N)$ gauge field, we define:

The gauge field as a map from the spacetime V to the algebra of the gauge group:

$$\begin{aligned} A : V &\longrightarrow \mathfrak{su}(N) \\ x &\longmapsto iA(x) \text{ with } \quad iA(x) \in \mathfrak{su}(N) \end{aligned} \tag{2.16}$$

The gauge field can be expressed in terms of the generators of the algebra:

$$A(x) = A^a(x)\, T^a, \quad \text{ with } A^a(x) \in \mathbb{R} \quad \text{ and } T^a \in \mathfrak{su}(N) \tag{2.17}$$

$$T^a \text{ is a basis vector in } \mathfrak{su}(N)\text{, a so called } \textit{generator} \text{ of the group.} \tag{2.18}$$

The covariant derivative is defined as:

$$D_\mu = \partial_\mu - iA_\mu \tag{2.19}$$

The field strength tensor is defined as:

$$\begin{aligned} F_{\mu\nu} &= i\,[D_\mu,\, D_\nu] \quad \text{ where } [\cdot,\cdot] \text{ denotes the commutator.} \\ &= \partial_\mu A_\nu - \partial_\nu A_\mu - i[A_\mu,\, A_\nu] \\ &= \partial_\mu A^a_\nu T^a - \partial_\nu A^a_\mu T^a - iA^a_\mu A^b_\nu [T^a,\, T^b] \\ &= \partial_\mu A^a_\nu T^a - \partial_\nu A^a_\mu T^a + f^{abc} T^c A^a_\mu A^b_\nu \\ &= \partial_\mu A^a_\nu T^a - \partial_\nu A^a_\mu T^a + f^{abc} A^b_\mu A^c_\nu T^a \end{aligned} \tag{2.20}$$

The dual field strength tensor is defined as:

$$\widetilde{F}_{\mu\nu} = \frac{1}{2}\epsilon_{\mu\nu\alpha\beta} F_{\alpha\beta} \tag{2.21}$$

2.2 Topology of gauge fields

2.2.1 The Brouwer degree of a map

At first, we want to introduce the concept of the *Brouwer Degree* of a map. For a map $\Phi: \; M \longrightarrow N$ between two closed oriented manifolds M and N of dimension n, the Brouwer degree is defined as

$$\deg(\Phi) = \int_M \Phi^{\,*}\,\omega = \int_{\Phi(M)} \omega \tag{2.22}$$

for a normalized n-form ω on N, that is for a form that satisfies

$$\int_N \omega = 1 \tag{2.23}$$

Here, the star * denotes the pull-back. In addition, it can then also be shown that the Brouwer degree can be rewritten as

$$\deg(\Phi) = \sum_{x \in \Phi^{-1}(y)} \operatorname{sign} \Phi(x) \tag{2.24}$$

Here, $y \in N$ is a regular value, x is its preimage, and sign is ± 1, depending if $\Phi_* : T_x M \rightarrow T_y N$ is orientation preserving or not. This definition does not depend on the choice of y, as long as y is a regular value. Details about the proofs can be found in [4]. From Eq. (2.24) we see immediately that the Brouwer degree $\deg(\Phi)$ is indeed an integer and that the definition of the Brouwer degree is independent of ω. Since $\deg(\Phi)$ maps a smooth function Φ to an integer, any continuous change to Φ cannot change the Brouwer degree of Φ. This means, that the degree of Φ only depends on the topological properties of Φ.

Let me give the simplest example of a function with a nontrival Brouwer degree, or winding number as it is also called. Suppose we have a map

$$\begin{aligned} U(1) &\longrightarrow U(1) \\ e^{it} &\longmapsto e^{n\,it} \quad \text{with} \quad n \in \mathbb{N} \end{aligned} \tag{2.25}$$

The preimage is covered n times by the image. That is, the regular point $e^{\pi i}$ has the points $e^{\frac{\pi}{n}i + \frac{2m}{n}i}$ with $m \in \{0,\, 1,\, \dots\, n-1\}$ as preimages. The above function preserves the orientation, and thus its Brouwer degree is n. This also illustrates the meaning of the term “winding number.” The image wraps n times around the preimage.

2.2.2 The group SU(2)

We will use the gauge group $SU(2)$ as a toy model for the QCD gauge group $SU(3)$ throughout this work. It is the group of special unitary 2×2 matrices, that is all complex 2×2 matrices U that fulfill $U^{-1} = U^\dagger$ and $\det(U) = 1$. The algebra $\mathfrak{su}(2)$ are the traceless, complex, anti-Hermitean 2×2 matrices. The group $SU(2)$ can be mapped to the 3-sphere S^3 in the following way:

$$\begin{gathered} U \longrightarrow S^3 \\ n_0 \mathbb{1} + \sum_{i=1}^{3} n_i \sigma_1 \longmapsto (n_0,\, n_1,\, n_2,\, n_3) \\ \text{with } n_0, n_i \in \mathbb{R} \text{ and } n_0^2 + n_1^2 + n_2^2 + n_3^2 = 1 \end{gathered} \tag{2.26}$$

Here, $\mathbb{1}$ denotes the unit matrix and σ_i are the Pauli matrices. It can be shown that is map is 1:1 and differentiable. Thus, since the 3-Sphere is a 3-dimensional compact manifold,

$SU(2)$ is also a 3-dimensional manifold. Manifolds with a group structure are called Lie Groups. I want to mention here, that any $U \in SU(2)$ can be expressed as $U = e^A$, were $A\mathfrak{su}(2)$ since $SU(2)$ is compact. That is, any matrix U in the gauge group $SU(2)$ can be written as the exponential of an element of the algebra. This is true for all compact Lie groups.

2.2.3 Winding number or topological charge of a gauge field

Suppose our gauge field had finite support. Then one can always find a 3-sphere of finite radius that encloses the support of the gauge field. The gauge field outside the 3-sphere is that of a free field, i.e., it is some constant gauge field $Y \in \mathfrak{su}(2)$. Physical gauge fields should have vanishing field strength at large distances. Therefore, the gauge field inside the 3-sphere must approach pure gauge on the boundary, i.e., on the 3-sphere. Pure gauge means that $X(x) = U^{-1}(x)\,\mathrm{d}\,U(x)$ where $X(x) \in \mathfrak{su}(2)$ and $x \in S^3$. However, there is a transition function

$$\begin{aligned} g : S^3 &\longrightarrow SU(2) \\ x &\longmapsto g(x) \end{aligned} \tag{2.27}$$

that maps the gauge fields on the 3-sphere to a constant via $Y = g(x)\,X(x)\,g^{-1}(x)$. The Brouwer degree of the transition is the winding number of the instanton. The same setting can be generalized to gauge fields that approach pure gauge at infinity by mapping $\mathbb{R}^4 \cup \infty \to S^4$.

It can also be proven that the Brouwer degree can be written via an integral over the field strength. The proof can be found in [5]. For an gauge field A with $iA \in \mathfrak{su}(2)$, the winding number Q can be computed via

$$Q(A) = \int_V \frac{1}{16\pi^2}\,\mathrm{tr}\sum_{\mu,\nu} F_{\mu\nu}(x)\,\widetilde{F}_{\mu\nu}(x)\;\,\mathrm{d}^4\,x \tag{2.28}$$

with $F_{\mu\nu}(x)$ being the field strength tensor and $\widetilde{F}_{\mu\nu}(x)$ being its dual. I want to stress again that the degree of the gauge field as given in Eq. (2.28) is an integer, although it is the integral of a smooth function of A over the whole space time volume V. The term *topological charge* for the winding number of a gauge field comes from the fact that Q does not change under smooth transformations of the gauge field. Conserved quantities are conventionally called charges.

In anticipation of a result I will derive later, let me state the following: The topological charge of a gauge field is equivalent to the index of the Dirac operator. This deep connection to quantum field theory is not apparent. To make it clearer, I will now discuss the Lagrangian of QCD in the continuum and its symmetries. As we saw from Eq. (2.27) and Eq. (2.28), I assumed that the gauge fields live in a 4-dimensional space and that their field strength vanishes at infinity. This can only happen in Euclidean spacetime. In Minkowski space, the gauge fields will propagate and be present for all times. We will later see that the use of Euclidean spacetime is immensely useful when running numerical simulations. I will therefore use Euclidean spacetime throughout this work.

2.3 The QCD Lagrangian

The main ingredient to any relativistic field theory is the Dirac operator. It is simply defined as

$$\not{D} = \gamma_\mu \left(\partial_\mu - iA_\mu\right) \tag{2.29}$$

with A being a gauge field and γ_μ being the familiar gamma-matrices. They fulfill the relation $\{\gamma_\mu, \gamma_\nu\} = 2\delta_{\mu\nu}\mathbb{1}$.

Since we are only interested in pure gauge fields, we do not include a mass term in our Lagrangian. The Lagrangian of massless QCD for two flavors (up and down quarks) is given by:

$$\mathcal{L}_0^{\mathsf{ferm}}(x) \;=\; \bar{\psi}(x)\gamma_\mu \left(\partial_\mu \;-\; iA_\mu^a(x)\, T^a\right)\mathbb{1}\psi(x) \quad , \tag{2.30}$$

and the quark fields have two flavor components which we denote explicitly as

$$\psi(x) \;=\; \begin{pmatrix} u(x) \\ d(x) \end{pmatrix} \quad .$$

Here u and d are spinors for the up and down quarks and $\mathbb{1}$ is the unit matrix in flavor space. It is not difficult to see that the Lagrangian is invariant under the following four global transformations:

$$\psi(x) \to e^{-i\theta_i\tau_i}\psi(x) \qquad \bar{\psi}(x) \to \bar{\psi}(x)e^{+i\theta_i\tau_i} \tag{2.31a}$$

$$\psi(x) \to e^{-i\theta\mathbb{1}_f}\psi(x) \qquad \bar{\psi}(x) \to \bar{\psi}(x)e^{+i\theta\mathbb{1}_f} \tag{2.31b}$$

$$\psi(x) \to e^{-i\theta_i\tau_i\gamma_5}\psi(x) \qquad \bar{\psi}(x) \to \bar{\psi}(x)e^{-i\theta_i\tau_i\gamma_5} \tag{2.31c}$$

$$\psi(x) \to e^{-i\theta\mathbb{1}_f\gamma_5}\psi(x) \qquad \bar{\psi}(x) \to \bar{\psi}(x)e^{-i\theta\mathbb{1}_f\gamma_5} \tag{2.31d}$$

In these equations θ_i are real numbers, $\tau_i = \frac{1}{2}\sigma_i$ with $\sigma_i,\ i = 1, 2, 3$ being the Pauli matrices and $\mathbb{1}_f$ being the unit matrix in flavor space. It is important to note that τ_i and $\mathbb{1}_f$ operate in *flavor* space, not in color space. This means that the τ_i matrices mix up and down quarks but do not affect the individual spinors or their color components. These four global symmetries have the following interpretation:

Isospin symmetry, Eq. (2.31a) is the Isospin symmetry. In nature, this is only an approximate symmetry since the u and d quarks have a small but non-vanishing mass.

Baryon number conservation, Eq. (2.31b) corresponds to baryon number conservation. This symmetry is also observed in nature, with small corrections due to the weak interaction.

Chiral vector symmetry, Eq. (2.31c) is not observed in nature. It is spontaneously broken and the pions (π^+, π^-, π^0) are the Goldstone bosons corresponding to this broken symmetry. The pions are light, but not massless, as the Goldstone theorem would require, but since Eq. (2.31c) is only an exact symmetry for *massless* QCD, we don't expect the pions to be massless. The small pion mass is simply an effect of the non-vanishing up- and down-quark masses.

Chiral scalar symmetry, Eq. (2.31d) is not observed in nature either. Yet, there is no light particle that could be the Goldstone boson corresponding to this symmetry. The only particle with the right quantum numbers – the η' – is much to heavy. Thus, this symmetry must be broken explicitly by quantum effects. We will later see that quantum field configurations with non-trivial topology do break this symmetry explicitly.

Figure 2.1: The anomaly can be evaluated through the triangle diagrams. They represent the axial current $j_{5\mu}$ coupling to an external field.

2.4 The Anomaly

I will now describe how to determine the explicit breaking of the chiral scalar symmetry of Eq. (2.31d) and how this symmetry breaking is related to topology.

We define the chiral current $j_{\mu 5}$ corresponding to Eq. (2.31d) as

$$j_{\mu 5}(x) \equiv \bar{\psi}(x)\gamma_\mu\gamma_5 \mathbb{1}_f \psi(x) \tag{2.32}$$

where again $\mathbb{1}_f$ is the unity matrix in flavor space. Since the chiral scalar symmetry is explicitly broken, the associated current Eq. (2.32) needs not to be conserved. We will call the divergence of that current the *anomaly function* $\mathfrak{A}$:

$$\mathfrak{A}[A](x) \equiv \partial_\mu j_{\mu 5} \tag{2.33}$$

In the above function, $\mathfrak{A}$ is a functional of the gauge field $A(x)$ as we will shortly see. It can be shown [6] that the lowest order contribution to the anomaly function come form triangle diagrams as shown in Figure 2.1.

The axial anomaly can be calculated in a number of ways. One way is to explicitly evaluate the triangle diagrams shown in Fig. 2.1.

2.4.1 Transformation of the path integral measure

Another way to derive the axial anomaly is via chiral transformations of the path integral measure. I want to remind that fermions in quantum field theory are described by Grassmann (anti-commuting) numbers. The standard conventions for such numbers can be found in most textbooks on quantum field theory, e.g., [7] or in [8].

The approach used here follows the method used by Fujikawa [9, 10] to prove the Atiyah-Singer Index Theorem [11].

We define our Grassmann functions $\psi(x)$

$$\begin{aligned} \psi(x) &= \sum_n a_n \langle x|n\rangle \\ \bar{\psi}(x) &= \sum_m \langle m|x\rangle \bar{b}_m \end{aligned}$$

with a_n and $\bar{b}_m$ being independent Grassmann numbers and $\langle x|n\rangle = \phi_n(x)$ being an eigenfunction of the Dirac operator.

Then these functions form a complete set:

$$\begin{aligned} \sum_n \langle y|n\rangle \langle n|x\rangle &= \delta(y-x) \\ \int \mathrm{d}^4x \, \langle m|x\rangle \langle x|n\rangle &= \delta_{m\,n} \end{aligned}$$

The path integral measure then can be expressed as:

$$\begin{aligned}[\mathcal{D}\bar{\psi}]\ [\mathcal{D}\psi] &= \left(\det\langle m|x\rangle \det\langle x|n\rangle\right)^{-1} \times \prod_n \mathrm{d}a_n \prod_m \mathrm{d}\bar{b}_m \\ &= \left(\det\langle n|n\rangle\right)^{-1} \prod_n \mathrm{d}a_n \mathrm{d}\bar{b}_n \\ &= \prod_n \mathrm{d}a_n \mathrm{d}\bar{b}_n\end{aligned}$$

The next step is to make an infinitesimal chiral transformation $\psi(x) \to \psi'(x)$

$$\begin{aligned}\psi'(x) &= \sum_n a'_n \phi(x) \\ \psi'(x) &= \left(\mathbb{1} + i\beta(x)\gamma_5\right)\psi(x) \\ &= \left(\mathbb{1} + i\beta(x)\gamma_5\right)\sum_m a_m \phi_m(x)\end{aligned}$$

Eigenfunctions ϕ_k are orthonormal, so from

$$\int \mathrm{d}^4x\ \phi_n^\dagger(x)\psi'(x) \ = \ a'_n$$

it follows that

$$a'_n \ = \ \sum_m c_{nm} a_m$$

with

$$c_{nm} \ = \ \delta_{mn} \ + \ i\int \mathrm{d}^4x\,\beta(x)\,\phi_n^\dagger(x)\,\gamma_5\,\phi_m(x)$$

and

$$\bar{b}'_m \ = \ \sum_n c_{mn}\bar{b}_n$$

We can now write down the transformation of the measure. Let the matrix C be the matrix with the elements c_{nm}. Since a_n and $\bar{b}_m$ are Grassmann numbers, the $\det C$ appears in the denominator.

$$\begin{aligned}\prod_n \mathrm{d}a'_n &== (\det C)^{-1} \prod_n \mathrm{d}a_n \\ \prod_m \mathrm{d}\bar{b}'_m &= (\det C)^{-1} \prod_m \mathrm{d}\bar{b}_m\end{aligned}$$

It follows that the path integral measure transforms according to

$$\begin{aligned}[\mathcal{D}\bar{\psi}']\,[\mathcal{D}\psi'] &= (\det C)^{-2}\,[\mathcal{D}\psi]\,[\mathcal{D}\bar{\psi}] \\ &=: \mathcal{J}[\beta]\,[\mathcal{D}\psi]\,[\mathcal{D}\bar{\psi}] \qquad .\end{aligned}$$

The matrix $\mathcal{J}[\beta]$ is the Jacobian of the transformation.

Note that because $\det C \;=\; e^{\mathrm{Tr}\ln C}$ and $\ln(1+\beta) \;=\; \beta + \mathcal{O}(\beta^2)$. Neglecting terms of $\mathcal{O}(\beta^2)$, we can approximate the Jacobian $\mathcal{J}[\beta]$:

$$\begin{aligned} \mathcal{J}\,[\beta] \;&=\; (\det C)^{-2} \;=\; e^{-2\mathrm{Tr}\;\ln C} \\ &= \exp\left\{-2\mathrm{Tr}\;\ln\left(\delta_{mn} \;+\; i\int \mathrm{d}^4x\,\beta(x)\,\phi_n^\dagger(x)\,\gamma_5\,\phi_n(x)\right)\right\} \\ &= \exp\left\{-2\mathrm{Tr}\;i\int \mathrm{d}^4x\,\beta(x)\,\phi_n^\dagger(x)\,\gamma_5\,\phi_n(x)\right\} \\ &\neq \exp\left\{-2i\int \mathrm{d}^4x\beta(x)\sum_n \phi_n^\dagger(x)\,\gamma_5\,\phi_n(x)\right\} \end{aligned}$$

So why is the last step in the above calculation not valid? On the one hand,

$$\mathrm{Tr}\;\gamma_5 \;=\; 0$$

but on the other hand,

$$\sum_n \phi_n^\dagger(x)\phi_n(x) \;=\; \delta(0)$$

At this point, we see that we have to introduce some kind of regulator. Obviously, we have to this in a gauge invariant way. Less obviously, we have to this in a way that provides a special treatment for the zero-modes of the Dirac operator, i.e. for the eigenfunctions with $\not{D}\phi \;=\; 0$. The reason is simply that

$$\int \mathrm{d}^4x\;\phi_k^\dagger(x)\,\gamma_5\,\phi_k(x) \;=\; \begin{cases} 0 & \text{if} \quad \lambda_k \neq 0 \\ \pm 1 & \text{if} \quad \lambda_k = 0 \end{cases}$$

A good choice is to add a Gaussian weight to eigenfunctions, using their eigenvalue as weight:

$$\begin{aligned} &\sum_n \phi_n^\dagger(x)\,\gamma_5\,\phi_n(x) = \\ &\qquad\qquad = \lim_{M\to\infty}\sum_n \phi_n^\dagger(x)\,\gamma_5\,e^{+\lambda_n^2/M^2}\,\phi_n(x) \\ &\qquad\qquad = \lim_{M\to\infty}\sum_n \phi_n^\dagger(x)\,\gamma_5\,e^{+\not{D}^2/M^2}\,\phi_n(x) \end{aligned}$$

Note that $\lambda < 0$ because $\not{D}$ is anti-Hermitean and thus $\mathrm{Re}\lambda = 0$. From this equation we can easily see that the zero modes behave very different using this regularization.

Now we make a Fourier transformation:

$$\phi_n(x) \;=\; \int \frac{\mathrm{d}^4\mathrm{k}}{(2\pi)^2}\,e^{ikx}\tilde{\phi}_n(k)$$

$$\begin{aligned} \sum_n \phi_n^\dagger(x)\gamma_5\phi_n(x) \;&=\; \lim_{M\to\infty}\int \frac{\mathrm{d}^4l\mathrm{d}^4k}{(2\pi)^4}\sum_n \tilde{\phi}_n^\dagger(l)e^{-ilx}\,\gamma_5\,e^{\frac{-\not{D}^2}{M^2}}\,e^{+ikx}\tilde{\phi}_n(k) \\ &= \lim_{M\to\infty}\int \frac{\mathrm{d}^4k}{(2\pi)^4}\mathrm{Tr}\;e^{-ikx}\,\gamma_5\,e^{-\frac{\not{D}^2}{M^2}}\,e^{ikx} \end{aligned}$$

But what is $\not{D}^2$?

$$\begin{aligned}
\not{D}^2 &= \gamma_\mu\gamma_\nu D_\mu D_\nu \\
&= \left(\frac{1}{2}\{\gamma_\mu,\,\gamma_\nu\} + \frac{1}{2}[\gamma_\mu,\,\gamma_\nu]\right) D_\mu D_\nu \\
&= \delta_{\mu\nu} D_\mu D_\nu + \frac{1}{2}[\gamma_\mu,\,\gamma_\nu]\,\frac{1}{2}\left(\{D_\mu,\,D_\nu\} + [D_\mu,\,D_\nu]\right) \\
&= D_\mu D_\mu + \frac{-i}{4}[\gamma_\mu,\,\gamma_\nu]\,F_{\mu\nu} \\
&= D_\mu D_\mu + \frac{-i}{2}\gamma_\mu\gamma_\nu F_{\mu\nu}
\end{aligned}$$

In the next step, note that

$$e^{-ikx}\, f(\partial_\mu)\, e^{ikx} = f(\partial_\mu + ik_\mu)$$

We get

$$\begin{aligned}
&\sum_n \phi_n^\dagger(x)\gamma_5\phi_n(x) = \\
&= \lim_{M\to\infty}\int \frac{\mathrm{d}^4k}{(2\pi)^4}\mathrm{Tr}\gamma_5 \exp\left\{\frac{(D_\mu + ik_\mu)\,(D_\mu + ik_\mu)}{M^2} + \frac{-i\gamma_\mu\gamma_\nu F_{\mu\nu}(x)}{2M^2}\right\} \\
&\text{change of variables: } k_\mu \to M\,k_\mu \\
&= \lim_{M\to\infty}\int \frac{M^4\,\mathrm{d}^4k}{(2\pi)^4}e^{-k_\mu k_\mu}\mathrm{Tr}\gamma_5 \exp\left\{\frac{2ik_\mu D_\mu}{M} + \frac{D_\mu D_\mu}{M^2} + \frac{-i\gamma_\mu\gamma_\nu F_{\mu\nu}(x)}{2M^2}\right\}
\end{aligned}$$

The only term that “survives” is the one quadratic in $F_{\mu\nu}$. Note that, since we use an expansion, we could have used other functions $f(+\lambda_k^2/M^2)$, provided these functions fall off rapidly enough at infinity. This shows that the following results do *not* depend on the regularization.

Using $\int \mathrm{d}^4k \exp\{-k_\mu k_\mu\} = \pi$, we get

$$\begin{aligned}
&\sum_n \phi_n^\dagger(x)\,\gamma_5\,\phi_n(x) = \\
&= \lim_{M\to\infty}\frac{-1}{2}\,\frac{M^4}{4\,M^4}\int\frac{\mathrm{d}^4k}{(2\pi)^4}\,e^{-k_\mu k_\mu}\mathrm{Tr}\,\gamma_5\gamma_\mu\gamma_\nu\gamma_\alpha\gamma_\beta F_{\mu\nu}(x)F_{\alpha\beta}(x) \\
&= -\frac{1}{32\pi^2}\varepsilon_{\mu\nu\alpha\beta}\mathrm{tr}F_{\mu\nu}(x)F_{\alpha\beta}(x)
\end{aligned}$$

where tr denotes the trace in color space.
Note that our choice of metric and γ-matrices implies that

$$\mathrm{Tr}\,\gamma_5\gamma_\mu\gamma_\nu\gamma_\alpha\gamma_\beta = 4\,\varepsilon_{\mu\nu\alpha\beta}$$

with $\varepsilon_{\mu\nu\alpha\beta}$ being the totally antisymmetric tensor and $\varepsilon_{1234} = 1$.

Thus, our Jacobian $\mathcal{J}[\beta]$ is:

$$\begin{aligned}
\mathcal{J}[\beta] &= \exp\left\{-2i\int \mathrm{d}^4x\,\beta(x)\,\sum_n \phi_n^\dagger(x)\,\gamma_5\,\phi_n(x)\right\} \\
&= \exp\left\{-2i\int \mathrm{d}^4x\,\beta(x)\,\frac{1}{32\pi^2}\varepsilon_{\mu\nu\alpha\beta}\,\mathrm{tr}F_{\mu\nu}(x)F_{\alpha\beta}(x)\right\}
\end{aligned}$$

Comparing the arguments of the exponential, we conclude that

$$\begin{aligned} \int \mathrm{d}^4x \, \frac{1}{32\pi^2} \varepsilon_{\mu\nu\alpha\beta} \operatorname{tr} F_{\mu\nu}(x) F_{\alpha\beta}(x) \; &= \\ = -\int \mathrm{d}^4x \sum_n \phi_n^\dagger(x) \, \gamma_5 \, \phi_n(x) & \\ = -\sum_n \int \mathrm{d}^4x \; \phi_n^\dagger(x) \, \gamma_5 \, \phi_n(x) & \qquad = n_- \, - \, n_+ \end{aligned}$$

with $n_\pm$ being the zero modes ϕ_0 of $\not{D}$ with $\gamma_5 \phi_0 \; = \; \pm \phi_0$.

Because the above calculations hold for every flavor, we are now ready to write down the final result:

$$\begin{aligned} \int \mathrm{d}^4x \; \mathfrak{A}\left[A_\mu\right](x) \; &= \; \int \mathrm{d}^4x \; \partial_\mu \, j_{\mu 5}(x) \\ &= \; N_f \; \int \mathrm{d}^4x \; \frac{1}{16\pi^2} \varepsilon_{\mu\nu\alpha\beta} \operatorname{tr} F_{\mu\nu}(x) F_{\alpha\beta}(x) \\ &= 2 \; N_f \; \int \mathrm{d}^4x \; \frac{1}{16\pi^2} F_{\mu\nu}(x) \; \widetilde{F}_{\mu\nu}(x) \\ &= \; 2N_f \, (n_- \, - \, n_+) \\ &= \; 2N_f \, Q \end{aligned}$$

□.

We have used the definition Eq. (2.28) here. There is a much more general theorem, also called the Atiyah-Singer index theorem. That theorem applies not only to the Dirac operator but to a whole class of elliptic operators.

2.4.2 Main results for the anomaly function

Let me briefly summarize the main results for the anomaly function: For every flavor, it holds that

$$\frac{1}{2} \mathfrak{A}[A](x) = \frac{1}{2} \partial_\mu \, j_{\mu 5}(x) = \frac{1}{16\pi^2} \operatorname{tr} F_{\mu\nu}(x) \widetilde{F}_{\mu\nu}(x) \tag{2.34}$$

Here, we see that the anomaly function $\mathfrak{A}$ is indeed a functional of the gauge field A, since the field-strength tensor F also depends on the gauge field A via Eq. (2.20). The anomaly function is defined as the divergence of the non-conserved current $j_{\mu 5}$ that can also be calculated via the triangle diagrams shown in Figure 2.1. The integral over the anomaly function,

$$\int \mathrm{d}^4 \, x \; \frac{1}{2} \mathfrak{A}[A](x) = (n_- - n_+) = Q \tag{2.35}$$

is an integer – the topological charge Q of the underlying gauge field. The topological charge Q is, via the Atiyah-Singer index theorem, equal to the difference of numbers of zero-modes with negative (n_-) and positive (n_+) chirality.

Now we can clearly see that if the underlying field configuration A has trivial topology, i.e., $Q = 0$, the current $j_{\mu 5}$ is conserved and the chiral scalar symmetry of Eq. (2.31d) would be conserved. However, due to the non-Abelian nature of the gauge fields, field configurations with non-trivial topology *do* occur and the chiral scalar symmetry is explicitly broken, leading for example to a extraordinarily high mass for the η' meson.

Chapter 3

Lattice QCD

Why use the lattice regularization for QCD? The answer is: in the case of low energies, the lattice regularization is the only practical approach to QCD. The deeper reason is, that at low energies, the strong coupling constant α_s is of order of unity. Thus, an expansion in a small parameter, as in QED or in high energy QCD, is not possible. The lattice regularization also solves the issues of infrared and ultraviolet divergences that trouble most quantum field theories. Lattice QCD simply bounds all possible momenta from below and from above. I will now describe the lattice regularization in more detail.

The key ingredient to the lattice regularization is the discretization of spacetime. The most common choice is a hypercubic lattice. The spacing between lattice points in a given direction is the same, but different directions may have different lattice spacings and a different number of lattice points. The quarks live on the lattice points and the gauge fields live on the links connection the lattice points. For a schematic picture, see Figure 3.1. For the gauge fields, periodic boundary conditions in all spacetime directions apply. For the quark fields, periodic boundary conditions in the spatial directions and anti-periodic boundary conditions in the temporal direction apply. The spacetime distance between neighboring lattice points a is called the lattice spacing.

3.1 Discretization of the Gauge Fields

Since the spacetime is now discrete, the spacetime separation between lattice points is a finite quantity. This implies that the gauge fields are no longer elements of the gauge algebra, but are now elements of the gauge group. The gauge links are denoted with $U_\mu(x)$, where μ denotes the spacetime direction and x is the lattice point where the link is attached to.

There are many possible expressions for the gauge action. The most familiar one is the *Wilson action* [12], named after Nobel laureate Kenneth Wilson. The action of lattice gauge fields in the group $SU(N)$ is expressed via products of links, so called *plaquettes*

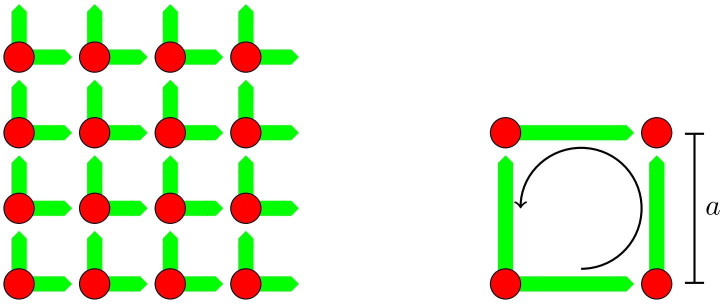

Figure 3.1: The left hand side of this figure shows a schematic picture of the lattice regularization. The red dots represent the quark field and the green links represent the gauge fields. Periodic boundary conditions in all directions apply. The right hand side figure shows a plaquette.

$U_{\mu\nu}$:

$$U_{\mu\nu}(x) = U_\mu(x)\; U_\nu(x+\hat{\mu})\; U_\mu^\dagger(x+\hat{\nu})\; U_\nu^\dagger(x) \tag{3.1}$$

$$S_{\text{gauge}} = \beta \sum_{x\in\text{lattice}} \sum_{\mu<\nu} \left(1 - \frac{1}{N}\,\mathrm{Re}\,\mathrm{tr}\,U_{\mu\nu}(x)\right) \tag{3.2}$$

The lattice coupling constant β is related to the continuum coupling via $\beta = \frac{2N}{g^2}$.

It is indeed straightforward to show that in the limit of $a \to 0$, the Wilson action yields the familiar continuum action for gauge fields. For a detailed calculation see [8]. The Wilson gauge action is not the only possible gauge action. In fact, there are many more gauge actions that are better suited for many purposes. These improved actions usually require more computer time to evaluate. Most improved actions do not use just 1×1 plaquettes, but also 1×2 plaquettes or even more complicated paths.

The gauge transformations for lattice gauge fields resemble finite transformations in the continuum. A lattice gauge transformation is a function V,

$$\begin{aligned} V: \quad \text{lattice} &\longrightarrow SU(N) \\ x &\longmapsto V(x) \end{aligned} \tag{3.3}$$

A gauge link $U_\mu(x)$ is transformed to $U'_\mu(x)$ via

$$U'_\mu(x) = V(x)\; U_\mu(x)\; V^\dagger(x+\hat{\mu}) \tag{3.4}$$

This transformation implies that closed loops for links on the lattice are gauge invariant. For example the trace of the plaquette $\mathrm{tr}\,U_{\mu\nu}(x)$ is a gauge invariant object and so is the lattice gauge action.

3.2 Discretization of the Quark Fields

The discretization of the quark fields is somewhat tricky. The first problem is, that the naïve discretization in Eq. (3.5) yields unphysical modes, the so called *doublers*. These arise from the (anti)-periodic boundary conditions.

$$\begin{aligned} S^{\text{naive}}_{\text{ferm.}} &= \\ &= a^4 \sum_{x\in\text{lattice}} \sum_\mu \bar{\psi}(x) \left[\gamma_\mu \frac{U_\mu(x)\;\psi(x+a\hat{\mu}) - U_\mu^\dagger(x-a\hat{\mu})\;\psi(x-a\hat{\mu})}{2a} + m\psi(x)\right] \\ &= a^4 \sum_{x,\,y\,\in\text{lattice}} \sum_\mu \bar{\psi}(x) \underbrace{\left[\underbrace{\gamma_\mu \frac{U_\mu(x)\;\delta_{x,y+a\hat{\mu}} - U_\mu^\dagger(x-a\hat{\mu})\;\delta_{x,y-a\hat{\mu}}}{2a}}_{D^0_{\text{naive}}} + m\delta_{x,y}\right]}_{D_{\text{naive}}} \psi(y) \end{aligned} \tag{3.5}$$

A solution to this problem is the Wilson-Dirac operator D_W. The lattice fermion action using the Wilson-Dirac D_W operator then reads:

$$S^{\text{W.-D.}}_{\text{ferm.}} = \sum_{x,\,y\,\in\text{lattice}} a^4\;\bar{\psi}(x) \Bigg[\tag{3.6}$$

$$\underbrace{\underbrace{\gamma_\mu \frac{U_\mu(x)\;\delta_{x,y+a\hat{\mu}} - U_\mu^\dagger(x-a\hat{\mu})\;\delta_{x,y-a\hat{\mu}}}{2a} - \frac{U_\mu(x)\;\delta_{x,y+a\hat{\mu}} - 2\delta_{x,y} + U^\dagger(x-a\hat{\mu})\;\delta_{x,y-a\hat{\mu}}}{2a}}_{D^0_W} + m\delta_{x,y}}_{D_W}$$

$$\Bigg]\psi(y)$$

The quark fields transform under a gauge transformation like Eq. (3.3) like

$$\psi'(x) = V(x)\,\psi(x), \qquad \bar{\psi}'(x) = \bar{\psi}(x)V^\dagger(x) \tag{3.7}$$

This behavior ensures, together with Eq. (3.4) that the Wilson-Dirac action is invariant under gauge transformations. The Wilson-Dirac operator effectively removes the doublers, but introduces another problem. The chiral symmetry is now lost. The *chiral symmetry* means, that the massless Dirac operator no longer anti-commutes with γ_5. In the continuum, $\{\not{D}, \gamma_5\} = 0$, and even the massless naïve lattice Dirac operator conserves the chiral symmetry: $\{D^0_{\text{naive}}, \gamma_5 = 0$. The massless Wilson-Dirac operator D^0_W no longer conserves chiral symmetry. This has implications for the analysis of the topology of gauge fields. If D^0_W does not conserve chiral symmetry, then the symmetry of Eq. (2.31d) is already broken in the Lagrangian. Our primary argument why topological gauge fields are interesting was, that the symmetry Eq. (2.31d) is present in the Lagrangian but broken by quantum effects. This means that if we use D^0_W for the study of topological gauge fields, our results would have to be interpreted with great care.

What one needs is a lattice Dirac operator that removes doublers and preserves chiral symmetry at the same time. That seemed like an impossible task, since the no-go theorem of Nielsen, Bech and Niyomiya [13] says that there cannot be a lattice Dirac operator that has the correct continuum limit, has no massless doublers, is ultra-local and anti-commutes with γ_5.

Luckily, there is a solution to the limit. The idea is to re-formulate the chiral symmetry on the lattice. The original requirement for chiral symmetry, $\{D, \gamma_5\} = 0$ for some lattice Dirac operator D is relaxed to the Ginsparg-Wilson equation [14]:

$$\{D,\, \gamma_5\} = a\, D\, \gamma_5\, D \tag{3.8}$$

Operators that solve the Ginsparg-Wilson equation exist and are widely used.

The most prominent solution to the Ginsparg-Wilson equation is the *Overlap Operator* [15, 16], [17, 18, 19]. The overlap operator is constructed via

$$D_{\text{overlap}} = \frac{1}{a}\Big(1 - A\,(A^\dagger A)^{-\frac{1}{2}}\Big) = \frac{1}{a}\Big(1 - \operatorname{sign}(A))\Big) \tag{3.9}$$

with $A = 1 - aD$ where D is a lattice Dirac operator without doublers, e.g. the Wilson operator, and sign being the matrix sign function. This operator shows several nice features: it is local (although not ultra-local), it has exact zero-modes without requiring finetuning, and the complex eigenvalues come in complex conjugate pairs. All eigenvalues lie on a circle in the complex plane, so so-called Ginsparg-Wilson circle. Just like in the continuum, zero-modes have a definite chirality, that is, the matrix element of a zero-mode ϕ_0 with γ_5, $\phi_0^\dagger(x)\gamma_5\phi_0 = \pm 1$. The matrix element of any complex eigenmode with γ_5 vanishes. The downside of the overlap operator is, that the matrix sign function is extremely costly in terms of computer time.

However, there are other operators offering a kind of compromise between chirality and cost. The lattice Dirac operator I will be using later, is the *Chirally Improved* (CI) Operator [20, 21, 22]. Roughly speaking, the CI Operator is an approximate solution to the Ginsparg-Wilson equation. Thus, the CI Operator is almost chiral and requires less computer time than the Overlap Operator. The complex eigenvalues also come in complex conjugate pairs and they lie approximately on the Ginsparg-Wilson circle although that requires some finetuning. Just like for the Overlap Operator, the matrix element of a complex eigenmode with γ_5 vanishes. However, the γ_5-matrix element of a real mode is usually not exactly plus or minus one, although it does not vanish. As a rule of thumb, the closer such a matrix element is to ±1, the better the quality of the eigenmode. Quality means, that the eigenmode is not caused by a dislocation in the underlying gauge configuration.

3.3 Generating Ensembles of Lattice Gauge Configurations

3.3.1 Markov chains

Now that we know what the Lagrangian on the lattice looks like, we want to measure some meaningful quantities. The general approach is to generate an ensemble of gauge field configurations via a Markov process. A Markov process generates a chain of states – gauge field configurations in our case – with the property that the next state does only depend on the present state and does not depend on any other past state. When generating gauge field configurations, additional requirements apply.

Naturally, the algorithm has to be *ergodic*, i.e., the algorithm can reach all positions in configuration space.

Furthermore, detailed Balance is required, i.e., the probability to reach a given state is the same as to leave a given state. This means that

$$P(g' \to g)\, Q(g) = P(g \to g')\, Q(g') \tag{3.10}$$

Here, $P(g \to g')$ is the transition probability, i.e., the probability to change from state g to state g' in the Markov chain, and $Q(g)$ is the weight of the state g. In our case, the weight of a state is a function of its action, namely e^{-S} with S being the action.

Next, we have to think about who our algorithm that generates the gauge field configurations can be implemented efficiently. The keyword for that is *importance sampling.* The generated gauge functions will differ in their statistical weight, i.e., the gauge configurations will have a different action. Importance sampling means, that the probability that a given configuration gets generated as part of the Markov chain is equal to the action of the gauge configuration. This technique allows an efficient evaluation of correlation functions, as I will now outline.

Generally, the expectation value $\langle \hat{O} \rangle$ of some operator $\hat{O}$ can be expressed through the Euclidean path integral. In the continuum, the relation reads

$$\langle \hat{O} \rangle = \frac{\int [DA]\; [D\psi]\; [D\bar{\psi}]\; e^{-S\left[A,\psi,\bar{\psi}\right]} O[A,\, \psi,\, \bar{\psi}]}{\int [DA]\; [D\psi]\; [D\bar{\psi}]\; e^{-S\left[A,\psi,\bar{\psi}\right]}} \tag{3.11}$$

where $D[\,\cdot\,]$ denotes the path integral measure of the gauge fields A and the fermion fields $\bar{\psi}$ and ψ. The action reads

$$S[A,\, \psi,\, \bar{\psi}] = \int \mathrm{d}^4 x \Big(\bar{\psi}(x)(\not{D} + m)\psi(x) + \frac{1}{2}\,\mathrm{tr}\,(F_{\mu\nu}(x)\, F_{\mu\nu}(x)) \Big) \tag{3.12}$$

Here, $\not{D}$ is the Dirac operator given in Eq. (2.29) and $F_{\mu\nu}(x)$ is the field strength tensor given in Eq. (2.20). The path integral over the Grassmann fields ψ and $\bar{\psi}$ in (3.11) can be calculated exactly and yields the determinant of the operator $M = \not{D} + m$. Operators $\hat{O}$ that depend on the Grassmann fields are then transformed into functions that depend on the inverse of M, the so-called propagator M^{-1}:

$$\langle \hat{O} \rangle = \frac{\int [DA]\; (\det M) e^{-S\left[A\right]} O[A,\, M^{-1}]}{\int [DA]\; (\det M) e^{-S\left[A\right]}} \tag{3.13}$$

Keep in mind that M still depends on the gauge fields A. The computation of the fermion determinant, $\det M$ requires a lot of computer resources, and so do the calculations of the propagators M^{-1}. In the further course of this thesis, I will *not* be concerned with any quantities that depend on the propagators. Therefore, I will now make a simplification that is quite common: The *quenched* approximation sets the fermion determinant $\det M \equiv 1$.

On the lattice, the path integral becomes the sum over all possible configurations and the fields A in the gauge algebra are replaced by the links U in the gauge group:

$$\langle \hat{O} \rangle = \frac{\prod_{x\in\text{lattice}} \prod_{\mu=1}^{4} \mathrm{d}\,U_\mu(x)\; e^{-S\left[U\right]} O\left[U\right]}{\prod_{x\in\text{lattice}} \prod_{\mu=1}^{4} \mathrm{d}\,U_\mu(x)\; e^{-S\left[U\right]}} \tag{3.14}$$

where $\mathrm{d}\,U_\mu(x)$ is the Haar measure for the group integration of the link variable at point x in direction μ. Keep in mind that all the dependencies on the fermion fields ψ and $\bar{\psi}$ are gone since we are using the quenched approximation.

Although Eq. (3.14) can – in principle – be evaluated exactly, it is much too complicated in the case of general gauge fields. Instead, one uses Monte Carlo integration to evaluate Eq. (3.14). This means, generate a set of gauge field configurations U via a Markov process such that the probability for a given gauge configuration to be produced is $e^{-S[U]}$ — this is the point where the meaning of the term *importance sampling* is visible. Then, the expectation value $\langle \hat{O} \rangle$ can be approximated via

$$\langle \hat{O} \rangle \approx \frac{1}{\mathcal{N}} \sum_{\text{configurations}} O\left[U\right] \tag{3.15}$$

where $\mathcal{N}$ is the number of gauge configurations.

3.3.2 The Metropolis Algorithm

The next question is: what is an algorithm that satisfies detailed balance as in Eq. (3.10) and does importance sampling? The widely used *Metropolis Algorithm* [23, 24] accomplishes both tasks. In the case of quenched lattice QCD, the Metropolis algorithm works as follows:

start Generate an arbitrary gauge configuration. This can be any gauge configuration. Common choices are a configuration with all links equal to $\mathbb{1}$ (called “cold start”) or a random gauge configuration.

update Make some change to the link variables. In many cases, it is sufficient to change only one link variable

accept/reject Compute the change of the action ΔS the update caused. If $\Delta S \leq 0$ accept the change, if $\Delta S > 0$, accept the change with a probability of $e^{-\Delta S}$. Otherwise reject the update.

sweep Go to **update** and change another link variable, until all link variables in the lattice have been visited.

A series if update-accept/reject steps that visits all links in the lattice is called a *sweep*. Typically, the gauge configurations before and after just one sweep are strongly correlated. Therefore, one performs many sweeps – depending on the action, lattice size, lattice spacing, and other parameters – before a gauge configuration is saved for further analysis. The details like the exact form of the gauge action and the way the updates were performed are covered in the next chapter.

Chapter 4

The Ensembles

In the previous chapter, I outlined the general principles of lattice gauge theory and how to generate a set of gauge configurations. In this chapter, I will explain in detail what algorithms and parameters I used. The generated ensembles serve as the basis for all further analysis.

4.1 Lattice gauge action

I chose the Lüscher-Weizs tree level improved gauge action for all the ensembles. This action offers $\mathcal{O}(a^2)$ reduction of discretization errors [25, 26]. In addition to the 1×1 plaquettes of the Wilson gauge action, the Lüscher-Weisz action also incorporates 1×2 and 2×1 plaquettes. Their relative weight is chosen such as to to minimize discretization errors. The coefficients β_0 and β_1 in the following formula relate to the inverse coupling β via

$$\beta_0 + 8\beta_1 = \beta \qquad . \tag{4.1}$$

A good choice for the coefficients β_0 and β_1 is [26]

$$\beta_0 = \frac{5}{3}\beta \quad , \qquad\qquad \beta_1 = -\frac{1}{12}\beta \quad . \tag{4.2}$$

It can be shown through analytic calculations that this particular choice reduces discretization errors [25]. The gauge action then reads

$$\begin{aligned} S_L^{\text{gauge}} = \sum_{x \in \text{lattice}} \Big\{ &\beta_0 \sum_{\mu,\,\nu}^{\mu<\nu} \left[1 - \frac{1}{N} \operatorname{Re}\operatorname{tr} U_{\mu\nu}(x)\right] \\ &+\beta_1 \sum_{\mu,\,\nu}^{\mu<\nu} \left[1 - \frac{1}{N} \operatorname{Re}\operatorname{tr} U_{\mu\nu}^{\text{long}}(x)\right] \\ &+\beta_1 \sum_{\mu,\,\nu}^{\mu<\nu} \left[1 - \frac{1}{N} \operatorname{Re}\operatorname{tr} U_{\mu\nu}^{\text{wide}}(x)\right] \Big\} \end{aligned} \tag{4.3}$$

The long and wide plaquettes are defined as follows:

$$\begin{aligned} U_{\mu\nu}^{\text{long}}(x) =& U_\mu(x) U_\mu(x + a\hat{\mu}) U_\nu(x + 2a\hat{\mu}) U_\mu^\dagger(x + a\hat{\nu} + a\hat{\mu}) U_\mu^\dagger(x + a\hat{\nu}) U_\nu^\dagger(x) \quad , \\ U_{\mu\nu}^{\text{wide}}(x) =& U_\mu(x) U_\nu(x + a\hat{\mu}) U_\nu(x + a\hat{\mu} + a\hat{\nu}) U_\mu^\dagger(x + 2a\hat{\nu}) U_\nu^\dagger(x + a\hat{\nu}) U_\nu^\dagger(x) \end{aligned} \tag{4.4}$$

During a gauge update, we change one link randomly and compute the change of the action. The change in the action after changing one link $U_\mu(x)$ into an updated link $U'_\mu(x)$ is given by:

$$\Delta S = \operatorname{Re}\operatorname{tr}\left(\left(U_\mu(x) - U'_\mu(x)\right) \cdot \left(\text{sum of staples attached to the changed link}\right)\right) \tag{4.5}$$

Figure 4.1 shows what terms appear in the calculation of the sum of staples necessary for one gauge update. The updated link $U'_\mu(x)$ is chosen according to the following algorithm. At first, a matrix U'' is computed via

$$U'' = \operatorname{norm} \begin{pmatrix} \varrho_1 \cos(\phi_1) + i\varrho_1 \sin(\phi_1) + b & \varrho_2 \cos(\phi_2) + i\varrho_2 \sin(\phi_2) \\ 0 & 0 \end{pmatrix} \tag{4.6}$$

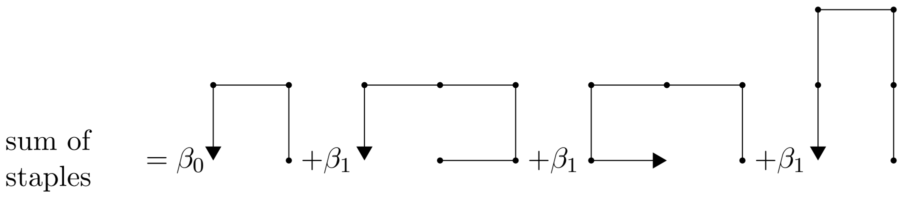

Figure 4.1: The staples contributing in one Metropolis update for the Lüscher-Weisz gauge action. There are four types of staples attached to one link in all six directions.

with

$$\phi_{1,2} \text{ is randomly chosen in the interval } [0, 2\pi) \quad ,$$
$$\varrho_{1,2} = \sqrt{-\log(1 - x_{1,2})} \text{ and } x \text{ equally distributed in the interval } [0, 1) \quad ,$$
$$\text{and the bias } b = 3.3 \quad .$$

The norm is defined via

$$\text{norm} \begin{pmatrix} a & b \\ c & d \end{pmatrix} = \begin{pmatrix} u & v \\ -\bar{v} & \bar{u} \end{pmatrix} \text{ with } u = \frac{a}{\sqrt{a\bar{a} + b\bar{b}}}, \quad v = \frac{b}{\sqrt{a\bar{a} + b\bar{b}}} \tag{4.7}$$

The particular choice for the update ensures that the updates are ergodic, since $\varrho_{1,2}$ are always positive and have a Gaussian distribution, and that $\phi_{1,2}$ are equally distributed. The bias b causes the updates to prefer matrices closer to the unit matrix, which improves acceptance rates. In a last step, with a probability of 0.5, the updated link $U'_\mu(x) = U''$ and with a probability of 0.5, $U'_\mu(x) = U''^\dagger$.

4.2 Setting the scale

One we have generated an ensemble of lattice gauge configurations, we are interested in their physical properties. An obviously important property is, whether the generated ensemble represents gauge fields that are above or below the confinement phase transition. The transition is actually a cross-over [27, 28] for realistic quark masses and a first order phase transition for zero quark mass. An order parameter for the confinement phase transition is the static quark potential.

4.2.1 The static quark potential

The static quark potential is the potential between two infinitely heavy quarks. Not only can it be used as an order parameter, but is also a convenient method for setting the scale a. The scale a describes the distance between neighboring lattice points in physical units. On the lattice, we can assume that the potential has the following form, where we ignore $\mathcal{O}a$ corrections:

$$V(R) = C + B/R + S \cdot R \tag{4.8}$$

In Eq. (4.8), $a\ V(R)$ is the potential in lattice units, C is just a constant term, B is the coefficient to the Coulomb term, S is the string tension squared, and R is the distance in lattice units.

In the continuum, the potential assumes the form

$$V(r) = C' + B'/r + \sigma^2 r \tag{4.9}$$

It follows easily from Eq. (4.8) and Eq. (4.9) that $\sqrt{\sigma} a = \sqrt{S}$, since $(1/a)V(R) = V(r)$.

Setting $\sigma = 440\ MeV$, we can derive the lattice spacing a via

$$a = \sqrt{S}\ \frac{197 MeV\ fm}{440\ MeV} \tag{4.10}$$

As usual, we employ natural units setting $\hbar \equiv 1$, and $c \equiv 1$.

$$\begin{aligned} 1 fm = Am, &\qquad 1MeV = B\ J \\ \hbar = H\ Js &\qquad 1J = \frac{\hbar}{Hs} \\ c = X\ m/s &\qquad 1m = c\ s/X \\ fm \times MeV &= \frac{A \times B}{X \times H} \end{aligned}$$

$$fm \times MeV = \frac{10^{-15} \times 1.602176462 \cdot 10^{-13}}{299792458 \times 1.054571628 \times 10^{-34}} = \frac{1}{197.326966}$$

$$\Rightarrow\ 197.326966\ fm\ MeV = 1$$

The extraction of the signal for the static quark potential from thermalized lattice gauge configurations is rather straightforward, but requires a few refinements. The master formula for the static quark potential is

$$V(R) = \ln \frac{\Big\langle W(R,T) \Big\rangle}{\Big\langle W(R,T+1) \Big\rangle} \tag{4.11}$$

since

$$\Big\langle W(R,T) \Big\rangle = e^{-T\ V(R)} \tag{4.12}$$

The naïve method to evaluate the Wilson loops and then calculate the potential according to Eq. (4.11) is likely to fail because the signal-to-noise ratio is quite bad. Two methods can be used to improve the signal for the static quark potential.

The first method is a fattening of the temporal links. Every gauge link in the time direction is replaced by the average of the attached staples. This procedure modifies the static quark potential up to a distance of one lattice spacing. Therefore, I only employ one step of fattening. Similar techniques are discussed in great length in [29]. This step has to be applied before other steps improving the signal-to-noise ratio.

The second method is spatial APE smearing. The overlap of $W(R,T)$ with the flux tube can significantly be improved with spatial smearing. This method replaces any given gauge link in the spatial directions by a weighted average of the link itself and the spatial staples [30, 31]. This method is iterated several times. Since the temporal gauge links are left unaltered and the temporal staples are not taken into account, the static quark potential is left unchanged under spatial smearing. For all measurements of the static quark potential given in this thesis, I used 20 steps of spatial smearing.

4.3 The phase transition

The temperature of the phase transition can be determined in several ways. Two commonly used order parameters for the QCD phase transition are the value of the temporal string tension and the distribution of the Polyakov loop. The string tension can be extracted from the static quark potential. However, for small temporal lattice extents, the computation via Wilson loops does not yield good results. Computing the static quark potential via Polyakov loop correlators is much more appropriate in those cases. The value of the Polyakov loop itself can easily be computed directly from the gauge configurations.

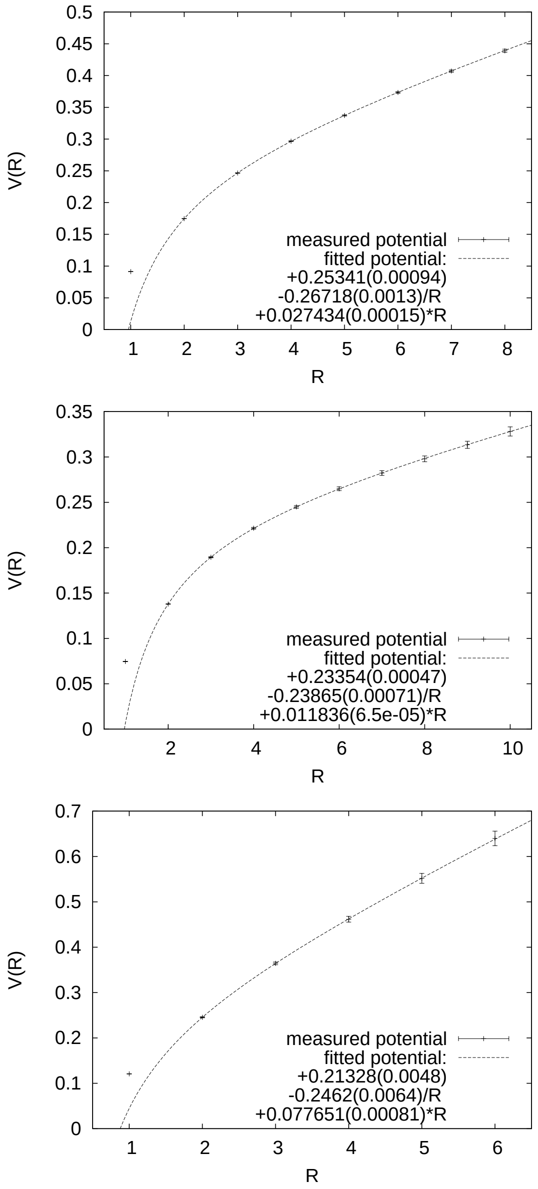

Figure 4.2: The first plot shows the fit of $c+b/x+sx$ to the static quark potential obtained from 366 configurations with $\beta = 1.95$ and a lattice size of 16^4. The dashed line shows the fitted potential, fitted in the range of 2 to 8 lattice spacings. The second plot shows the same fit obtained from 35 configurations with $\beta = 2.1$ and a 20^4 lattice in the range from 2 to 10 lattice spacings. The third plot is obtained from 100 configurations with $\beta = 1.8$ and a 12^4 lattice, fitted in the range from 2 to 6 lattice spacings.

β	$\sigma\, a^2$	$a\ /\ fm$	lattice size	box length / fm	# of configurations
1.8	0.07765(81)	0.1247(13)	12^4	12 $a = 1.50$	100
1.95	0.02743(15)	0.07415(40)	16^4	16 $a = 1.186$	366
2.1	0.011836(7)	0.04870(3)	20^4	20 $a = 0.974$	35

Table 4.1: This table shows lattice spacing for those ensembles predominantly used in this work. With a lattice spacing around 0.1 fm, the configurations are reasonably fine.

4.3.1 The string tension

The static quark potential can be computed conveniently via Eq. (4.13), where $\langle\ \cdot\ \rangle$ denotes the ensemble average as usual, and $L(\vec{x})$ denotes the Polyakov loop at a spatial lattice coordinates $\vec{x}$.

$$V(R) = -\frac{1}{N_T} \sum_{\vec{x}} \sum_{\vec{y}} \left(\left\langle L(\vec{x}) L^\dagger(\vec{y}) \right\rangle \delta(R - |\vec{x} - \vec{y}|) \right) \tag{4.13}$$

The Polyakov loop itself is defined for the $SU(2)$ gauge group, via Eq. (4.14).

$$L(\vec{x}) = \frac{1}{2} \operatorname{tr} \prod_{t=0}^{N_T - 1} U(\vec{x}, t) \tag{4.14}$$

where U denotes an $SU(2)$ gauge link.

Figure 4.3 shows the static quark potential for the finite temperature ensembles used in this work. That figure is not meant to be qualitative in the sense that we do not aim to extract precise values for the string tension $\sqrt{\sigma}$ from the potentials. It merely illustrates which ensembles are above, at or below the QCD phase transition.

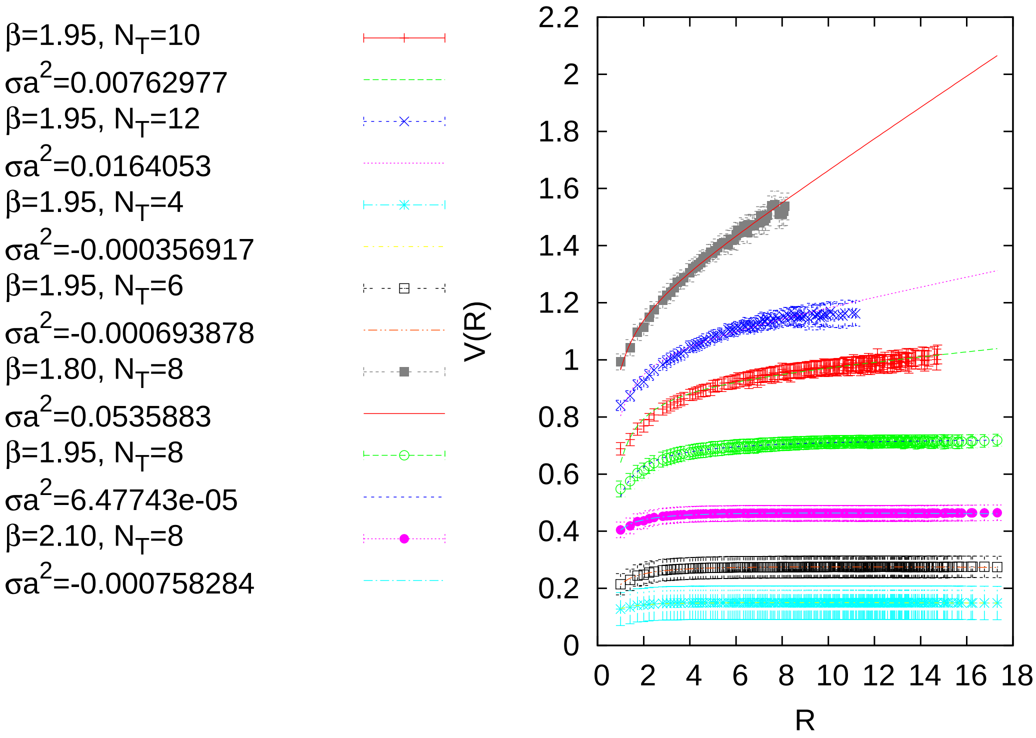

Figure 4.3: This figure shows the static quark potential obtained using Polyakov loop correlators. The Polyakov loop has been evaluated after fattening the temporal links once, followed by 20 steps of spatial APE smearing. The curves are shifted in the vertical direction by an arbitrary amount to improve the readability of the plot.
The Ordinate shows the static quark potential in lattice units, the abscissa shows the spatial distance in units of a. All plots have been obtained using an ensemble of 100 configurations.

4.3.2 The distribution of the Polyakov loop

The average value of the Polyakov loop per configuration is simply computed via Eq. (4.15).

$$L = \frac{1}{V_3} \sum_{\vec{x}} L(\vec{x}) \tag{4.15}$$

Here, V_3 denotes the 3-dimensional lattice volume, and $L(\vec{x})$ is defined in Eq. (4.14).

Figure 4.4 shows the distribution of the Polyakov loop within the various ensembles. If the distribution shows a clear gap around zero, then the ensemble lies above the QCD phase transition. Table 4.2 shows a summary of the ensembles at finite temperature.

$N_T =$	4	6	8	10	12
$\beta = 1.80$			below		
$\beta = 1.95$	above	above	at	below	below
$\beta = 2.10$			above		

Table 4.2: This table summarizes the seven ensembles at finite temperature. It states if the ensemble is above, at, or below the QCD phase transition.

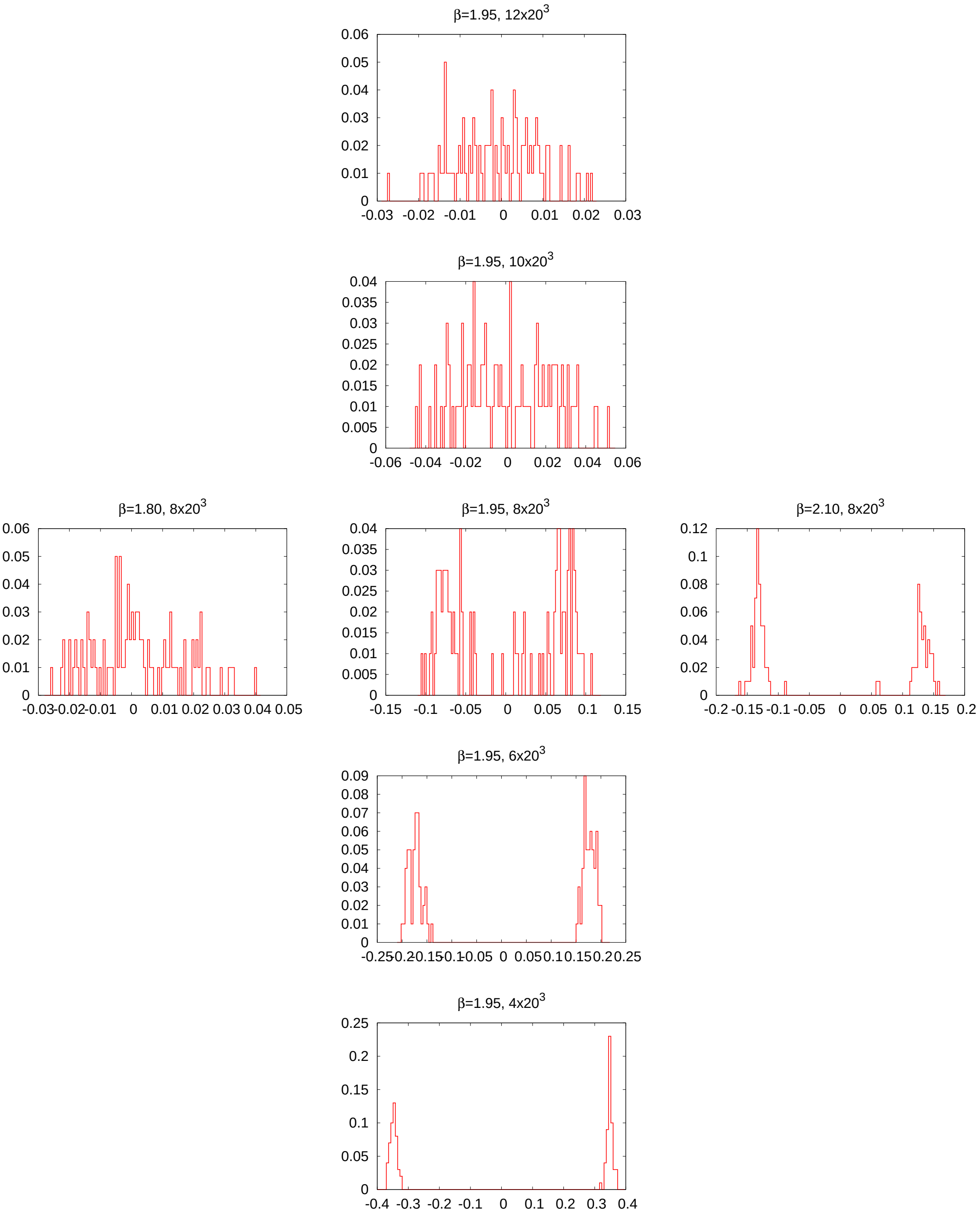

Figure 4.4: The above plots show the distribution of the Polyakov loop for the ensembles at finite temperature. Note that the plots show normalized histograms of the Polyakov loop distribution. For better readability, the plots are *not* to scale. Every ensemble consists of 100 configurations.

Chapter 5

Results at zero temperature and the power-law

In this chapter, I will present my principal results. The techniques used to obtain the results and the relevant observables are presented first. The majority of the results were calculated on the gauge ensembles described in the chapter 4, “The Ensembles.” If other ensembles were used, I will state that explicitly. A method to study the topological objects within gauge field configurations is the cluster analysis of the filtered topological charge density, the primary subject of this thesis.

5.1 The topological charge density

At first, I want to introduce the primary observable. Quite obviously, the topological charge density is the most prominent observable. It is particularly interesting that several independent definitions of the topological charge density of the lattice exist. However, there is a inherent problem that I cannot stress enough:

There is no unique *definition of the topological charge on the lattice.*

This is very different from the situation in the continuum. According to Eq. (2.35), there are three equivalent definitions of the topological charge – via the divergence of a non-conserved current, via the contraction of the field strength tensor and the dual field strength tenor and via the index of the Dirac operator.

The ambiguous situation on the lattice simply arises from the fact that the lattice is not continuous, and topology is all about continuous deformations. Luckily, not all hope is lost.

If we treat our gauge field configurations carefully enough, we can still get a reasonably sensible definition of the topological charge density. Recall, from Eq. (2.34) and Eq. (2.35), we define the *topological charge density* $q(x)$ in the continuum as:

$$q(x) = \frac{1}{16\pi^2} \operatorname{tr} F_{\mu\nu}(x) \widetilde{F}_{\mu\nu}(x) \quad . \tag{5.1}$$

We can transfer this definition directly to the lattice once we have a sensible definition of the field strength tensor. One such definition is the *highly improved* (HI) field strength tensor [32]. It works similar to the Lüscher-Weizs gauge action, in the sense that it is defined via plaquettes of different sizes, weighted to reduce lattice artifacts. The definition I chose is depicted in Figure 5.1. For every combination of μ and ν, four 1×1, 2×2 and 3×3 plaquettes are combined. The “starting point” for the plaquettes of $F_{\mu\nu}(x)$ is always x, so that $F_{\mu\nu}$ is a gauge invariant object. Keep in mind that the gauge transformations on the lattice take the form of Eq. (3.4).

Just by constructing a good field strength tensor, one obtains one definition of the topological charge on the lattice:

$$q(x) = \frac{1}{16\pi^2} \operatorname{tr} F^{HI}_{\mu\nu}(x) \widetilde{F}^{HI}_{\mu\nu}(x) \quad . \tag{5.2}$$

This definition of the topological charge only involves the gauge links. Therefore, I will call Eq. (5.2) the gluonic topological charge. Experience shows that a sensible topological charge density can only be calculated on configurations that are sufficiently smooth. The criterion is, that the topological charge density summed over all lattice points should be close to an integer, since this is the definition of the topological charge.

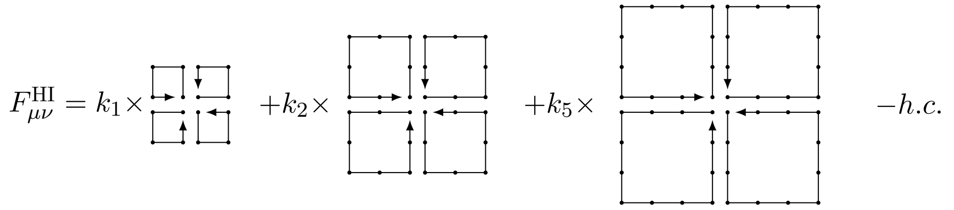

Figure 5.1: The highly improved field strength tensor has contributions from 1 × 1, 2 × 2, and 3 × 3 plaquettes. They are arranged in a gauge-covariant order. The coefficients k_1, k_2, and k_5 are chosen such that $\mathcal{O}(a^2)$ artifacts are minimized.

As we saw in Eq. (2.35), the topological charge can also be calculated via the index of the Dirac operator. The question is, can the topological charge density also be calculated in terms of the eigenmodes of some Dirac operator? The answer is [33, 9].

$$\begin{aligned} q(x) &= -\operatorname{tr}\gamma_5 \left(1-\frac{1}{2}aD_{G.W.}(x,x)\right) \\ &= -\sum_{\lambda}\left(1-\frac{a\lambda}{2}\right)\psi^\dagger_\lambda(x)\gamma_5\psi_\lambda(x) \end{aligned} \tag{5.3}$$

In the formula above, $D_{G.W.}$ is a Dirac operator that satisfies the Ginsparg-Wilson equation Eq. (3.8), λ runs through all eigenvalues that operator and ψ_λ is the eigenmode belonging to eigenvalue λ. One such operator would be the Overlap operator shown in Eq. (3.9). For the Chirally Improved operator, I make a small modification, since the matrix element with γ_5 of its real modes is not exactly ±1:

$$\begin{aligned} q^{\mathrm{ferm.}}_N(x) = &\sum_{\substack{i=1\\ \lambda_i\ \mathrm{complex}}}^{N} \left(\left(\frac{\lambda_i}{2}-1\right)\phi^\dagger_{\lambda_i}(x)\ \gamma_5\ \phi_{\lambda_i}(x) + \left(\frac{\overline{\lambda_i}}{2}-1\right)\phi^\dagger_{\overline{\lambda}_i}(x)\ \gamma_5\ \phi_{\overline{\lambda}_i}(x)\right) \\ &+ \sum_{\mathrm{all\ real}\ \lambda_j}\left(-\frac{1}{|\rho_{5,\lambda_j}|}\phi^\dagger_{\lambda_j}(x)\ \gamma_5\ \phi_{\lambda_j}(x)\right)\ \text{ with } \rho_{5,\lambda_j} = \sum_x\left(\phi^\dagger_{\lambda_j}(x)\gamma_5\phi_{\lambda_j}(x)\right) \end{aligned} \tag{5.4}$$

In the following, I will call the definition of Eq. (5.4) the fermionic definition of the topological charge density. If N runs through all eigenmodes, we get the full topological charge density. If N only incorporates a certain number of low-lying eigenmodes, then $q^{\mathrm{ferm.}}_N(x)$ is the *filtered* topological charge. This will be become a crucial point later on. I want to point out that for the gross fermionic topological charge, $Q^{\mathrm{ferm.}} = \sum_{x\in\mathrm{lattice}} q^{\mathrm{ferm.}(x)}$, only the zero-modes contribute. This holds for both, Eq. (5.4) and Eq. (5.3). This is because the matrix element of a complex eigenmode with γ_5 is always exactly zero, both for the Overlap operator and the Chirally Improved operator:

$$\sum_{x\in\mathrm{lattice}} \phi^\dagger_{\lambda_j}(x)\ \gamma_5\ \phi_{\lambda_j}(x) \equiv 0 \quad \text{for} \quad \operatorname{Im}\lambda_j \neq 0 \tag{5.5}$$

Both, the gluonic and the fermionic definition of the topological charge density are frequently used. In principle, there is a third definition of the topological charge density given in [34]. Although that definition is conceptually very interesting since it is closely related to fiber bundles and connections in differential geometry, it is also quite challenging to be implemented on a computer. I will not go into further details about it.

5.2 Filtering

Figure 5.2 is the icon of filtering. It shows that thermalized gauge field configurations are dominated by short range fluctuations. In order to reveal the interesting long range

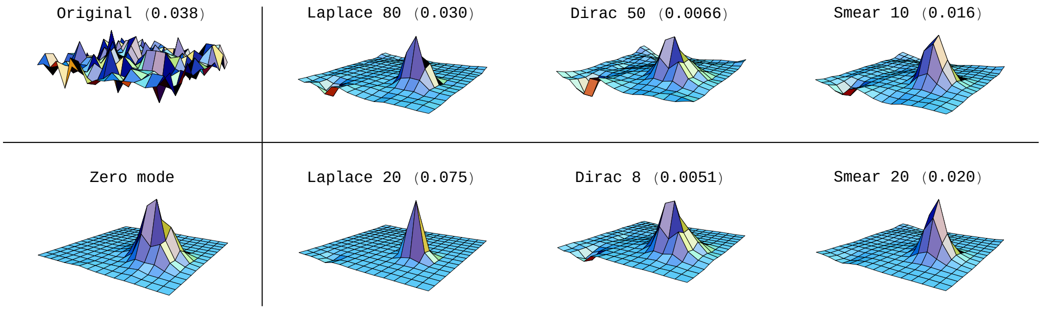

Figure 5.2: The plots visualize the filters. All images show the same 2-dimensional slice of the topological charge density of the same configuration. The upper left plot shows the unfiltered density. The lower left plot shows the scalar density of the single real eigenmode for comparison. The other plots show the filtered topological charge with the three methods and various filtering parameters. Note that the plots are drawn not in the same scale. Peak values are indicated in brackets.

objects, one has to apply some kind of filtering. Figure 5.2 shows several filtering methods in comparison: Smearing, Laplace filtering and Dirac filtering. I will explain these in more detail later. However, I want to emphasize that even with the bare eye, we see that these filtering methods pick out more or less the same structures from the seemingly orderless thermalized gauge field.

Let me briefly state the basic ideas of filtering, what we are filtering and why we think it is interesting: We are interested in the long range – or infrared – properties of gauge fields. These are possibly tied to confinement and chiral symmetry breaking. Those infrared objects carry topology. A prominent example is the instanton, although it is by far not the only example. However, these objects are hidden by short range – or ultraviolet – fluctuations. By changing the amount of filtering, we can reveal a certain amount of the interesting structures, but filtering might introduce artifacts. Now the different definitions of the topological charge density become actually an advantage: we can use different filtering methods, or even combinations of them to reduce artifacts.

I will now explain the three different filtering methods in detail.

5.2.1 Smearing

Smearing is a technique that directly averages the gauge links in a controlled way. We used APE smearing [30], which averages locally in a gauge covariant way. The new gauge link is replaced by a weighted average between the link and the attached staples. This sum usually has to be normalized, because for an arbitrary choice of the weight, the sum of link and staples is not a member of the gauge group. However, in the case of the $SU(2)$ gauge group, we choose the coefficients $\alpha = 0.55$ and $\gamma = 0.075$, following [35]. For the gauge group $SU(2)$, the smeared link then is in the gauge group. Figure 5.3 shows this process.

While keeping the coefficients α and γ fixed, we can still control the strength of the “smearing filter” easily. Smearing is not applied only once, but many times. The number of smearing steps is then a measure for the filter strength. We say that a higher number of smearing steps is a stronger filter. More and more fluctuations are smoothed out and the infrared objects emerge.

We can now use the APE smearing to define a smearing-filtered topological charge density: It is simply the topological charge density computed via Eq. (5.2) on smeared gauge field configurations:

$$q^{\text{smeared}}(x) = \frac{1}{16\pi^2} \operatorname{tr}\left[F^{HI}_{\mu\nu}(x)\widetilde{F}^{HI}_{\mu\nu}(x)\right] \tag{5.6}$$

where $F^{HI}_{\mu\nu}$ is computed on the smeared gauge links.

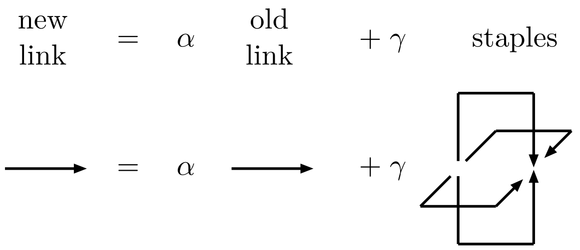

Figure 5.3: This figure visualizes the process of APE smearing. Every link is substituted by a weighted average of itself and the attached stables.

5.2.2 Laplace filtering

Laplace filtering uses the eigenmodes of the lattice Laplacian. Its definition reads:

$$\Delta^{ab}_{xy} = \sum_{\mu=1}^{4}\left[U^{ab}_{\mu}(x)\delta_{x+\hat{\mu},y} + U^{\dagger ab}_{\mu}(y)\delta_{x-\hat{\mu},y} - 2\delta^{ab}\delta_{xy}\right] \tag{5.7}$$

Here, the $U^{ab}_{\mu}(x)$ are the original, unfiltered gauge links with the color indices written out. The eigenmodes of the lattice Laplacian can be used as a filter for the gauge links in the following way [36]:

$$U^{ab\ \text{Laplace filtered}}_{\mu}(x) = -\sum_{n=1}^{N}\lambda_n\phi^{a}_{n}(x)\phi^{*b}_{n}(x+\hat{\mu})\big|_{\text{normalization}} \tag{5.8}$$

If $N = 2V$, the formula above is exact and no filtering has been done. However, if the truncate the sum, and $N << 2V$ we have an efficient filtering mechanism. The low modes of the lattice Laplacian act as a low-pass filter for infrared structures. Like smearing, Laplace filtering acts on the gauge links. The filtered topological charge density is simply:

$$q^{\text{laplace}}(x) = \frac{1}{16\pi^2} \operatorname{tr}\left[F^{HI}_{\mu\nu}(x)\widetilde{F}^{HI}_{\mu\nu}(x)\right] \tag{5.9}$$

where $F^{HI}_{\mu\nu}$ is computed on the Laplace filtered gauge links. The strength of the Laplace filter is controlled by the number of Laplacian eigenmodes used to reconstruct the gauge links. Taking fewer modes into account means a stronger filter, since high modes typically show more fluctuations.

5.2.3 Dirac filtering

The third filtering technique is known as Dirac filtering. The eigenmodes of a chiral Dirac operator are used to compute the topological charge density. It not necessary for the operator to be exactly chiral. A reasonably chiral operator is sufficient. We chose the Chirally Improved operator, as already stated earlier. Its eigenmodes have good chirality, and it is much cheaper in terms of computer time than the Overlap operator. We use the Eq. (5.10) top compute the topological charge density from the eigenmodes of the Chirally Improved operator. The sum is truncated, such that only the low eigenmodes contribute to the topological charge density. Again, we can control the strength of the filter. Using *less* modes means stronger filtering, since typically the low modes show very little fluctuations.

$$q_N^{\text{dirac.}}(x) = \sum_{\substack{i=1 \\ \lambda_i \text{ complex}}}^{N} \left(\left(\frac{\lambda_i}{2} - 1\right) \phi^\dagger_{\lambda_i}(x)\, \gamma_5\, \phi_{\lambda_i}(x) + \left(\frac{\overline{\lambda_i}}{2} - 1\right) \phi^\dagger_{\overline{\lambda_i}}(x)\, \gamma_5\, \phi_{\overline{\lambda_i}}(x) \right)$$
$$+ \sum_{\text{all real } \lambda_j} \left(-\frac{1}{|\rho_{5,\lambda_j}|} \phi^\dagger_{\lambda_j}(x)\, \gamma_5\, \phi_{\lambda_j}(x) \right) \text{ with } \rho_{5,\lambda_j} = \sum_x \left(\phi^\dagger_{\lambda_j}(x) \gamma_5 \phi_{\lambda_j}(x) \right) \tag{5.10}$$

5.3 Optimal filtering

Now we have three different filtering methods available. Every method has a parameter to control its filtering strength – the number of smearing steps in the case of APE smearing and the number of eigenmodes in the case of Laplace filtering and Dirac filtering. At this point, I want to emphasize again that those three filtering methods differ fundamentally. Yet, as we already saw in Figure 5.2, they pick out largely the same structures. Of course, a judgment by eye is not a scientific approach. The task is now to tune the filtering methods such that the structures they pick out match best. In other words, we are looking for a relatively simple parameter that reflects the common structures found by the individual methods. The "matching" of two methods A and B, respective the matching of topological densities q_A and q_B is measured with the ratio of cross-correlators to auto-correlators at zero distance:

$$\Xi_{q_A q_B} \equiv \frac{\langle \chi_{q_A q_B}(0) \rangle \, \langle \chi_{q_A q_B}(0) \rangle}{\langle \chi_{q_A q_A}(0) \rangle \, \langle \chi_{q_B q_B}(0) \rangle} \quad \text{with} \quad \chi_{q_A\, q_B}(0) \equiv (1/V) \sum_x \, q_A(x)\, q_B(x) \tag{5.11}$$

The angle brackets $\langle \ \cdot \ \rangle$ denote the ensemble average, as usual. The quantity Ξ will be exactly 1 if the topological densities q_A and q_B are identical. Any deviation of Ξ from 1 is a sign of a mismatch. Figure 5.4 shows plots of Ξ of all three methods at various filtering strengths. It turns out that there is a "ridge" of optimal match for any two methods. See the caption of the figure how the matching was performed. In the following analysis, we frequently use two sets of filtering parameters, *weak* and *strong* filtering. The filtering parameters are listed in Table 5.1. Their values are drawn from 10 configurations with $\beta = 1.95$ and a lattice size of 16^4, part of the ensemble listed in Table 4.1.

	smearing steps	Laplace eigenmodes	Dirac eigenmodes
weak filtering	10	80	50
strong filtering	20	20	8

Table 5.1: This table shows the filtering parameters used for weak and strong filtering. Their values are determined by optimal filtering.

To confirm that the matching of filter parameters is truly reliable, we made a number of cross-checks. A first consistency check is, whether the topological charge is stable under successive steps of smearing or under inclusion of more Laplace modes. Note that the topological charge is stable under Dirac filtering by definition, since only the zero-modes contribute to the gross topological charge, see Eq. (5.5). We can see that the topological charge computed on smeared configuration quickly approaches 1. For the Laplace filtered configurations, the topological charge is not as stable, but this is understandable: these configurations are not completely smooth and get more and more "spiky" as more Laplacian modes are used. However, the Dirac zero mode is preserved under Laplace filtering, if

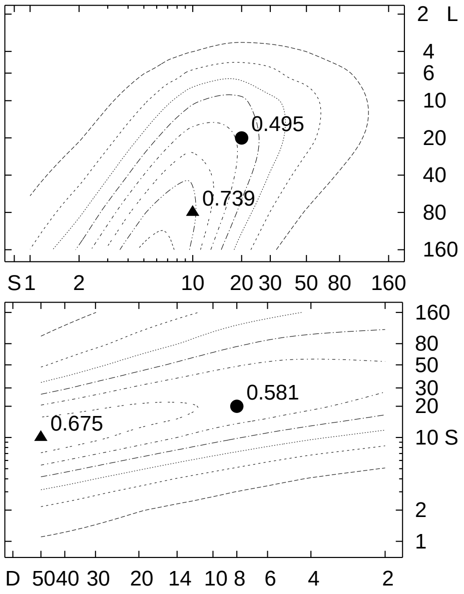

Figure 5.4: These plots show a pairwise comparison of filtering methods. Shown are lines of constant Ξ, as defined in Eq. (5.11). L, D and S refer to Laplace and Dirac filtering and smearing. The ridges in each contour plot represent the optimal matching between two methods. The triangle ▲ denotes an example of weak filtering, the dot ● represents a case of strong filtering in all three methods. The dots in the right plots relate 20 Laplacian modes to 8 pairs of non-zero Dirac modes, and these to 20 smearing steps. The dot in the left plot is close to the ridge there, confirming the consistency of matching between all three methods. Say we choose an arbitrary number of Laplace modes used for filtering, e.g., 20 modes. Then the ridge in the upper right plot gives the corresponding number of Dirac modes, here 8, marked with the dot ●. In the same fashion, we determine from the lower right plot that 8 Dirac modes correspond to 20 smearing steps. As a cross check, the position "20 Laplace modes, 20 smearing steps" in the left plot is very close to the ridge. This confirms that the method to match filtering parameters is consistent between all three methods.

at least 10 modes are used. It is also no surprise that there is a minimum of Laplace modes necessary to reproduce the Dirac zero-mode. It can be shown analytically that Laplace filtering with only two modes produces a gauge field that is pure gauge, i.e., it produces a gauge field that is just a gauge transformation of the trivial gauge field configuration [36].

smearing		Laplace filtering	
steps	Q	Q	modes
1	0.948*	1.161*	160
2	1.256*	0.947*	80
5	1.118*	0.896*	40
10	1.004*	0.778*	20
20	1.000*	0.760*	10
80	1.000*	-0.138	4

Table 5.2: This table shows the topological charge$Q$ for a configuration that has one Dirac zero-mode when not filtered. Filters marked with an asterisk * also have a Dirac zero-mode with the same chirality as the unfiltered configuration.

One might argue that the good agreement of the topological charge for smearing and

	$\lvert Q^{\text{glue}} - Q^{\text{ferm.}} \rvert \leq 0.5$	S/S_{orig}
10 smearing steps	89%	0.026
80 Laplacian modes	76%	0.036
20 smearing steps	85%	0.009
20 Laplacian modes	69%	0.017

Table 5.3: This table shows the correlation between the gluonic topological charge computed on filtered configurations and the fermionic topological chargecomputed on the unfiltered configurations. The first column shows the filtering method and the filtering parameters used. The second column shows, on how many configurations the two definitions of the topological charge agreed. Here, "agreed" means that the absolute value of the difference was less than 0.5. The third column lists the action of the filtered configuration in relation to the original configurations. The table is based on 295 gauge configurations with $\beta = 1.95$ and a lattice size of 16^4.

Dirac filtering is just accidental. Indeed, there are configurations where smearing and Laplace filtering do not yield configurations with the same topological charge as the original configuration. However, for the majority of configurations, the gluonic definition of the topological charge after smearing or Laplace filtering agrees with the fermionic definition of the topological charge. Table 5.3 makes a quantitative statement how well the two definitions agree. We can see that the agreement is quite good, although filtering has reduced the action enormously.

Another consistency check is to compare the links directly. Again, we just compare Laplace filtering and smearing, since Dirac filtering does not yield filtered links. The difference of the links after smearing $U^S_\mu(x)$ and after Laplace filtering $U^L_\mu(x)$ is computed via

$$\sum_{x,\mu} \operatorname{tr} \left(U^S_\mu(x) - U^L_\mu(x) \right)^\dagger \left(U^S_\mu(x) - U^L_\mu(x) \right) \quad . \tag{5.12}$$

The comparison of smearing and Laplace filtering via the link difference confirms the results of optimal filtering. Figure 5.5 shows plots both for periodic and anti-periodic boundary conditions of the lattice Laplace operator. In both plots, we can see that the position of weak filtering (80 Laplace modes, 10 smearing steps) and strong filtering (20 Laplace modes, 20 smearing steps) lie in a "valley" where the difference of links is smallest.

5.4 Clusters and the watermark

A cluster analysis can be done for many observables that are sufficiently smooth. In this work, clusters of the topological charge density will be in the focus. I call the method to choose some kind of cutoff in the topological charge density the *watermark* method.

5.4.1 Basic concepts

I will first give the definition of a cluster using the "watermark" method. Choosing the a watermark means that I pick a fixed fraction of points f from every configuration in the ensemble. I pick those points x where the absolute value of the topological charge $|q(x)|$ is largest. These are the points above the watermark. They are then grouped into clusters. Two points belong to the same cluster if they are nearest neighbors, i.e., if the lattice distance is smaller than a fixed value, typically 1. Figure 5.6 shows an artist's concept of the watermark. The "water" is lowered until a fixed fraction of points f is above the watermark.

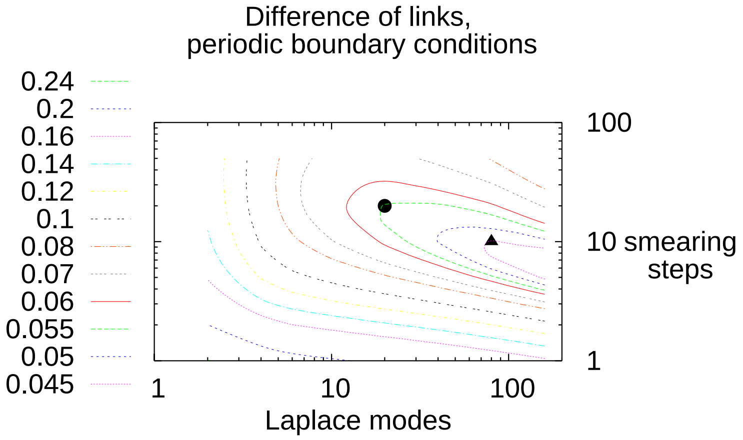

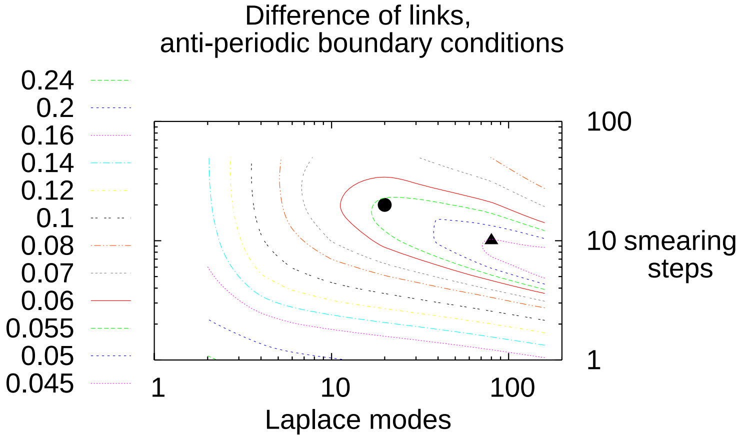

Figure 5.5: This figure shows the difference of links. The contours show the difference of links computed via Eq. (5.12). The label "●" shows the position of weak filtering, the label "▲" shows the position of strong filtering. The strong and weak filtering positions appear in the "valley" of least link differences. The link difference has been evaluated on one configuration.

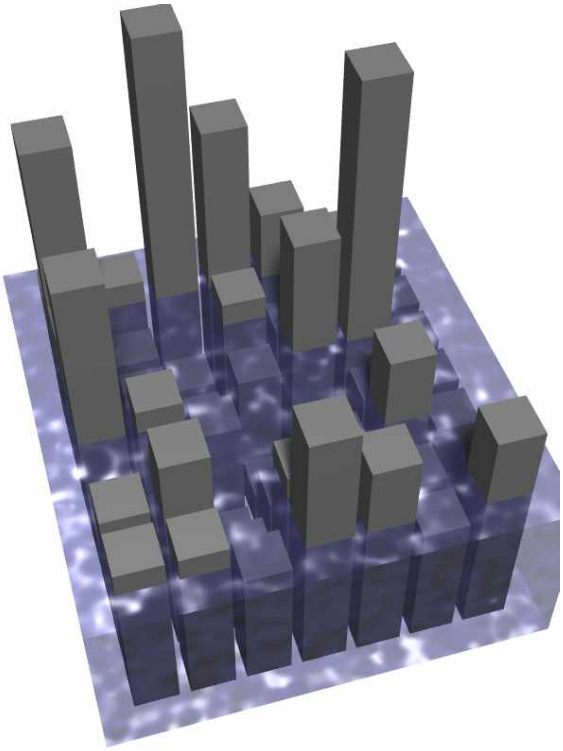

Figure 5.6: This figure shows an artist's concept of the watermark. The gray bars represent lattice points and the height corresponds to the topological charge.

This method is more convenient than choosing a fixed cutoff, because the maximal topological charge density varies greatly among configurations. Had I chosen a fixed cutoff, I would have gotten – in the same ensemble – a lot of configurations with no clusters at all and at the same time many configurations with dozens of clusters. Quite understandably this has a negative effect on the signal to noise ratio. Figure 5.7 shows the relation between the watermark and the cutoff in the topological charge density. We can see that the watermark method corresponds to large steps in the cutoff if only a small fraction of points is taken into account. Later, the cutoff decreases only very slowly with the watermark. From the curve of the Dirac filtered configuration, we deduce that the same watermark translates into very different cutoffs, as we can see by the large error bars. Note that the Dirac filtered topological charge density has been calculated from just 10 configurations, but the Laplace filtered and the smeared topological charge density has been calculated from 295 configurations.

Before we finally turn to the analysis of the clusters, I want to present one more quantity to show the agreement of the various filtering methods. In the previous section, Section 5.3, "Optimal filtering," we have convinced ourselves that the strong and weak filtering parameters are indeed optimal filtering parameters. One last consistency check now follows. Like clustering, it is also based on the concept of a watermark. For this check, I will introduce the relative point overlap. The idea is now to compare the topological charge densities directly. The topological charge density is computed via two different filtering methods A and B. The relative point overlap s_{AB} between two methods A and B at a fixed fraction of points is given by:

$$s_{AB} = \frac{\sum_{\substack{x \in X_A \cap X_B \\ q_A(x) q_B(x) > 0}} 1}{\sum_{x \in X_A \cup X_B} 1} \quad . \tag{5.13}$$

Here, $X_{A,B}$ are all points that are above the watermark for method A, B. This just means

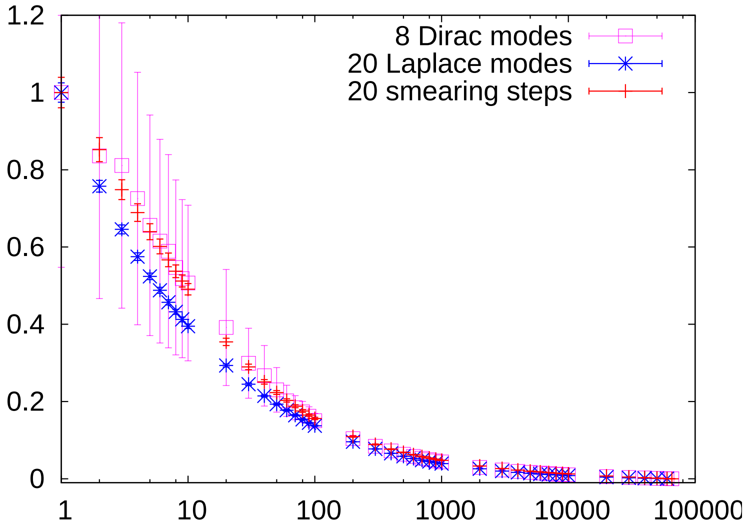

Figure 5.7: This figure shows how the watermark translates – on average – to a cutoff in the topological charge density. The abscissa shows the number of points that contribute to the cluster analysis. The ordinate shows the charge density that corresponds to that, normalized to the average maximum. For smeared and Laplace filtered configurations, the curves are an average over the full ensemble of 295 configurations, for the Dirac filtered topological charge density, the curve shows the average of 10 configurations.

that s_{AB} is the number of points that are above the watermark for both methods in common and where the sign of the topological charge density agrees, divided by the number of points above the watermark for any method. Figure 5.8 shows plots for the relative point overlap at weak and strong filtering, as well as a pictogram how it is calculated. We can see that the agreement of all three methods is quite good for all values of the fraction of points f.

5.4.2 Power-law and combined filtering

Before I come to the highlight of this thesis, I want to restate the main train of thoughts that led us here.

QCD is theory for the strong nuclear interaction.

Topology of gauge fields is possible in QCD, since QCD is a non Abelian gauge theory. Topological field configurations are connected to chiral symmetry breaking and might be connected to confinement.

Lattice QCD is a regularization of QCD that makes QCD accessible for simulations on computers.

Topology in lattice QCD is a tricky field, since there is no *unique* definition of topology on the lattice.

Filtering is a way to extract the interesting infrared objects from the noisy, raw gauge field configurations.

Optimal filtering matches the filtering parameters of Dirac filtering, Laplace filtering and smearing consistently.

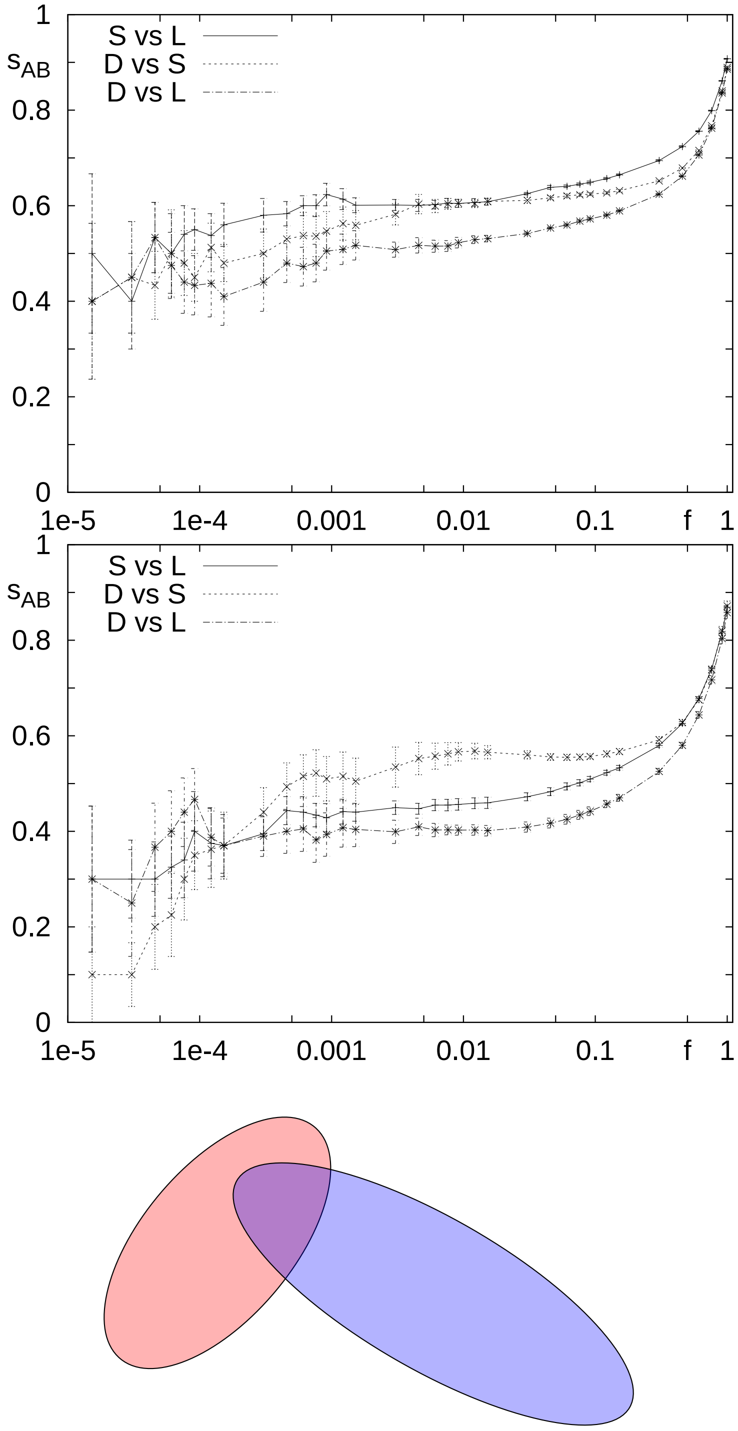

Figure 5.8: This figures show the relative point overlap. The top plot shows is for weak filtering and the bottom plot for strong filtering. Both measurements were produced with 10 configurations. The error bars show the 1 σ error. The pictogram in the bottom visualizes the way the relative point overlap is computed. If, the red area is above the watermark for method A, and the blue are is above the watermark for method B, then the relative point overlap s_{AB} is the purple area (the overlap) divided by the total colored area.

Clustering via a watermark identifies clusters of topological charge density for a certain fraction of points (number of points per volume) in a filtered gauge configuration.

The interesting measurements now are, how the number of clusters depends on the watermark. The main result is show in Figure 5.9: The number of clusters as a function of the fraction of points (or number of points) obeys a power law. Furthermore, we can combine the different filtering methods to reduce artifacts.

Let us discuss the findings in Figure 5.9 in more detail. For low values of $f = N_p/V$, where N_p is the number of points in clusters and V is the lattice volume, we see that the number of clusters obeys a power-law. Also, we see that combined filtering enlarges that part of the curve where the power-law is visible. At some number of points, the power-law breaks down, at eventually the number of clusters decreases. The decrease of clusters beyond a certain watermark is simply the point when the clusters take up a substantial part of the total volume and start merging. Furthermore, I want to stress that all three methods see a power-law, but combined filtering enhances measurement. We can draw two conclusions from that result:

Combined filtering should be used whenever we need quantitative results. Only filtering methods should be combined if their respective filtering parameters

Smearing is a valid technique. Sometimes, smearing has been criticized because important physics might washed away my the averaging process. Yet, we see that smearing – if done in a well controlled way – does yield results comparable to other filtering methods. We conclude that results obtained from smearing are just as valid as results obtained with Dirac filtering or Laplace filtering. The last statement applies if not too much smearing was applied, i.e., if the smearing parameters were tuned to be equivalent to another smearing method known to give sensible results.

5.4.3 Exponent of the power-law and the instanton gas

Now that we found a power-law, the next question is: What is its exponent? Furthermore, does this exponent depend on the filtering? In order to answer these questions, I will show results for the exponent ξ of the power-law and its dependence of smearing and Laplace filtering. Figure 5.10 shows a contour plot of the exponent. The exponent has been determined via matched filtering with Laplacian eigenmodes and smearing. We have not used Dirac modes in this analysis, because Dirac eigenmodes are by far more expensive to calculate. We see that the exponent ξ forms a “valley” where it is almost constant, it is marked with a shade in the plot. It is consistent with previous findings that the optimal filtering parameters lie in the same valley. This is yet another hint that optimal filtering is a method that yields consistent, physically sensible results.

We might ask ourselves now, can we determine the value of ξ to a certain degree, and if so, does it have any other implications? Figure 5.11 shows the values for ξ at optimal filtering. They have been computed on the same set of configurations as those used for Figure 5.10. The exponent starts out high if filtering is weak, i.e., if many Laplacian modes and few smearing steps are used. When filtering becomes stronger, ξ decreases. The curve tends towards a plateau for strong filtering. However, filtering beyond a certain point does not make much sense. On the one hand, the statistic breaks down because there are only very few – less than 10 – clusters per configuration. A sensible fit of a power-law is no longer possible. On the other hand, filtering with less than 6 Laplacian eigenmodes is unsound, because the gross topological charge might no longer be conserved, as shown in Table 5.2. Figure 5.11 shows the value that is expected if the clusters were only caused by a dilute instanton gas. The value of ξ at the plateau found via optimal filtering is very different from the value for the dilute instanton gas. I can make with quiet conscience the statement that the measurements presented in this section exclude

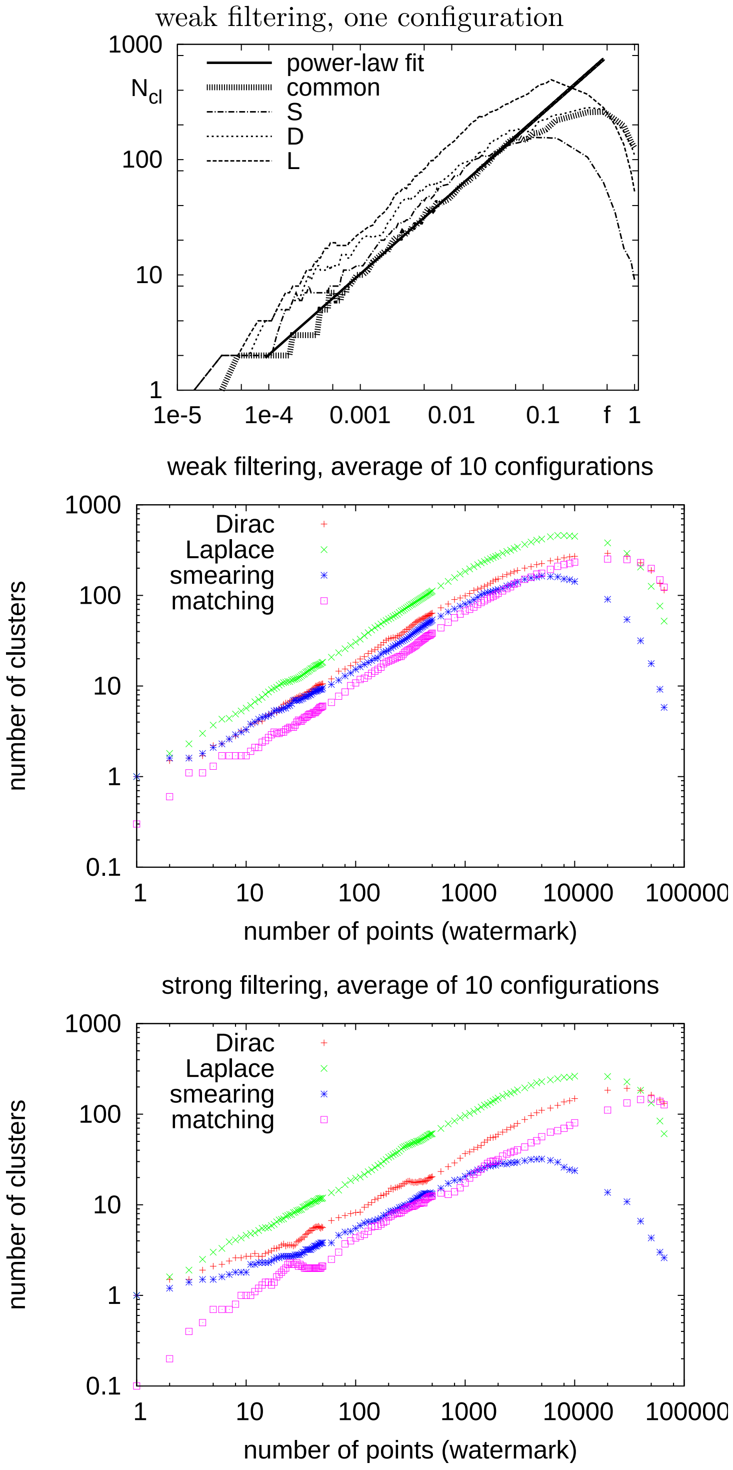

Figure 5.9: This figure shows the main result: The number of clusters obeys a power-law as a function of the fraction of points f at low watermarks. All plots show four curves: The clusters found via Dirac filtering, via Laplace filtering, via smearing and via the matching of all three methods. Matching means, that only those points are taken into account for the cluster analysis that are above the watermark for all three methods. The top plot is for a single configuration at weak filtering, the middle plot and the bottom plot are the average of ten configurations.

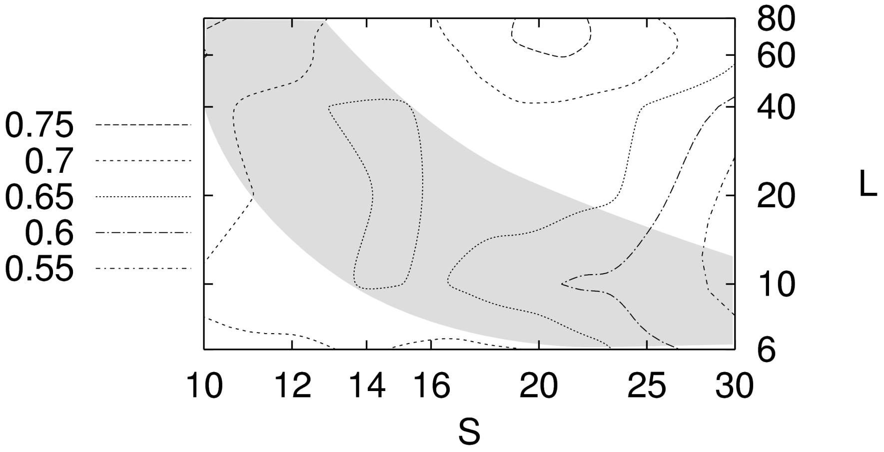

Figure 5.10: This figure shows a contour plot of ξ, the exponent of the power-law. The data shown in this plot is taken from 9 configurations with $\beta = 1.95$ and a lattice size of 16^4. For every combination of smearing steps S and Laplacian eigenmodes L, we have performed combined filtering, i.e., only those clusters were used to determine the power-law that are seen by both filtering methods at the same time. The shaded area marks a "valley" where ξ is almost constant. It coincides with the parameters for optimal filtering.

the dilute instanton gas. While this does not come as a surprise, it is nevertheless a step towards the understanding of topological objects and a point in the book of filtering. From the plot in Figure 5.11, we can read off an exponent of $\xi = 0.595(5)$. In principle, this result should be checked for finite volume and finite size effects.

5.5 A model for the power-law

Now is the right time to think about a model for the power-law. Questions that come up immediately are: Can we make any predictions and can we distinguish a power-law from noise?

5.5.1 The exponent for noise

The latter question is relatively easy to answer. Assume the topological densities for every point in the lattice were chose absolutely randomly. Furthermore, assume the lattice is large. Then, if we lower the watermark by one point, i.e., we consider one more point in the cluster analysis, this new point will be a new cluster by itself. Why is that? If the lattice is large, and we use only a small fraction of points for the cluster analysis, it is very unlikely that two neighboring points have a similar value for the topological charge. If the lattice was infinitely large, the probability for two neighboring points to be of similar height would be actually zero. Therefore, we can expect that at a low fraction of points, we get a new cluster for every point added to the cluster analysis. This translates into a power-law with exponent $\xi = 1$.

5.5.2 A realistic model

In order to construct a model for the distribution, we try to be as general as possible. Starting from few, sensible assumptions, we can develop a simple model that can explain the power-law. The first assumption is, that all objects have the same shape function f, but

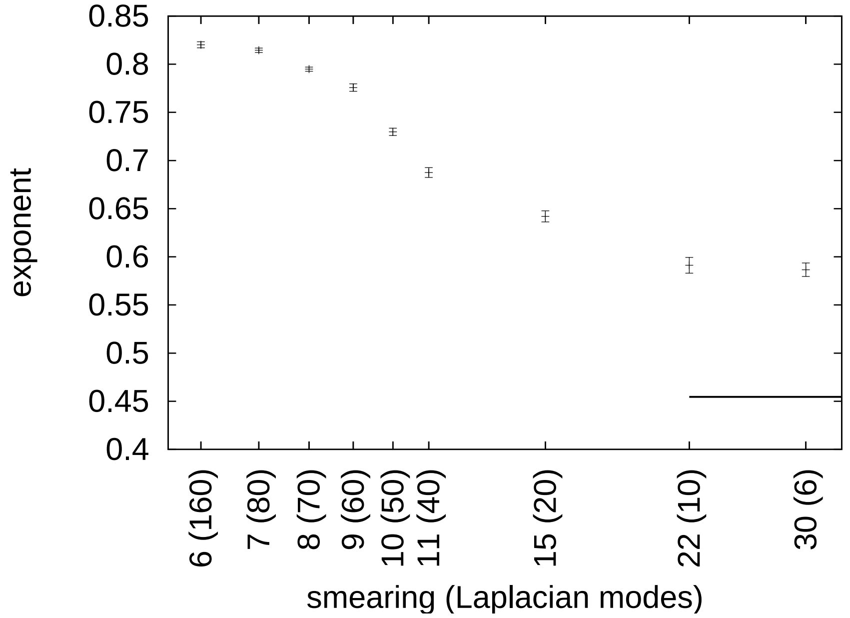

Figure 5.11: This plot shows the value of ξ for optimal filtering. We can see that for very weak filtering, ξ starts out high and then decreases, until it reaches a plateau. If filtering becomes too strong, the statistic beaks down because there are only very few clusters per configuration. Therefore, considering values beyond 30 smearing steps or with less than 6 Laplace modes is not sensible. The horizontal bar marks the value of ξ that is predicted by a dilute instanton gas.

the width ρ of the objects can vary. Furthermore, all objects have the same dimensionality δ. With these assumptions, we can write the topological density of a single object as:

$$q(r) = C' f(r/\rho)\, \rho^{-\delta} \quad . \tag{5.14}$$

The last assumption will be that all objects have the same topological charge Q. We define the maximum of the topological charge density q_0 via

$$q_0 \equiv q(0) = f_0 C' \rho^{-\delta} \text{ with } f_0 \equiv f(0). \tag{5.15}$$

We now calculate the volume that lies above a certain threshold $\tilde{q}$

$$V(\tilde{q}, q_0) = \int_0^\infty \mathrm{d}\, r\, r^{d-1}\, \theta\big(q(r) - \tilde{q}\big) = \rho^d \widetilde{R}^d \tag{5.16}$$

with $f(\widetilde{R}) = \tilde{q}\rho^\delta / C'$. Now, assume the topological objects have a power-law distribution in their shape parameter ρ, that can also be expressed via a distribution of maxima q_0:

$$\mathcal{D}(\rho)\, \mathrm{d}\, \rho = C'' \rho^\beta\, \mathrm{d}\, \rho \qquad \mathcal{D}(q_0)\, \mathrm{d}\, q_0 = C''' q_0^{-\alpha}\, \mathrm{d}\, q_0 \tag{5.17}$$

The two distributions need to be equal. Therefore,

$$\rho^\beta\, \mathrm{d}\, \rho \propto q_0^{-\alpha}\, \mathrm{d}\, q_0 \quad . \tag{5.18}$$

Using Eq. (5.15) we get $\beta = \delta\alpha - \delta - 1$. In the next step, we calculate the number of clusters above the cut-off $\tilde{q}$.

$$N_{clust}(\tilde{q}) = \int_0^\infty \mathrm{d}\, q_0\; \mathcal{D}(q_0)\; \theta(q_0 - \tilde{q}) \propto \tilde{q}^{1-\alpha} \tag{5.19}$$

Now, we need the number of points above the cut-off:

$$\begin{aligned} N_{points}(\tilde{q}) &= \int_0^\infty dq_0 \mathcal{D}(q_0)\theta(q_0 - \tilde{q})V(\tilde{q}, q_0) \\ &\propto \tilde{q}^{1-\alpha-d/\delta}. \end{aligned} \tag{5.20}$$

In the last step, we derive the prediction for the exponent ξ, defined as:

$$\xi \equiv \frac{\mathrm{d}\log N_{clust}(\tilde{q})}{\mathrm{d}\log N_{points}(\tilde{q})} = \frac{1-\alpha}{1-\alpha-d/\delta} = \frac{\beta+1}{\beta+1+d} \tag{5.21}$$

For the instanton gas model, the various parameters are $\delta = 4$, $d = 4$, $\alpha = 11/6$, $\beta = 7/3$, $\xi = 5/11$. according to [37, 38].

The final message of this section is, that *if* the topological objects all have the same shape – governed by some shape parameter ρ, and *if* the size distribution of the topological objects is determined by a power-law distribution of ρ, *then* the measurable cluster distribution ξ also obeys a power law.

I would like to stress that this result is independent of the dimensionality δ of the topological objects. The power law behavior only depends on the dimension d of spacetime and on the exponent β of the size distribution of ρ. This result cannot, a priori, distinguish between vortices, monopoles, calorons or other topological objects. Yet, it has the power to exclude models that predict other values of ξ.

Further results and finite temperature

This chapter contains various results that compare the power law and cluster analysis under various conditions that differ from the previous. In particular we want to know if the power-law changes if the change the definition of a cluster and what happens if lattice parameters are changed. Interesting results are those obtained for lattices at finite temperature.

6.1 Different cluster definitions

Varying the definition of what a cluster is constitutes another cross-check if the newly found power-law is robust and free from subtle systematic errors. One can of course change the cluster definition and define two points as belonging to the same cluster if the lattice distance is smaller than say, $\sqrt{2}$, $\sqrt{3}$, or 2. One can expect that the total number of clusters will decrease, since clusters will merge earlier if points with a lattice distance larger than 1 belong to the same cluster. Yet, a change of the exponent of the power-law is not expected. What I find indeed meets the expectations. Just the total number of clusters found for a given fraction of points f changes. The overall exponent of the power-law is not changed. Figure 6.1 shows these results.

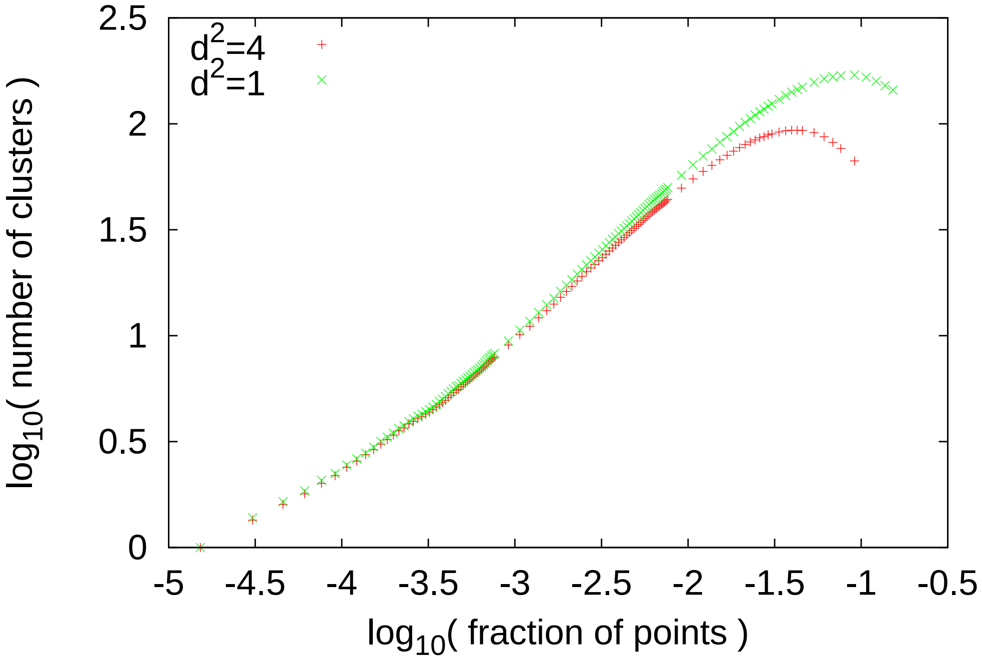

Figure 6.1: This figure shows that varying the definition of what is the "neighbor" of a point does not change the results. The curve labeled $d^2 = 1$ uses the usual nearest-neighbor definition, whereas the curve labeled $d^2 = 4$ assumes all points belong to the same cluster if the squared lattice distance is equal or smaller than 4. The usual nearest-neighbor definition yields more clusters, but the slope of the two curves is very similar. The data shown in this plot was obtained from an ensemble of 295 configurations with $\beta = 1.95$ and a lattice size of 16^4.

6.2 Finite temperature

The investigation of topological structures would not be complete without checking the behavior of the clusters found at *finite* temperature. The connection of topological structures with chiral symmetry breaking is well established. The interesting question now is, if clusters change their behavior at the phase transition. This might provide deeper insight into the mechanisms of the QCD phase transition.

6.2.1 Behavior of individual clusters

First, we study how individual clusters react with respect to a change in temperature. More precisely, we want to know how the Polyakov loop inside the cluster behaves. This can be visualized using a quantity we call "Polyakov loop difference" of a cluster. It is defined as follows:

For every point $x = (t, \vec{x})$ inside a given cluster, the Polyakov loop along is computed via

$$P(\vec{x}) = \frac{1}{2} \operatorname{tr} \prod_{t=0}^{N_t - 1} U(t, \vec{x}) \quad . \tag{6.1}$$

Then P_{max} is the maximum of $P(\vec{x})$ inside the cluster and P_{min} is the minimum. The difference,

$$P_{\text{diff}} = P_{\text{max}} - P_{\text{min}} \tag{6.2}$$

then is the Polyakov loop difference of a given cluster. The average Polyakov loop is simply

$$P_{\text{av}} = \frac{1}{N} \sum_{(t,\vec{x}) \in \text{cluster}} P(\vec{x}) \tag{6.3}$$

Figure 6.2 shows the results.

6.2.2 The power-law at finite temperature

An interesting question is also if the power law changes if the temperature rises above the phase transition.

Figure 6.3 shows two plots how the power-law behaves as the temperature is changed. Quite unexpectedly, when the temporal extent N_T of the lattice is changed in from 4 to 12, the power-law does not change. An extent of $N_T = 4$ is above the phase transition, $N_T = 8$ is approximately at the phase transition and $N_T = 12$ is well below the phase transition. If the temperature is changed by varying the coupling constant β, the picture is slightly different. While the curves for $\beta = 1.95$ (at the phase transition) and $\beta = 2.10$ (above the phase transition) have the same slope, the curve for $\beta = 1.80$ (below the phase transition) has a lower slope in general but a steeper onset. However, this effect can very well be due to the roughness of the configurations at $\beta = 1.80$. For the bottom plot in Figure 6.3, 20 smearing steps have been used for all values of β, but since configurations with low β are far more noisy, more smearing steps might have been appropriate. The exponent of the power law, when filtered appropriately, does not seem to be dependent on the temperature, yet the total number of objects changes.

6.2.3 Cluster moments

Up to now, I have been talking about the cluster distribution. Nothing was said about the individual shape or the dimensionality of the clusters. I will make an attempt to shine some light on the shape of clusters in this section. My first goal is to find a quantity that

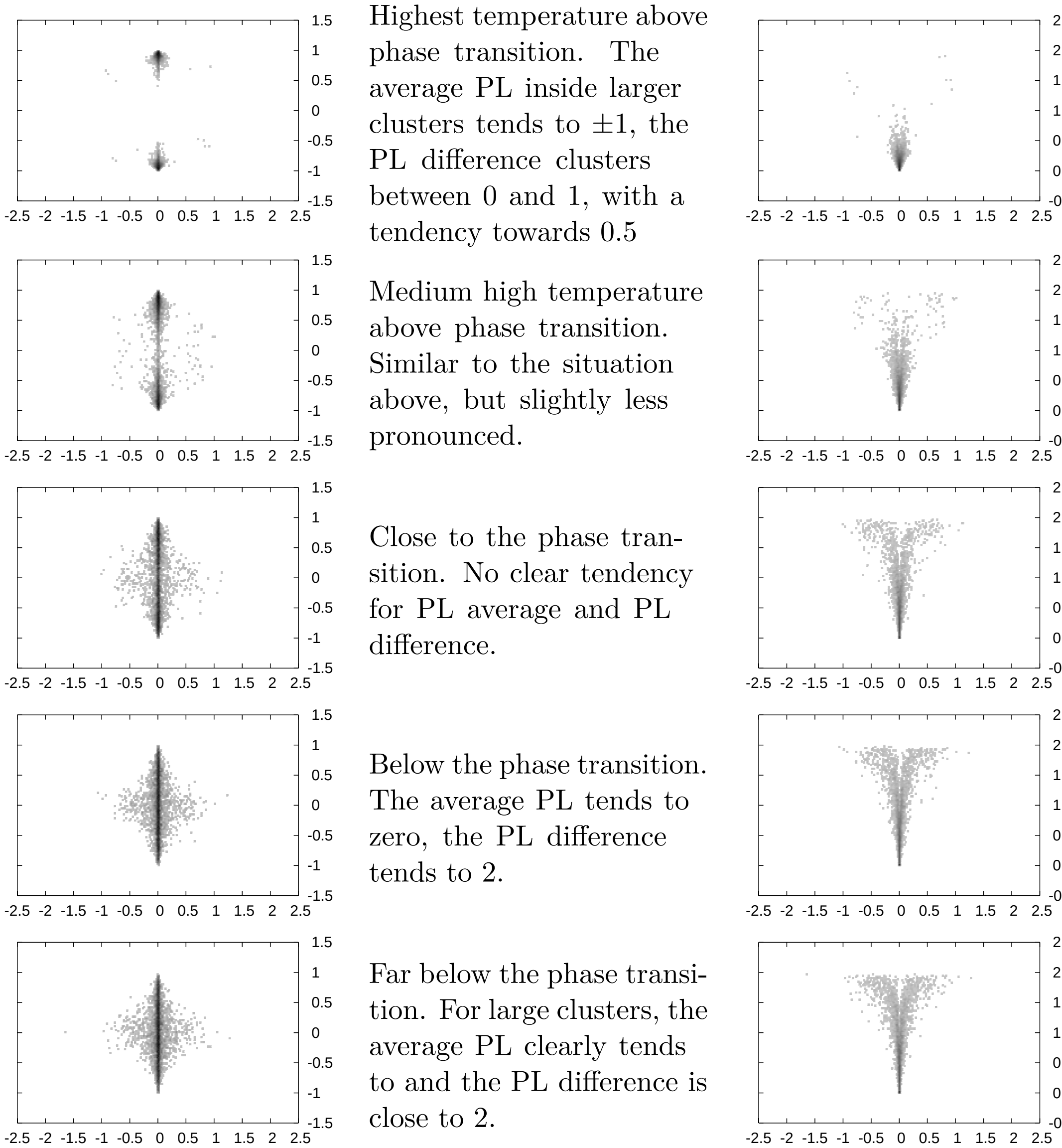

Highest temperature above phase transition. The average PL inside larger clusters tends to ±1, the PL difference clusters between 0 and 1, with a tendency towards 0.5

Medium high temperature above phase transition. Similar to the situation above, but slightly less pronounced.

Close to the phase transition. No clear tendency for PL average and PL difference.

Below the phase transition. The average PL tends to zero, the PL difference tends to 2.

Far below the phase transition. For large clusters, the average PL clearly tends to and the PL difference is close to 2.

Figure 6.2: The left column shows scatter plots of the averaged Polyakov loop (PL), the right columns shows the PL difference, according to Eq. (6.2). Polyakov loop or PL difference are plotted on the ordinate, the topological charge of a given cluster is plotted on the abscissa. The individual clusters feel the temperature. All measurements for this figure are taken from the full ensemble of 295 configurations after 20 smearing steps. The watermark for all measurements was 1000 points. The spatial lattice size is always 16^3, and the temporal lattice sizes were – from top row to bottom row – 12, 10, 8, 6, and 4. Large clusters show a monopole like behavior above the phase transition and a caloron like behavior below the phase transition.

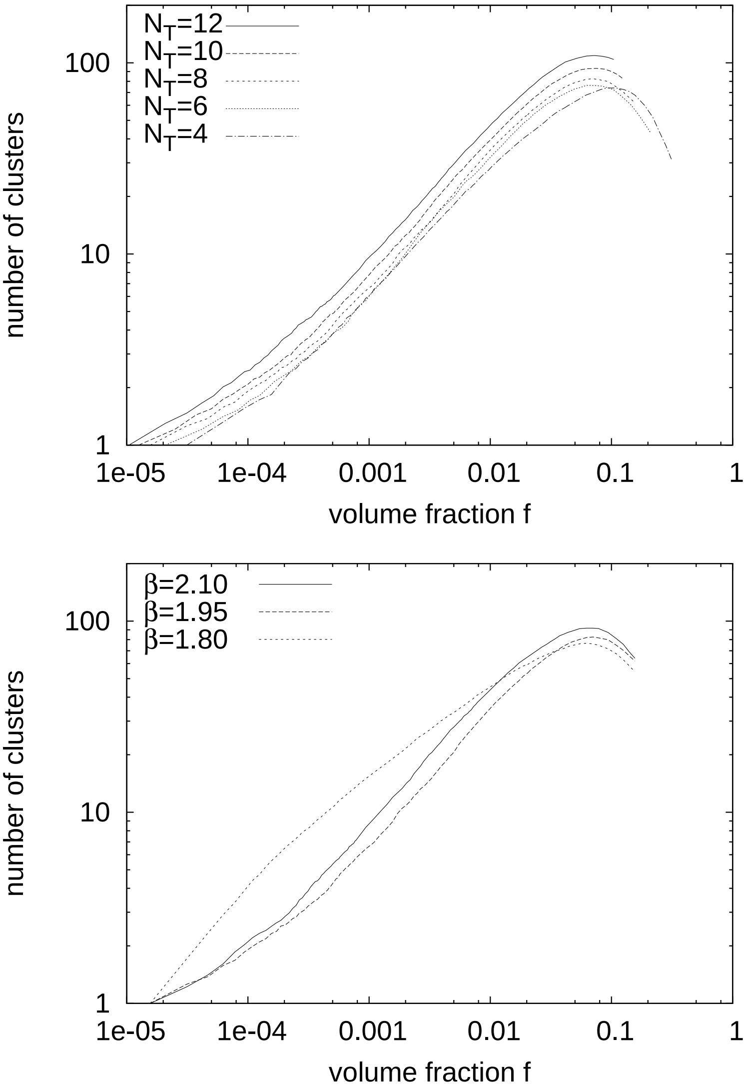

Figure 6.3: The figures shows the power laws for finite temperature. All data was taken from the full ensemble of 295 configurations, after 20 smearing steps. In the top plot, the temperature is varied by changing the temporal extent of the lattice from $N_T = 4$ (above the phase transition), to $N_T = 8$ (approximately at the phase transition) and to $N_T = 12$ (below the phase transition). In the bottom plot, the temperature is varied by changing the coupling constant β from $\beta = 2.1$ (above the phase transition), to $\beta = 1.95$ (at the phase transition) and to $\beta = 1.80$ (below the phase transition) while keeping the lattice dimensions constant at $20^3 \times 8$.

describes the overall shape of clusters. Plotting pictures of clusters is just not suitable for the analysis of a full ensemble of configurations. I chose the eigenvalues of the inertial tensor as a suitable quantity. Figure 6.4 illustrates how the eigenvalues can describe the shape of an object. If the cluster is spherical, all eigenvalues will be equally large. For an prolate cluster, one eigenvalue is smaller than the other ones. An oblate cluster will have one eigenvalue larger than the other ones. In the three-dimensional case, the inertial tensor is a familiar object in classical mechanics. Its definition can be easily extended to four dimensions. In Eq. (6.4) shows the definition we used. It is the definition of the inertial tensor M_{ij} on the lattice, where every point in the cluster is considered as a small four-dimensional hypercube of volume a^4.

$$\begin{aligned} M_{ii} &= \frac{1}{3}\sum_{j=1}^{4}(1-\delta_{ij})\Big((r_j+1/2)^3-(r_j-1/2)^3\Big) \\ M_{ij} &= -\frac{1}{4}\Big((r_i+1/2)^2-(r_i-1/2)^2\Big)\Big((r_j+1/2)^2-(r_j-1/2)^2\Big) \quad \text{for} \quad i\neq j \end{aligned} \tag{6.4}$$

Here, M_{ij} are the elements of the inertial tensor, and r_i is the distance of a lattice point from the cluster's center of mass.

I want to note that the finite volume and the periodic boundary conditions are not an issue in our case. There is a potential problem with clusters that wind around the lattice in one or more directions. In the case of a periodic cluster, there is no unique definition of its center. Therefore, one cannot define the inertial tensor for a periodic cluster. However, I checked that in the case analyzed here – a watermark of 1000 points – only very few periodic clusters occur.

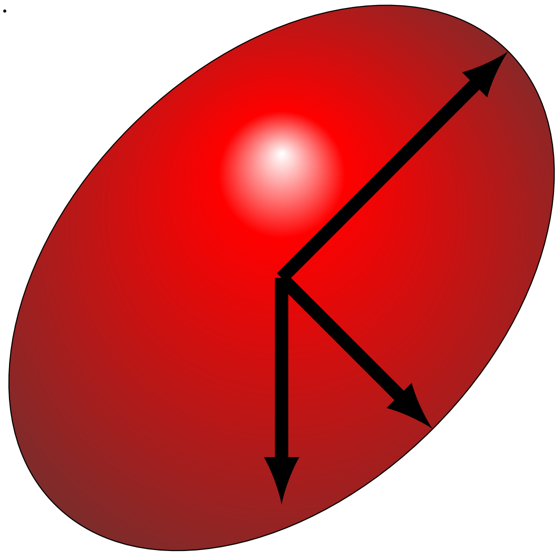

Figure 6.4: This illustration shows a schematic picture how the inertial tensor can describe the shape of a cluster. The cluster – the red object – is elongated in one direction. This implies that one eigenvalue of the inertial tensor is larger than the other ones.

The results of the analysis of cluster moments are shown in Figure 6.5. Two ensembles, one below the critical temperature and one above, have been analyzed. The plots show a two-dimensional histogram of the distribution of cluster moments. "Distribution" here means that the cluster moments in relation to the cluster size is plotted. The distinction is important, because for very small clusters, only few possibilities exist. A cluster consisting of just one point, for example, is always spherical, whereas a cluster consisting of only two points is always prolate. What we can see from the plots in Figure 6.5 is, that the clusters tend to be oblate in one direction. This is because the clusters show a tendency that one eigenvalue is smaller than the other ones, and the larger eigenvalues are of comparable size. This would be the behavior of a “stick.” However, distribution of cluster moments is spread out over a large range. There is no such thing as the typical cluster shape. It is very well possible that the prolate shapes just come from the merger of two spherical clusters.

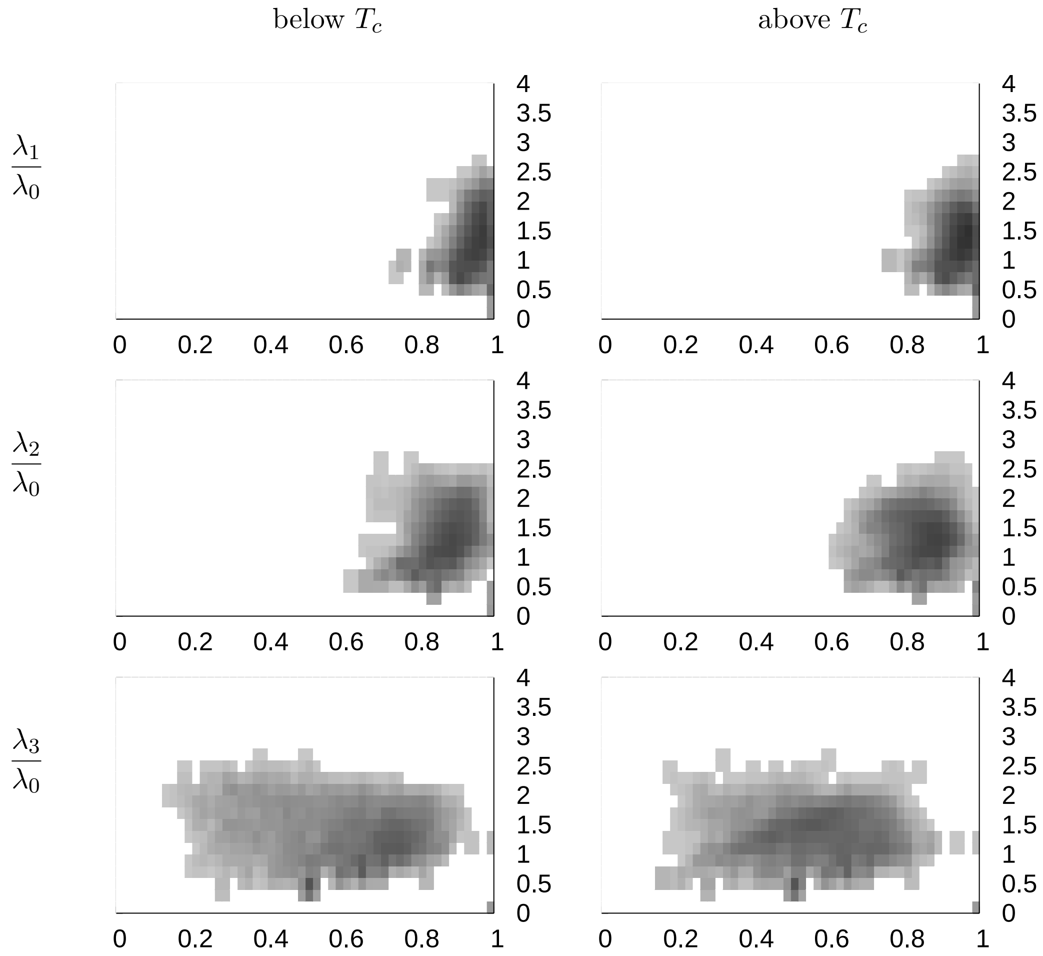

Figure 6.5: The plots show the distribution of cluster moments. The moments are the ratio of eigenvalues of the inertial tensor. The left column shows the results for the ensemble below the critical temperature, the right column shows the ensemble above the critical temperature. Both ensembles consist of 100 configurations with an inverse coupling of $\beta = 1.95$ and a spatial lattice size of 16^3. Above T_c, the temporal lattice size is 4, below the critical temperature, it is 12. The abscissa in all plots shows the ratio of eigenvalues, the ordinate shows $\log_{10}(n)$, with n being the number of points in a cluster. The grayness in the scatter plot encodes the number of clusters in each bin on a logarithmic scale. The eigenvalues are named λ_0 to λ_3, with λ_0 being the largest and λ_3 being the smallest eigenvalue. From the above plots, we can conclude that the clusters have a slight tendency towards a prolate shape.

6.3 Caloron model configurations

In simple words, a caloron is a classical solution of the field equations at finite temperature. Calorons are localized objects with a non-trivial inner substructure. For a more in-depth introduction to calorons see Chapter 7, “Models for topological objects”, Section 7.5, “Caloron model configurations”.

As a cross check, we also made a cluster analysis for configurations provided by Philipp Gerhold *et al.*, given in [39]. These are caloron model configurations. Caloron models have been discussed in, e.g, [40].

The comparison is interesting, because we can test if the caloron model configurations reproduce the exponent ξ for the thermalized and filtered configurations. In Figure 6.6 we see the cluster analysis for three caloron model configurations – above, at, and below the critical temperature. The first thing to notice is that we can indeed see a power-law in all plots. As usual, the power-law is only present for small numbers of points. When we compare the exponent of the power law for the three ensembles, there is little difference. This is consistent with the findings for thermalized configurations. The difference between the thermalized configurations and the caloron model configurations is a peculiar "bump" in the cluster distribution. This bump is probably due to numerical noise when we have already identified all real calorons, and new clusters emerge from the numerical noise at very small cutoffs. If we look at Figure 6.7, we can see that the caloron model configurations look quite different from the thermalized configurations. The caloron configurations are mostly empty, with few interspersed lumps. Since the size of the individual caloron is not much larger than the distance between two lattice points, the interpretation of the results is not easy. For the cluster analysis to work correctly, the clusters should be considerably larger than the lattice size. Otherwise, very small clusters will just appear as lattice artifacts and will appear to be white noise.

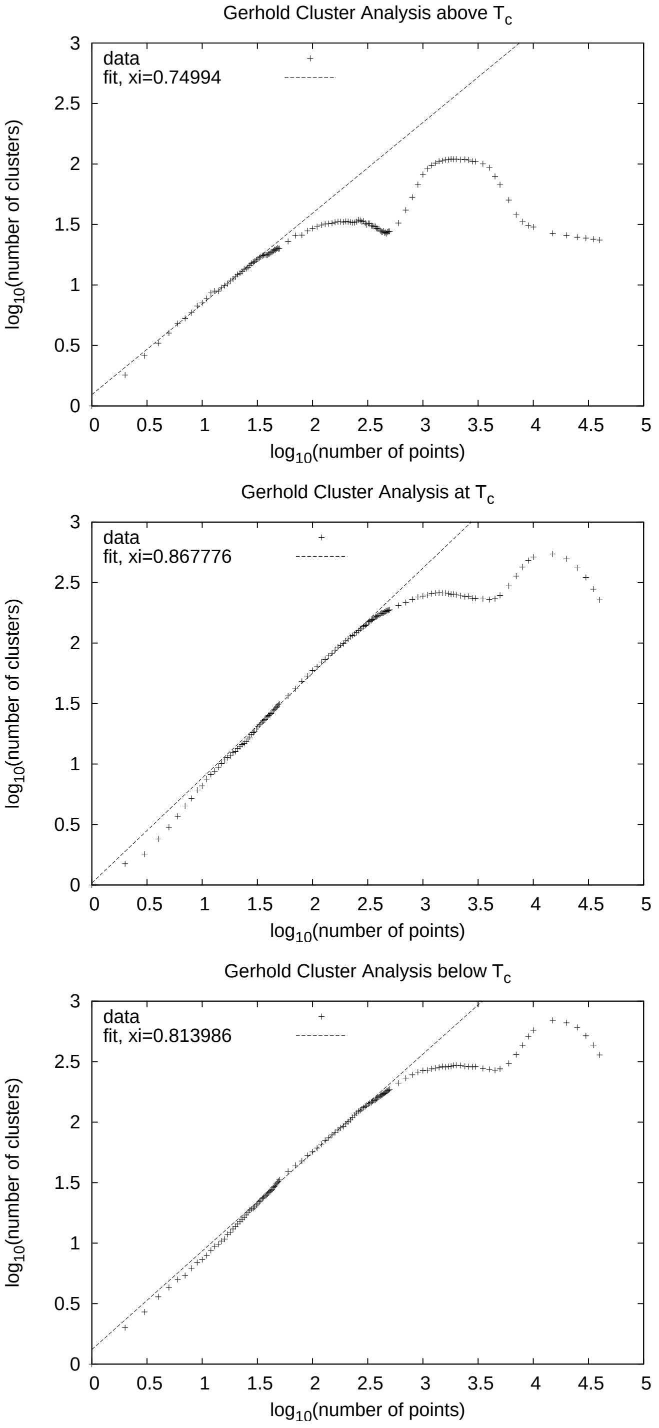

Figure 6.6: The plots above show the cluster distribution for caloron model configurations. The “bump” in the distribution is probably due to numerical noise. The exponent ξ of the power-law is higher than for thermalized and filtered configurations and does not vary much with temperature.

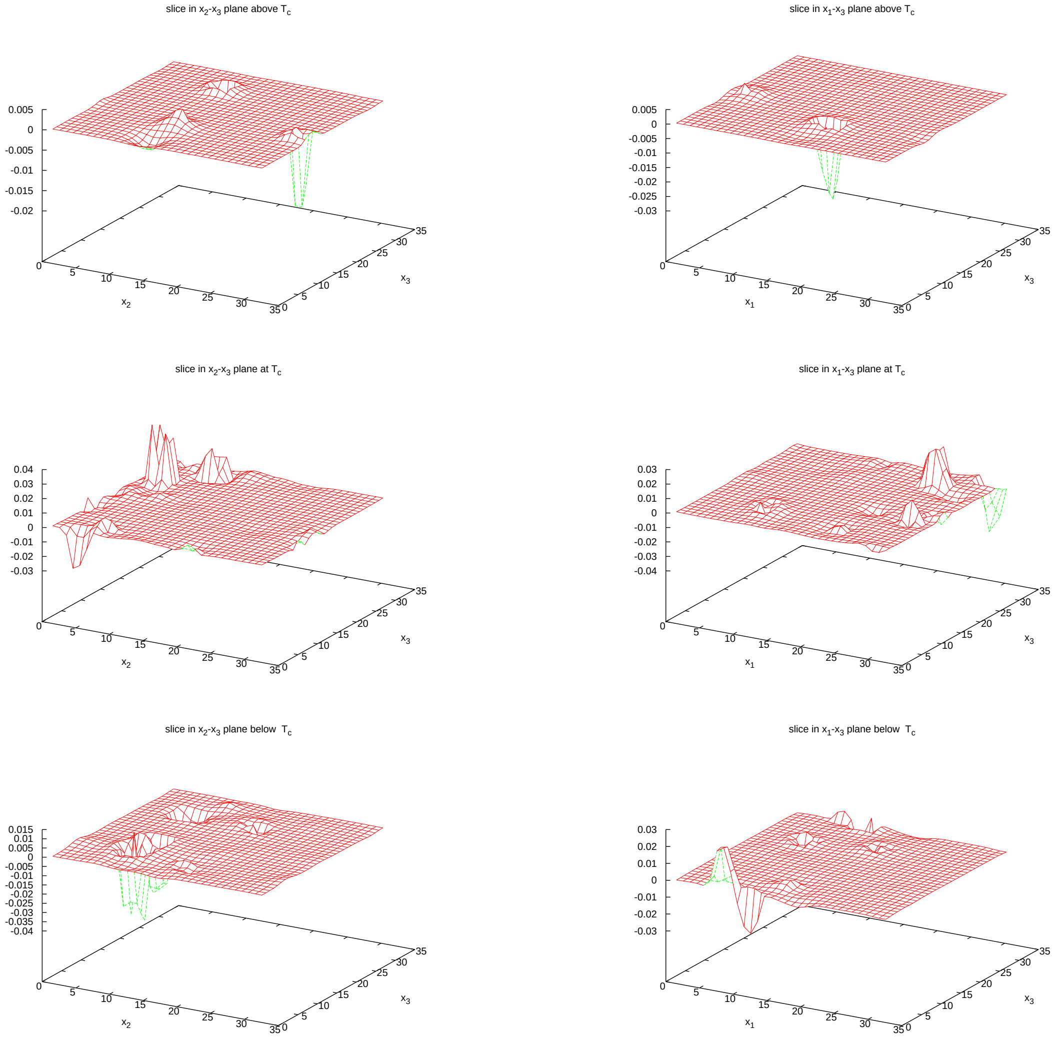

Figure 6.7: This figure shows some slices in caloron model configurations. Each plot is a 2-dimensional slice of the topological charge density within the 4-dimensional volume.

Chapter 7

Models for topological objects

7.1 Monopoles

7.1.1 Monopole definition

For the $SU(2)$ gauge group, a link can be written as

$$U = \begin{pmatrix} \cos(\varphi)\; e^{-i\theta} & \sin(\varphi)\; e^{-i\chi} \\ -\sin(\varphi)\; e^{i\chi} & \cos(\varphi)\; e^{i\theta} \end{pmatrix} \tag{7.1}$$

Typically, monopoles are identified after fixing to a suitable gauge. Normally, this would be the maximal Abelian gauge (MAG). It brings links to being close to a diagonal matrix. In other words, φ should be close to 0 or π. The functional

$$\begin{aligned} F^{\mathrm{MAG}}[U] =& \sum_{x\in\Lambda}\sum_{\mu=1}^{4} \left\{ U_\mu(x)\,\sigma_3\, U_\mu^\dagger(x)\,\sigma_3 \right\} && (7.2) \\ =& 2\cos(2\varphi) && (7.3) \end{aligned}$$

is used to fix the MAG. The Abelian projection is given by:

$$\begin{aligned} SU(2) &\to U(1) && (7.4) \\ U &\mapsto e^{i\theta}\ . && (7.5) \end{aligned}$$

It is convenient to use the θ directly instead of doing the calculations with the $e^{i\theta}$. (Note: θ is a real-valued 1-form on the lattice.) We define a $U(1)$ plaquette ϑ in the usual way:

$$\begin{aligned} \vartheta(x) &= \mathrm{d}\,\theta(x) && (7.6) \\ \vartheta_{\mu\nu}(x) &= \partial_{[\mu}\theta_{\nu]}(x) && (7.7) \\ &= \theta_\mu(x) + \theta_\nu(x+\hat\mu) - \theta_\mu(x+\hat\nu) - \theta_\nu(x)\ . && (7.8) \end{aligned}$$

Note: ϑ is a real-valued 2-form on the lattice. Since θ lies in the range $[-\pi, +\pi)$, ϑ lies in the range $[-4\pi, +4\pi)$. We can now split ϑ in a "photonic" part $\overline{\vartheta}$ and a "monopole" part m, following [41, 42, 43].

$$\begin{aligned} \vartheta(x) &= \overline{\vartheta}(x) + 2\pi\, k(x) && (7.9) \\ \vartheta_{\mu\nu}(x) &= \overline{\vartheta}_{\mu\nu}(x) + 2\pi\, k_{\mu\nu}(x)\ , && (7.10) \end{aligned}$$

with $\overline{\vartheta}$ being in the range $[-\pi, +\pi)$. The monopole content m in the 3-cube at x as:

$$\begin{aligned} m(x) &= \mathrm{d}\,k(x) && (7.11) \\ m_{\lambda\mu\nu}(x) &= \epsilon_{\lambda\mu\nu}\partial_\lambda k_{\mu\nu}(x) + \epsilon_{\nu\lambda\mu}\partial_\nu k_{\lambda\mu}(x) + \epsilon_{\mu\lambda\nu}\partial_\mu k_{\lambda\nu}(x) && (7.12) \\ &= \epsilon_{\lambda\mu\nu}\Big(k_{\mu\nu}(x) - k_{\mu\nu}(x+\hat\lambda)\Big) + && (7.13) \\ &\quad\ \epsilon_{\nu\lambda\mu}\Big(k_{\lambda\mu}(x) - k_{\lambda\mu}(x+\hat\nu)\Big) + \\ &\quad\ \epsilon_{\mu\lambda\nu}\Big(k_{\lambda\nu}(x) - k_{\lambda\nu}(x+\hat\mu)\Big) \end{aligned}$$

where ϵ is the antisymmetric tensor, and the indices are *not* summed over. Note: m is a 3-form on the lattice. We can define the form $\vec{j}$ dual to m, i.e., $\vec{j} = *m$. Then $\vec{j}$ is a

1-form on the dual lattice. We will call $\vec{\jmath}$ the monopole current. It is easy to show that the monopole currents are conserved:

$$\begin{aligned}\delta\vec{\jmath} &= (-1)^3 * \mathrm{d} *^{-1} \vec{\jmath} \\ &= (-1)^3 * \mathrm{d} *^{-1} * m \\ &= (-1)^3 * \mathrm{d} *^{-1} * \mathrm{d}\, k \\ &= (-1)^3 * \mathrm{d}\,\mathrm{d}\, k \\ &= 0 \quad .\end{aligned}$$

In coordinates:

$$\begin{aligned}(-1)^3\delta\vec{\jmath} &= * \mathrm{d} *^{-1} \vec{\jmath} && (7.14)\\ &= * \mathrm{d} *^{-1} * m && (7.15)\\ &= * \mathrm{d}\, m && (7.16)\\ &= \partial_1 m_{234} - \partial_2 m_{134} + \partial_3 m_{124} - \partial_4 m_{123} && (7.17)\\ &= \quad \partial_1(\partial_2 k_{34} - \partial_3 k_{24} + \partial_4 k_{23}) - \partial_2(\partial_1 k_{34} - \partial_3 k_{14} + \partial_4 k_{13}) && (7.18)\\ &\quad +\partial_3(\partial_1 k_{24} - \partial_2 k_{14} + \partial_4 k_{12}) - \partial_4(\partial_1 k_{23} - \partial_2 k_{13} + \partial_3 k_{12}) \\ &= \quad \partial_1\partial_2 k_{34} - \partial_1\partial_3 k_{24} + \partial_1\partial_4 k_{23} - \partial_2\partial_1 k_{34} + \partial_2\partial_3 k_{14} - \partial_2\partial_4 k_{13} && (7.19)\\ &\quad +\partial_3\partial_1 k_{24} - \partial_3\partial_2 k_{14} + \partial_3\partial_4 k_{12} - \partial_4\partial_1 k_{23} + \partial_4\partial_2 k_{13} - \partial_4\partial_3 k_{12} \\ &= 0 \quad . && (7.20)\end{aligned}$$

7.1.2 Separating the Abelian field into a photon and a monopole contribution

Inverse of the lattice Laplacian

Lattice Laplacian:

$$\Delta^{\text{lat.}}(x,y) = \sum_{\mu=1}^{4} \delta(x + a\hat{\mu},\, y) + \delta(x - a\hat{\mu},\, y) - 2\delta(x,y) \tag{7.21}$$

Fourier Transform:

$$\begin{aligned}\widetilde{\Delta}^{\text{lat.}}(p,q) =& \sum_{x\in\Lambda}\sum_{y\in\Lambda}\sum_{\mu=1}^{4} \\ & \Big\{e^{-ixp}e^{iyq}\left(\delta(x + a\hat{\mu},\, y) + \delta(x - a\hat{\mu},\, y) - 2\delta(x,y)\right)\Big\} && (7.22)\\ =& \sum_{x\in\Lambda}\sum_{y\in\Lambda}\sum_{\mu=1}^{4} \\ & \Big\{e^{-ipx}e^{+iqx}e^{+iqa\hat{\mu}} + e^{-iqx}e^{+iqx}e^{-iqa\hat{\mu}} - 2e^{-ipx}e^{+iqx}\Big\} && (7.23)\\ =& \sum_{x\in\Lambda}\sum_{y\in\Lambda}\sum_{\mu=1}^{4} e^{-ipx}e^{+iqx}\Big\{e^{iaq_\mu} + e^{-iaq_\mu} - 2\Big\} && (7.24)\\ =& \sum_{\mu=1}^{4} 2\Big\{\cos\left(aq_\mu\right) - 1\Big\}\sum_{x\in\Lambda} e^{-ix(p-q)} && (7.25)\\ =& 2\,V\delta(p-q)\sum_{\mu=1}^{4}\Big\{\cos\left(aq_\mu\right) - 1\Big\} && (7.26)\end{aligned}$$

With this result, we can now easily write down the Green's function in momentum space. It is simply the inverse of the lattice Laplacian in momentum space:

$$\widetilde{G}^{\text{lat.}}(p,q) = \delta(p-q)\frac{1}{2\,V\,\sum_{\mu=1}^{4}\big(\cos(aq_\mu)-1\big)}. \tag{7.27}$$

However, there is a problem if we use periodic boundary conditions. In this case, the Green's function has a pole at $p_\mu = 0$. We will show in a moment that we can approximate the Green's function at periodic boundary conditions if we simply leave out the term containing the pole. Thus, we define the approximate Green's function in momentum space as:

$$\widetilde{G}^{\text{lat.}}_{\text{approx.}}(p,q) = \begin{cases} \widetilde{G}^{\text{lat.}}(p,q) & \text{if } q \neq 0 \\ 0 & \text{if } q = 0 \end{cases}. \tag{7.28}$$

Now we can write the Green's function in coordinate space via a Fourier transform:

$$\begin{aligned} G^{\text{lat.}}_{\text{approx.}}(x,y) &= \sum_{p\in\Pi}\sum_{\substack{q\in\Pi\\ q\neq 0}} e^{ipx}e^{-iqy}\frac{\delta(p-q)}{2\,V\,\sum_{\mu=1}^{4}\{\cos(aq_\mu)-1\}} && (7.29)\\ &= \sum_{\substack{p\in\Pi\\ p\neq 0}} \frac{e^{ipx}e^{-ipy}}{2\,V\,\sum_{\mu=1}^{4}\{\cos(ap_\mu)-1\}} && (7.30)\\ &= \sum_{\substack{p\in\Pi\\ p\neq 0}} \frac{e^{ip(x-y)}}{2\,V\,\sum_{\mu=1}^{4}\{\cos(ap_\mu)-1\}} && (7.31)\end{aligned}$$

Note the approximation we make for periodic boundary conditions is simply to leave out the term where $p = 0$. If we have other boundary conditions, this approximation is unnecessary.

We will now show that the above approximation is exact in the infinite volume limit, $V \to \infty$.

A few general remarks: For a differential operator $\Delta^{\text{lat.}}$ on the lattice, there is a "Green's function" $G^{\text{lat.}}$ such that we can formally write:

$$\sum_{z\in\Lambda}\Delta^{\text{lat.}}(x,z)\,G^{\text{lat.}}(z,y) = \delta(x,y)\ .$$

This allows us to calculate solutions g of the equation

$$\sum_{y\in\Lambda}\Delta^{\text{lat.}}(x,y)\,g(y) = h(x)$$

via

$$g(x) = \sum_{y\in\Lambda} G^{\text{lat.}}(x,y)h(y)\ .$$

In other words,

$$\sum_{z\in\Lambda}\sum_{y\in\Lambda}\Delta^{\text{lat.}}(x,z)\,G^{\text{lat.}}(z,y)\,h(y) = h(x)\ .$$

When we apply the general statement above to the (approximated) lattice Laplacian, we get the following:

$$
\begin{aligned}
&\sum_{z\in\Lambda}\sum_{y\in\Lambda}\Delta^{\text{lat.}}(x,z)\,G^{\text{lat.}}_{\text{approx.}}(z,y)\,h(y) = \\
&= \sum_{z\in\Lambda}\sum_{\nu=1}^{4}\sum_{y\in\Lambda}\left(\delta(x+a\hat{\nu},z)+\delta(x-a\hat{\nu},z)-2\delta(x,z)\right)\cdot \\
&\quad\cdot\sum_{\substack{p\in\Pi\\ p\neq 0}}\frac{e^{ip(z-y)}}{2\,V\,\sum_{\mu=1}^{4}\{\cos(ap_\mu)-1\}} \\
&= \sum_{\nu=1}^{4}\sum_{y\in\Lambda}h(y)\sum_{\substack{p\in\Pi\\ p\neq 0}}\frac{e^{ip(x-y+a\hat{\nu})}+e^{ip(x-y-a\hat{\nu})}-2e^{ip(x-y)}}{2\,V\,\sum_{\mu=1}^{4}\{\cos(ap_\mu)-1\}} \\
&= \sum_{y\in\Lambda}h(y)\sum_{\substack{p\in\Pi\\ p\neq 0}}\frac{e^{ip(x-y)}}{V}\frac{2\,\sum_{\nu=1}^{4}\{\cos(ap_\nu)-1\}}{2\,\sum_{\mu=1}^{4}\{\cos(ap_\mu)-1\}} \\
&= \sum_{y\in\Lambda}h(y)\left\{\left(\sum_{\substack{p\in\Pi\\ p\neq 0}}\frac{e^{ip(x-y)}}{V}\right)+\frac{1}{V}-\frac{1}{V}\right\} \\
&= \sum_{y\in\Lambda}h(y)\left\{\left(\sum_{p\in\Pi}\frac{e^{ip(x-y)}}{V}\right)-\frac{1}{V}\right\} \\
&= \sum_{y\in\Lambda}h(y)\left\{\delta(x-y)-\frac{1}{V}\right\} \\
&= h(x)-\frac{1}{V}\sum_{y\in\Lambda}h(y)\;.
\end{aligned}
$$

Thus, we may formally write

$$\Delta^{\text{lat.}}G^{\text{lat.}}_{\text{approx.}} = \delta-\frac{1}{V}\;.$$

Note that the $\frac{1}{V}$ term is the only effect of the approximation and it only appears for periodic boundary conditions. The final result,

$$\sum_{z\in\Lambda}\sum_{y\in\Lambda}\Delta^{\text{lat.}}(x,z)\,G^{\text{lat.}}_{\text{approx.}}(z,y)\,h(y) = h(x)-\frac{1}{V}\sum_{y\in\Lambda}h(y) \tag{7.32}$$

tells us that the approximation is indeed exact in the infinite volume limit $V\to\infty$ as long as the function h falls off at infinity fast enough.

A bit of Hodge theory

The *Hodge decomposition* states that on a closed, n-dimensional manifold, any k-form ω can be written as

$$\omega = \mathrm{d}\,\alpha+\delta\,\beta+h \tag{7.33}$$

where

$\mathrm{d} : \Omega^k \longrightarrow \Omega^{k+1}$	is the external derivative,
$\delta : \Omega^k \longrightarrow \Omega^{k-1}$	is the co-derivative, with
$\delta = * \, \mathrm{d} \, *$	with
$* : \Omega^k \longrightarrow \Omega^{n-k}$	is the Hodge star operator on a n-dimensional manifold,
α	is a $k-1$ form,
β	is a $k+1$ form,
h	is a harmonic form, i.e.,
$\delta \, h = \mathrm{d} \, h = 0$	.

Details can be found in [44] or [45].

Let us write the lattice 1-form θ using the Hodge decomposition:

$$\theta = \mathrm{d}\,\alpha + \delta\,\beta + h$$

Then, we apply the Laplace-Beltrami operator on both sides:

$$\begin{aligned} \Delta\theta &= \Delta\,\mathrm{d}\,\alpha + \Delta\,\delta\,\beta + \Delta h \\ &= \big(\mathrm{d}\,\delta + \delta\,\mathrm{d}\big)\,\mathrm{d}\,\alpha + \big(\mathrm{d}\,\delta + \delta\,\mathrm{d}\big)\,\delta\,\beta + \Delta h \\ &= \mathrm{d}\,\delta\,\mathrm{d}\,\alpha + \delta\,\mathrm{d}\,\delta\,\beta \end{aligned}$$

Now compare this to the lattice 2-form ϑ:

$$\begin{aligned} \vartheta &= \mathrm{d}\,\theta \\ &= \mathrm{d}\left(\mathrm{d}\,\alpha + \delta\,\beta + h\right) \\ &= \mathrm{d}\,\delta\,\beta \end{aligned}$$

We see that

$$\Delta\theta = \delta\,\vartheta \text{ iff } \mathrm{d}\,\delta\,\mathrm{d}\,\alpha \equiv 0 \quad .$$

This can be regarded as gauge fixing. More precisely, since

$$\begin{aligned} \Delta\theta &= \mathrm{d}\,\delta\,\theta + \delta\,\mathrm{d}\,\theta \\ &= \mathrm{d}\,\delta\,\theta + \delta\,\vartheta \quad , \end{aligned}$$

this means that $\mathrm{d}\,\delta\,\theta \equiv 0$. This is the Landau gauge condition. See [40] for lattice results on monopoles.

7.2 Vortices

7.2.1 Introduction

Vortices are two-dimensional topological objects. In lattice gauge theory, “vortices” is often used equivalently for “p-vortices.” The p-vortices are infinitely thin objects that live on the dual lattice. In contrast to the p-vortices on the lattice, vortices in the continuum are also 2-dimensional closed objects. However, they consist of patches of oriented surfaces, i.e., there is an “outer” and an “inner” side of the vortex surface at a given point. In terms of gauge fields, they are described as surfaces of electromagnetic flux [46]. It can be shown that they carry topological charge and the zero-modes of the Dirac operator can be calculated analytically [47]. On the lattice, however, the p-vortices do not have any orientation. For completeness, I want to mention that also thick vortices can be constructed. Thick vortices also give rise to zero-modes of the Dirac operator [48]. These consist of Abelian gauge fields. For an investigation of thin and thick vortices using the Chirally Improved lattice Dirac operator, see [49, 8].

P-vortices are detected by projection on the $\mathbb{Z}_2$ group, usually after a suitable gauge fixing. Commonly gauges are either the maximal center gauge or indirect center gauge.

The condition for the maximal center gauge reads:

$$\sum_{\mu,\,x} \left[U_\mu(x) - Z_\mu(x)\right]^\dagger \left[U_\mu(x) - Z_\mu(x)\right] \longrightarrow \text{ minimum.} \tag{7.34}$$

With $Z_\mu(x) = \operatorname{sign} \operatorname{Re} \operatorname{tr} U_\mu(x)$. This gauge brings the links $U_\mu(x)$ close to a center element. Keep in mind, for the gauge group $SU(2)$, the center is $\pm\mathbb{1}$. For details see e.g., [50, 51]. After projection on $\mathbb{Z}_2$, the gauge links are either $+1$ or -1. Now, plaquettes are evaluated. Obviously, a single plaquette can be either $+1$ or -1. Vortices are then identified on the dual lattice: A plaquette on the dual lattice that is pierced by a plaquette of value -1 is said to belong to a vortex. Other plaquettes on the dual lattice do not belong to a vortex. By construction, it can be shown that vortices on the dual lattice are always closed surfaces. The smallest possible vortex is a single cube on the dual lattice. It is induced by a single negative link on the real lattice. Figure 7.1 illustrates this smallest vortex. Then, if more negative links are added on the real lattice, more cubes are induced on the dual lattice, with the 'inner' surfaces removed. Thus, vortices are closed, two-dimensional surfaces on the dual lattice.

Figure 7.1: This figure shows the smallest possible Vortex. It is the vortex induced by a single negative link. The negative plaquettes attached to a single negative link are shown in red. The vortex on the dual lattice is shown in blue. Assume the negative link points in the z-direction. The left hand side picture shows four of the six vortex plaquettes, piercing the spatial plaquettes. The right hand side picture shows all six vortex plaquettes. Those vortex plaquettes drawn at a distance above and below the others are pierced by the negative plaquettes in the temporal direction.

Vortices can be used to explain confinement. Suppose we compute a Wilson loop $\mathcal{W}$ in a configuration where all links are in the center:

$$\mathcal{W} = \prod_{l\in\mathcal{C}} Z_l$$

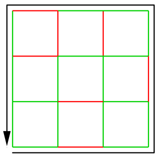

The Wilson loop W is the product of links l in the contour $\mathcal{C}$. Negative links are shown red, positive links are green.

$$\mathcal{W} = \prod_{l\in\mathcal{C}} Z_l = \prod_{p\in\mathcal{A}} \prod_{l\in p} Z_l$$

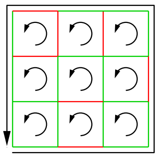

The links l in the contour $\mathcal{C}$ enclose an area $\mathcal{A}$. W is also the product of all plaquettes p, since the links are in the center and commute.

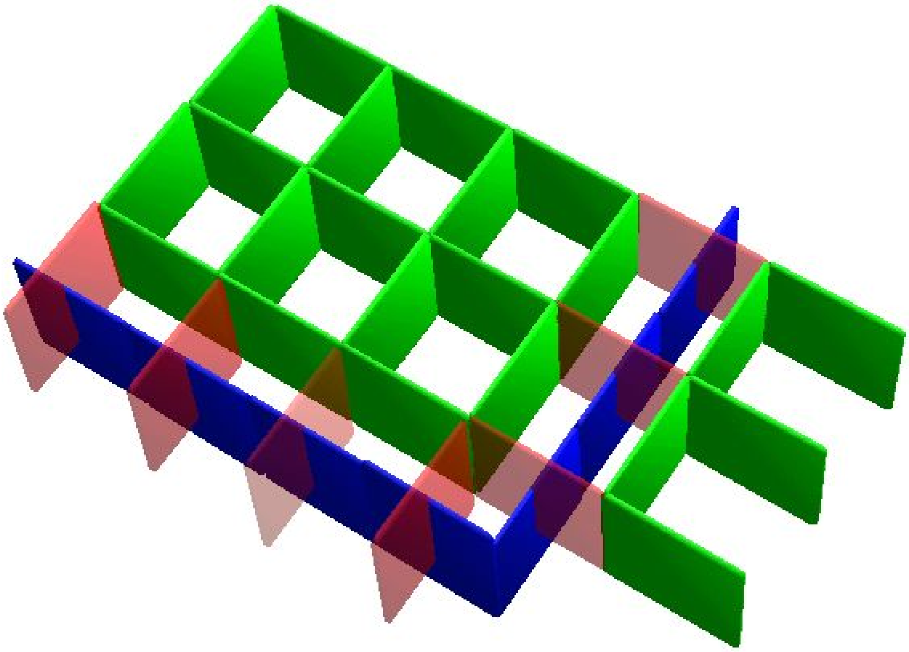

Figure 7.2: This figure is an artist's impression of a vortex. The green plaquettes evaluate to +1, the red plaquettes evaluate to −1. The vortex, living on the dual lattice, pierces those plaquettes that evaluate to −1.

$$\mathcal{W} = \prod_{l\in\mathcal{C}} Z_l = \prod_{p\in\mathcal{A}}\prod_{l\in p} Z_l = \prod_{p\in\mathcal{A}} v(p)$$

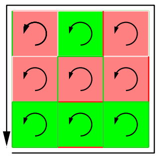

W is also the product of all plaquette values $v(p)$, where $v(p)$ is ±1, depending if a plaquettes is pierced by a vortex or not.

Confinement means that the expectation value for the Wilson loop obeys an area law, $\langle\mathcal{W}\rangle \propto e^{-\sigma\mathcal{A}}$, where σ is the string tension and $\mathcal{A}$ is the area enclosed by the contour $\mathcal{C}$. Now assume that the vortices are randomly distributed. Then the expectation value if a plaquette is $\langle v\rangle = 1 - 2f$ where f is the probability that a vortex pierces a plaquette. Therefore, the expectation value of the Wilson loop can be expressed in terms of that probability f:

$$\begin{aligned} \langle\mathcal{W}\rangle &= \left\langle \prod_{l\in\mathcal{C}} Z_l \right\rangle = \left\langle \prod_{p\in\mathcal{A}} v(p) \right\rangle = (1-2f)^{\mathcal{A}} = \exp\{\ln(1-2f)\mathcal{A}\} = \exp\{-\sigma\mathcal{A}\} \\ &\text{and} \\ \langle\mathcal{W}\rangle &= \sum_n (-1)^n \, P(n) \end{aligned} \tag{7.35}$$

with $\sigma = -\ln(1-2f)$ and $P(n)$ being the probability that n vortices pierce the Wilson loop.

It has been shown that vortices reproduce the string tension of $SU(2)$ gauge field configurations almost entirely [52]. Chiral symmetry breaking can also be modeled with the vortex description, see [53, 54].

The phase transition from the confined to the deconfined phase transition can be explained as follows: In the confined phase, vortices percolate and are randomly distributed. According to Eq. (7.35) this implies an area law for the Wilson loop and confinement. In the deconfined phase, the vortices tend to form pairs. This means that a pair of vortices that pierces a Wilson loop does not contribute to the expectation value of the Wilson loop. Only pairs of vortices where one vortex is outside and one is inside the Wilson loop contribute. This gives rise to a perimeter law of the Wilson loop and confinement is lost. A quantity that can be measured is the pairing ratio of vortices:

$$r_P = \frac{\langle N_{\text{even}} \rangle}{\langle N_{\text{even}} \rangle \; \langle N_{\text{odd}} \rangle} \tag{7.36}$$

Figure 7.3 shows a measurement and an illustration.

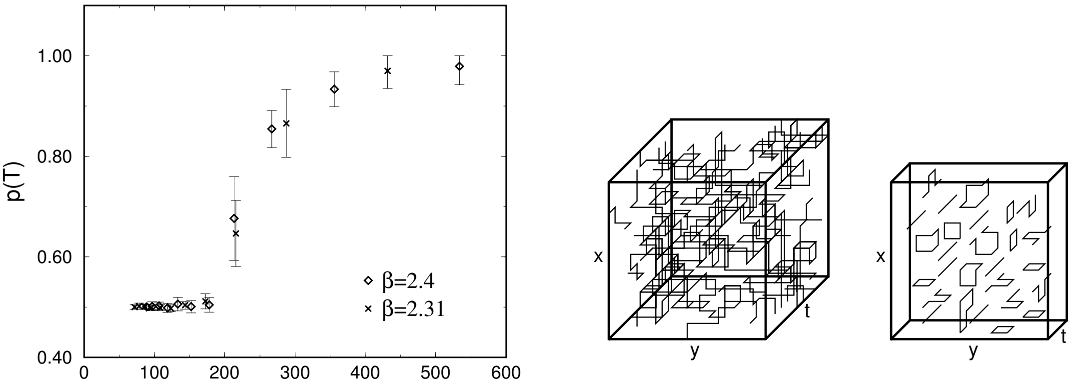

confined phase

deconfined phase

Figure 7.3: The left plot shows a measurement of the vortex pairing ratio, given in Eq. (7.36). The plot is taken from [52]. The middle illustration shows a schematic impression of the vortex distribution in the confined phase. Vortices percolate and are randomly distributed throughout the lattice. An illustration for the vortices in the deconfined phase is shown on the right. Vortices tend to appear in pairs. Both illustrations are taken from [55].

7.2.2 Removal of vortices

Vortices can be removed from the lattice by a rather straightforward procedure. It was first introduced in [56]. For the $SU(2)$ group, the method is to multiply the projected lattice link by link with the original gauge fixed lattice. The new, vortex removed lattice still has full $SU(2)$ links. However, if one projects links from the vortex removed lattice on the center of the group, all links will be trivial, i.e., 1. The vortex removed lattices are very different from the original ones. It has been shown that the string tension vanishes on the vortex removed configurations [57]. Furthermore, the eigenvalue spectrum of the Chirally Improved Dirac operator changes fundamentally and resembles the spectrum of the free operator [49].

7.2.3 Pure vortex configurations

There is another way to access vortices in lattice QCD. Instead of looking for vortices in thermalized ensembles of the full gauge group, one can also generate pure vortex configurations [58]. These pure vortex configurations are also generated by a Monte-Carlo process, but use a action specifically targeted at vortices. A flat vortex would have zero action, and every “bend” in the vortex increases the action. Choosing a suitable update algorithm, one can generate thermalized pure vortex configurations.

These vortices can be transferred on a lattice. I was lucky to get a set of pure vortex configurations configurations from M. Engelhardt. Originally, these were configurations at zero temperature and the lattice volume was 3^4. In order to make the configurations accessible for analysis with standard lattice methods, they were put on a finer lattice with a lattice volume of 12^4.

From previous works [49], we knew that the analysis of pure $Z(2)$ configurations with the CI operator is tricky, of not impossible. However, thick vortex configurations can be analyzed with the CI operator. The idea was, to treat the pure vortex $Z(2)$ configurations with standard techniques in the hope that thick vortices would emerge from the p-vortices. Visually speaking, we were trying to grow “flesh” on the vortex “bones.”

In spite of many attempts to produce sensible results, I did not manage to produce physically meaningful $SU(2)$ configurations from the $Z(2)$ configurations. The techniques used were heating followed by Metropolis cooling. In this context, *heating* must means a series of regular gauge updates using the standard Monte-Carlo gauge updates as described in Eq. (4.6) and Section 3.3.2, “The Metropolis Algorithm.” The *cooling* used here is a technique often called Hioki-cooling [59]. It consists of the same gauge updates as the Metropolis algorithm used for heating, but now only gauge updates that lower the action are accepted. Gauge updates that increase the action are always discarded during cooling. The heating step is indeed necessary – for a pure $Z(2)$ gauge field configuration, any gauge update of the from Eq. (4.6) would increase the action. Therefore, we choose to heat the configurations first.

The benchmark I used was not a p-vortex configuration produced with a vortex action. The results from these turned out to be very difficult to interpret. Instead, I took the simplest non-trivial case of a vortex configuration. That is, a configuration with four vortex sheets that are pairwise parallel and flat. Such a configuration has four vortex intersection points. I will call this the test configuration for the remainder of this section. Since the p-vortices do not have oriented surfaces, the topological charge of the test configuration is not determined. The hope was, that a treatment with heating and subsequent cooling would produce sensible $SU(2)$ gauge configurations. Table 7.1 shows the results. The values of the topological charge determined from the zero-modes of the CI operator are listed for various numbers of heating steps and various seeds for the random number generator.

What we find is, that the fermionic topological charge varies greatly depending on the number of heating steps and – worse – varies with the seed of the random number generator. This is a clear indication that the method pursued does not yield physically sensible results. Moreover, the values obtained for the topological charge are not in accordance with the vortex model. The test configuration has four vortex intersection points. Every intersection point can contribute $\pm\frac{1}{2}$ to the topological charge. If the vortex sheets would have gained a uniform orientation, the topological charge should take on values of 0 or ± 2. If the vortex sheets were not uniformly oriented and consisted instead of patches of different orientations, values of 0, ± 1, or ± 2 are possible. Yet, we see values of ± 3 and even 4 for the topological charge.

An inspection by eye of the generated configurations did not look so bad. The scalar density of the lowest Dirac eigenmode showed peaks in the vicinity of the vortex intersection points and so did the action density. An example of the slices is shown in Figure 7.4. But a rough agreement is not enough for a sensible analysis. The conclusion of this section is, that pure vortex configurations are not suitable to be analyzed with the CI operator, even after heating and cooling.

7.3 Instantons

Instantons are a widely applied model for topological objects [38, 60]. They are solutions of the classical (euclidean) field equations at zero temperature. As such, they represent a minimum of the action. The explicit form of an instanton in regular gauge with the size

heating steps	random seed									
	1000	1001	1002	1003	1004	1005	1006	1007	1008	1009
1	+1	-3	+2	+2	+1	-2	+3	+2	+2	+1
2	-0	-1	-0	-0	-0	-3	-0	-1	+1	-1
3	-1	+1	-0	+1	+1	-2	-0	+3	-0	-1
4	+1	+1	-1	-3	-1	+2	-3	-0	-1	-2
5	+2	+1	+1	+2	-1	+3	-0	+1	+1	-1
10	-0	+2	-2	-1	-3	+2	-2	-0	-0	-1
15	+1	-2	-0	-3	-2	-1	-0	+3	+2	+1
25	-1	+2	-1	-3	-2	-0	-2	+2	+1	-2
50	+1	+1	-3	-4	-0	-0	-1	+2	-3	-1
100	-1	-0	-0	-1	-0	-0	-2	-0	-3	-0

Table 7.1: This table shows the fermionic topological charge for the test configuration after heating and cooling. We varied the number of heating steps and varied the seed of the random number generator for the Metropolis algorithm. The heating phase was followed by 1000 cooling steps.

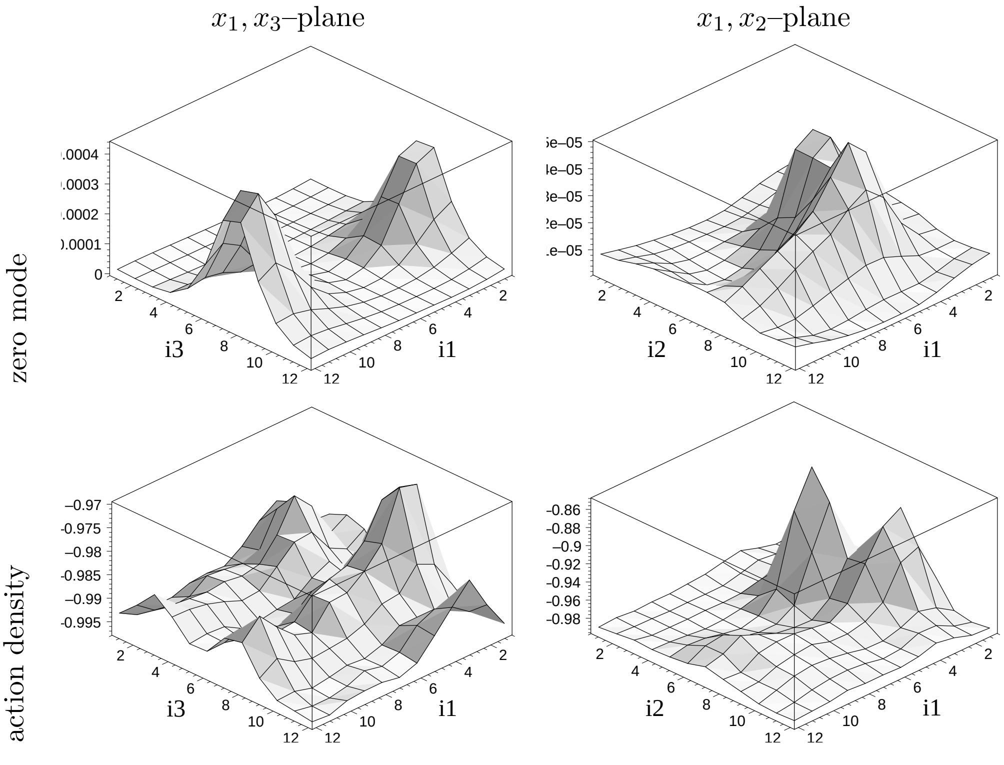

x_1, x_3–plane

x_1, x_2–plane

Figure 7.4: This figure shows slices of the vortex-only test configuration. The top row shows two slices of the zero mode scalar density, the bottom row shows slices of the action density. All slices go through the point (3, 3, 3, 3) which should be a vortex intersection point. Both the scalar density of the zero mode and the action density show some localization properties. However, the localization is not consistent between the two densities.

parameter ρ – the Belavin-Polyakov-Schwartz-Tyupkin instanton solution [61] is:

$$A^a_\mu(x) = \frac{2\eta_{a\mu\nu}\, x_\nu}{x^2 - \varrho^2}, \qquad \eta_{a\mu\nu} = \begin{cases} \epsilon_{a\mu\nu}, & \mu,\, \nu = 1,2,3, \\ \delta_{a\mu}, & \nu = 4, \\ -\delta_{a\nu}, & \mu = 4. \end{cases}$$

An anti-instanton is given by (7.37)

$$A^a_\mu(x) = \frac{2\overline{\eta}_{a\mu\nu}\, x_\nu}{x^2 - \varrho^2}, \qquad \overline{\eta}_{a\mu\nu} = \begin{cases} \epsilon_{a\mu\nu}, & \mu,\, \nu = 1,2,3, \\ -\delta_{a\mu}, & \nu = 4, \\ \delta_{a\nu}, & \mu = 4. \end{cases}$$

Note that the field of an (anti)-instanton is (anti)-selfdual, i.e., $F_{\mu\nu} = \pm\widetilde{F}_{\mu\nu}$. From the above equation, one can derive the action density of an instanton:

$$\Big(F^a_{\mu\nu}(x)\Big)^2 = \frac{192\varrho^2}{(x^2 - \varrho^2)^4} \quad . \tag{7.38}$$

The parameter ϱ called the size parameter of the instanton. It is well known that the Dirac operator in the presence of a single instanton has one exact zero-mode. According to the Atiyah-Singer index theorem (see Eq. (2.35)) this means the underlying gauge field has a topological charge of ±1. It can also be shown [62] that the Dirac operator has two near-zero modes in the presence of a two-instanton gauge field. Figure 7.5 shows a pictogram of the mode splitting.

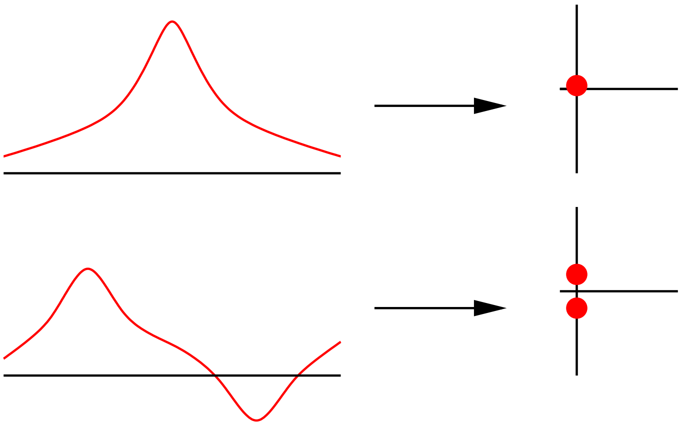

Figure 7.5: This schematic figure shows schematically how a single instanton leads to a single zero mode in the spectrum of the Dirac operator. Two instantons lead to two near-zero modes.

These results can be generalized: The Dirac operator builds up a density of near zero modes for a many-instanton gauge field. This density of zero modes is an order parameter for chiral symmetry breaking, according to the Banks-Casher relation [63]. The Banks-Casher relation [63] reads

$$\langle\bar{\psi}\psi\rangle = -\lim_{m\to 0}\int \mathrm{d}\,\mu\;\rho(\mu)\,\frac{m}{\mu^2 + m^2} = -\pi\;\rho(0) \quad , \tag{7.39}$$

with m being the mass, $\rho(\mu)$ the density of eigenvalues μ averaged over gauge-fields. In the above formula, the Dirac operator in the continuum $\not{D}$ has only imaginary eigenvalues $i\mu$ with $\mu \in \mathbb{R}$. Since the chiral condensate $\langle\bar{\psi}\psi\rangle$ is an order parameter for the breaking of the chiral symmetry, a non-vanishing density of near-zero modes – $\rho(\mu) \to$ const. as

$\mu \to 0$ – means that the chiral symmetry is broken. Therefore, instantons are very useful in explaining chiral symmetry breaking. Various models for the QCD vacuum based on instantons exist. For a detailed review see [62]. However, instantons have notorious problems explaining confinement [64].

7.4 Calorons

In the previous section, I introduced the instanton as a classical solution to the field equations at zero temperature. The generalization to finite temperature is non-trivial, and several possibilities exist. The first one was the Harrington-Shepard caloron [65]. It is constructed as a superposition of infinitely many instantons in the temporal direction.

The Kraan-van Baal-Lee-Lu caloron [66, 67] (KvBLL caloron) is a more elaborate solution. A difference between the Harrington-Shepard (HS) caloron and the KvB caloron is the behavior of the Polyakov loop at infinite distances. The Polyakov loop at infinite distances is frequently called the *holonomy.* Whereas the HS caloron only allows for trivial holonomy, i.e., the Polyakov loop is in the center of the group at infinite distances, the KvBLL caloron accommodates arbitrary holonomy. For low temperatures, a KvBLL caloron would appear as a single lump of topological charge density, and it would dissociate into two monopoles at high temperatures. Evidences for KvBLL calorons in lattice configurations have been found [68, 40]. In addition, there is evidence for a connection between calorons and confinement [69].

7.5 Caloron model configurations

It is possible to construct caloron model configurations on the lattice, see [39, 70]. They model an ensemble of KvBLL calorons with a distribution of the size parameter. The distribution of the size parameter consists of a power-like behavior for small values of the size parameter, times an exponential cutoff for large size parameters. The discretization of caloron ensembles is highly non-trivial. A simple superposition would not yield self-dual solutions. More sophisticated techniques are deployed. For details see [70]. According to the model given in Chapter 5, “Results at zero temperature and the power-law”, Section 5.5, “A model for the power-law”, the exponent for the power-law in the size parameter of the calorons should be retrieved by the cluster analysis. This is not exactly the case. The cluster analysis of caloron model configuration yields an exponent that is too high. The interpretation is not obvious as several effects can cause a mismatch. One possible explanation is, that the interaction of the calorons within the ensemble gives rise to new clusters. Another explanation would be that the lattices used for the discretization are not fine enough for the cluster analysis to work properly.

7.6 Pseudoparticle approach

Another interesting approach is the pseudoparticle approach [71, 72]. Previous works in this direction include [73, 74]. In this approach, the gauge fields are superpositions if instantons, anti-instantons and akyrons. The latter are similar to instantons in the sense that they are long range gauge fields, but a single akyron has neither a net action nor a topological charge density [71]. We started to study topological densities derived from the pseudoparticle approach. The first results look promising, but I feel that we are not ready for a conclusive statement yet.

Chapter 8

Applications beyond QCD

This chapter is devoted to applications of lattice QCD techniques beyond QCD. The idea was to show that developments that were originally targeted exclusively on QCD can be deployed in completely different fields. The analysis of magnetic resonance imaging data is such a field.

Generally speaking, magnetic resonance imaging takes advantage of the hyperfine structure. For isotopes with half-integer spin, one can observe that the hyperfine levels shift according to several parameters like external magnetic field or chemical environment. If a fixed isotope is targeted – frequently the hydrogen in water – the dependency of the hyperfine shifts on magnetic fields can be used to obtain tomographic images. For a good educational introduction see [75, 76]. This technique is long established in medical science and commercial MRI scanners are readily available. Most devices use echo planar imaging, which allows image acquisition at very high rates.

8.1 Introduction to functional magnetic resonance imaging

The term *functional magnetic resonance imaging* (fMRI) refers to a technique that uses standard magnetic resonance imaging (MRI) to explore the function of organisms. In particular, the the reaction of a given organism to a stimulus varying with time is used to gain deeper insight.

The idea behind fMRI is best illustrated on an example. Suppose we want to find out which region of the brain is responsible for the processing of visual motion information. Then, we would place a test person in an MRI scanner and present a visual stimulus that varies over time. The simplest design is a block design: The test person sees a pattern of moving spots for 20 seconds, then for 20 seconds the spots are at rest. The the spots start moving again and so on. The key to fMRI is the assumption that those regions of the brain that are responsible for the processing of the stimulus change their signature in a way that is correlated to the stimulus. The kind of correlation is not important at the moment. While the test person sees the visual stimulus, a full volume picture of the brain is taken at frequent intervals, e.g., every two seconds. The resulting “volumetric movie” of the brain can then be analyzed for correlations.

We see immediately that this is a problem can can be evaluated separately on every voxel[1] of the MRI image. The analysis if one voxel shows a correlation with the stimulus is independent of the other voxels. Such a problem is frequently called trivially parallelizable.

8.2 Multi parameter fits using SVD

In order to detect correlations, we have to perform a multi-parameter fit to the measured data. Keep in mind that this can be done for every voxel separately. A data point is the value of a voxel at a given time. Typically, we have a lot more data points than fit parameters. Therefore we are dealing with a overdetermined system. The standard technique to find the best fit is to use *singular value decomposition* (SVD).

Suppose we have an $m \times n$ matrix $\boldsymbol{A}$ of rank n and a column vector $\boldsymbol{y}$ of length m with $m \geq n$. Then the linear equation $\boldsymbol{Ax}{=}\boldsymbol{y}$ is overdetermined and has no solution in general. However, instead of an exact solution, we can look for a vector $\boldsymbol{x}$ that is “closest” to a a solution. To be precise, we are looking for a vector $\boldsymbol{x}$ such that the 2-norm $||\boldsymbol{Ax} - \boldsymbol{y}||^2$

---

[1] A *voxel* is a volumetric pixel, the building block of the tomographic image.

becomes minimal. The matrix $\boldsymbol{A}^{+}$ that yields a vector $\boldsymbol{x} = \boldsymbol{A}^{+}\boldsymbol{y}$ which minimizes the 2-norm $||\boldsymbol{A}\boldsymbol{x} - \boldsymbol{y}||^2$ is called the Moore-Penrose matrix pseudo-inverse of $\boldsymbol{A}$ [77]. It can be expressed as

$$\boldsymbol{A}^{+} = \left(\boldsymbol{A}^T\boldsymbol{A}\right)^{-1}\boldsymbol{A}^T \tag{8.1}$$

Note that if $\boldsymbol{A}$was invertible in the first place, the inverse and the pseudo-inverse are identical.

A sketch of the proof follows:

$$\begin{gathered}
\text{We want to minimize the norm } d = ||\boldsymbol{A}\boldsymbol{x} - \boldsymbol{y}||^2 \\
\text{This is a quadratic expression, that vanishes if its gradient} \\
\operatorname{grad} d = \left(\frac{\mathrm{d}\,d}{\mathrm{d}\,x_1}, \ldots, \frac{\mathrm{d}\,d}{\mathrm{d}\,x_n}\right) \quad \text{vanishes.} \\
\text{Using} \quad d = \boldsymbol{x}^T\boldsymbol{A}^T\boldsymbol{A}\boldsymbol{x} + \boldsymbol{y}^T\boldsymbol{y} - 2\boldsymbol{y}^T\boldsymbol{A}\boldsymbol{x} \\
\text{we obtain} \quad \operatorname{grad} d = 2\boldsymbol{x}^T\boldsymbol{A}^T\boldsymbol{A} - 2\boldsymbol{y}^T\boldsymbol{A}^T \\
\text{therefore,} \quad \boldsymbol{A}^T\boldsymbol{y} = \boldsymbol{A}^T\boldsymbol{A}\boldsymbol{x} \quad \text{if } d \text{ is minimal.} \\
\text{if} \quad \boldsymbol{A}^T\boldsymbol{A} \quad \text{is invertible,} \quad \boldsymbol{x} = \left(\boldsymbol{A}^T\boldsymbol{A}\right)^{-1}\boldsymbol{A}^T\boldsymbol{y} =: \boldsymbol{A}^{+}\boldsymbol{y}
\end{gathered}$$

Note that we assumed that the matrix $\boldsymbol{A}$ has a rank of n.

A convenient method to compute the Moore-Penrose matrix inverse is the *singular value decomposition.* Any $m \times n$ matrix can be written as

$$\boldsymbol{A} = \boldsymbol{U}\boldsymbol{S}\boldsymbol{V}^T \tag{8.2}$$

where $\boldsymbol{U}$ is $m \times m$ matrix $\boldsymbol{S}$ is a diagonal $n \times n$ matrix and $\boldsymbol{V}$ is an $n \times n$ matrix. The matrix elements of $\boldsymbol{S}$ are positive or zero, $\boldsymbol{U}$ and $\boldsymbol{V}$ are orthogonal. Here, an orthogonal matrix is a matrix whose column vectors form a set of orthonormal vectors. If all diagonal values $s_1, \ldots, s_n$of $\boldsymbol{S}$ are positive, it is straightforward to show that

$$\boldsymbol{A}^{+} = \boldsymbol{V}\boldsymbol{S}^{-1}\boldsymbol{U}^T \tag{8.3}$$

Just apply Eq. (8.1) to Eq. (8.2):

$$\begin{aligned}
\left(\boldsymbol{A}^T\boldsymbol{A}\right)^{-1}\boldsymbol{A}^T &= \left(\boldsymbol{V}\boldsymbol{S}\boldsymbol{U}^T\boldsymbol{U}\boldsymbol{S}\boldsymbol{V}^T\right)^{-1}\boldsymbol{V}\boldsymbol{S}\boldsymbol{U}^T = \left(\boldsymbol{V}\boldsymbol{S}^2\boldsymbol{V}^T\right)^{-1}\boldsymbol{V}\boldsymbol{S}\boldsymbol{U}^T \\
&= \boldsymbol{V}\boldsymbol{S}^{-2}\boldsymbol{V}^T\boldsymbol{V}\boldsymbol{S}\boldsymbol{U}^T = \boldsymbol{V}\boldsymbol{S}^{-1}\boldsymbol{U}^T
\end{aligned}$$

The real advantage of using singular value decomposition to compute the Moore-Penrose pseudo-inverse is, that we can cope with ill-conditioned systems. In such a system, one or more of the diagonal values of $\boldsymbol{S}$, $s_1, \ldots, s_n$ is zero or close to zero. This means that the rank of $\boldsymbol{A}$ is less than n. In this case, $\boldsymbol{S}^{-1}$ is ill-defined. In this case, we define the pseudo-inverse of $\boldsymbol{S}$ such that the troublesome inverse eigenvalue of $\boldsymbol{S}$ is set to zero, i.e.,

$$\boldsymbol{A}^{+} = \boldsymbol{V}\boldsymbol{S}^{+}\boldsymbol{U}^T \tag{8.4}$$

$$\text{with} \quad \boldsymbol{S}^{+} = \operatorname{diag}\left(\frac{1}{s_1}, \ldots\, 0, \ldots\, \frac{1}{s_n}\right) \tag{8.5}$$

Details on how to perform the singular value decomposition itself can be found in [78, 79]. Implementations of the numerical algorithm for SVD can be found in various popular libraries, for example in in the GNU scientific library [80] or in the LAPACK library [81].

8.3 The design matrix

I will now show how the multi-parameter fit procedure from the previous section can be put to use for fMRI. The vector $\boldsymbol{y}$ are now our measured data. One vector element corresponds to one timestep. Keep in mind that we are doing the multi parameter fit separately for every voxel, so there is a different vector $\boldsymbol{y}$ for every voxel. The vector $\boldsymbol{x}$ are the fit parameters. We can see now that the typical setup is such that there are much more datapoints in time than fit parameters – a typical fMRI session might last more than five minutes with a new volumetric image every two seconds, and the number of fit parameters is well under 10. The matrix $\boldsymbol{A}$ contains the model were we want to fit the data to. $\boldsymbol{A}$ is usually called the *design matrix*. One might think that the columns of the design matrix just consist of zeros and ones if we are using a simple block design. However, experience shows that the organic response to a stimulus is also block-shaped is generally not true. Therefore, the design matrix has to be constructed in a slightly more sophisticated way.

8.3.1 The haemodynamic response function and the BOLD signal

For fMRI, the most widely used signal is the *blood oxygen level dependent* (BOLD) signal. This method was introduced by S. Ogawa [82]. It uses the fact that haemoglobin changes its magnetic properties depending if it is oxygenized or not. This change in the magnetic behavior can be detected through MRI if appropriate pulse sequences are employed. The paradigm that a higher consumption of oxygen is spatially correlated with an enhanced brain activity is widely accepted. The variation of the blood oxygen level after a stimulus is called the haemodynamic response. This response, however, is not immediate and non-linear. The model for the response is the so-called *haemodynamic response function* (HRF). Various model exist, see for example [83, 84].

I chose to use the same HRF as the one used by the popular software package *SPM* [85, 86, 87], a package widely used for fMRI analyses. The HRF and its derivatives are

$$h_R(t) = \frac{1}{1-\gamma}\left(\frac{t^{\alpha-1}e^{-t}}{\Gamma(\alpha)} - \gamma\frac{t^{\beta-1}e^{-t}}{\Gamma(\beta)}\right) \tag{8.6}$$

$$\frac{\mathrm{d}}{\mathrm{d}\,t}h_R(t) = \frac{e^{-t}}{1-\gamma}\left(\frac{t^{\alpha-2}}{\Gamma(\alpha-1)} - \frac{t^{\alpha-1}}{\Gamma(\alpha)} - \gamma\frac{t^{\beta-2}}{\Gamma(\beta-1)} + \gamma\frac{t^{\beta-1}}{\Gamma(\beta)}\right) \tag{8.7}$$

$$\frac{\mathrm{d}^2}{\mathrm{d}\,t^2}h_R(t) = \frac{e^{-t}}{1-\gamma}\left(\frac{t^{\alpha-3}}{\Gamma(\alpha-2)} - 2\frac{t^{\alpha-2}}{\Gamma(\alpha-1)} + \frac{t^{\alpha-1}}{\Gamma(\alpha)} - \gamma\frac{t^{\beta-3}}{\Gamma(\beta-2)} + 2\gamma\frac{t^{\beta-2}}{\Gamma(\beta-1)} - \gamma\frac{t^{\beta-1}}{\Gamma(\beta)}\right) \tag{8.8}$$

where t is the time in seconds, $\alpha = \frac{p_1}{p_3}$, $\beta = \frac{p_2}{p_4}$, $\gamma = \frac{1}{p_5}$, and $p_1 = 6$ $p_2 = 16$ $p_3 = 1$ $p_4 = 1$ $p_5 = 6$ and $\Gamma(x) = \int_0^\infty y^{x-1}e^{-y}\,\mathrm{d}\,y$ is the gamma function. Figure 8.1 shows the HRF and its derivatives.

8.3.2 Design matrix for a simple block design

Even if our simple block design has just one stimulus, our design matrix has at least four columns:

- a constant column to allow for a constant background,
- a drift column to allow for a continuous increase or decrease of the brain activity during the experiment
- a column that is the convolution of the HRF with the block design, and

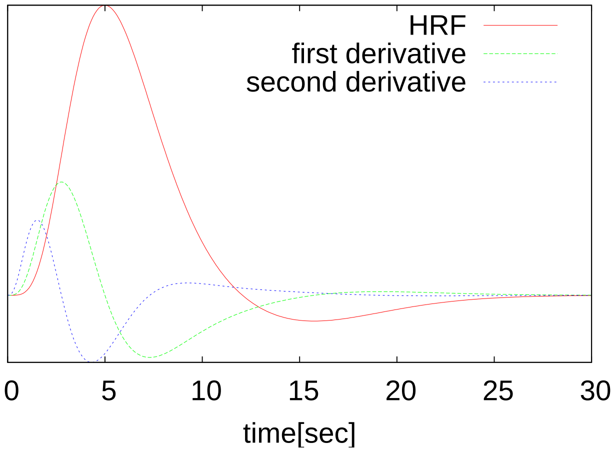

Figure 8.1: This figure shows the haemodynamic response function (HRF) and its derivatives as in Eq. (8.6), Eq. (8.7), Eq. (8.8).

- a column that is the convolution of the inverse of the block design, since we do not know if the brain activity is correlated or anti-correlated with the stimulus.

One can include convolutions of the first and second derivatives of the HRF with the block design. The basic idea behind is simply the usual Taylor expansion:

$$f(x+\epsilon) = f(x) + f'(x)\epsilon + \frac{1}{2}f''(x)\epsilon^2 \tag{8.9}$$

This means that if we include the derivatives in the design matrix, we allow in a way for a non-standard HRF, i.e., a HRF that sets in a little earlier or later that the standard one, or a HRF that is a bit narrower or wider. Figure 8.2 shows how the design matrix could look like.

8.3.3 T-values and contrast

There is one more step to do. We have to define a quantity that reflects the quality of the multi-parameter fit. Moreover, we want to have the freedom to test for various relationships between the fit parameters. The tool for this is the contrast vector c which has the same number of elements there are fit parameters. Using the contrast, we define the *T-value* as

$$T = \frac{\boldsymbol{c}^T \boldsymbol{x}}{\sqrt{\sigma^2 \, \boldsymbol{c}^T \left(\boldsymbol{A}^T \boldsymbol{A}\right)^+ \boldsymbol{c}}} \quad \text{with} \quad \sigma^2 = ||\boldsymbol{A}\boldsymbol{x} - \boldsymbol{y}||^2 \tag{8.10}$$

Again, $\boldsymbol{A}$ is the design matrix, $\boldsymbol{x}$ is the set of parameters that minimizes the 2-norm and $\boldsymbol{y}$ is the measured data. Larger values of T indicate a better fit.

8.4 Implementation on the QCDOC

The link between psychology and QCD is the implementation of the SVD algorithm and the computation of the T-values on the QCDOC. The QCDOC is a massively parallel machine, specially designed to run QCD simulations [88, 89, 90]. Since the calculation of the T-values can be done for each voxel separately, a given fMRI image can be distributed

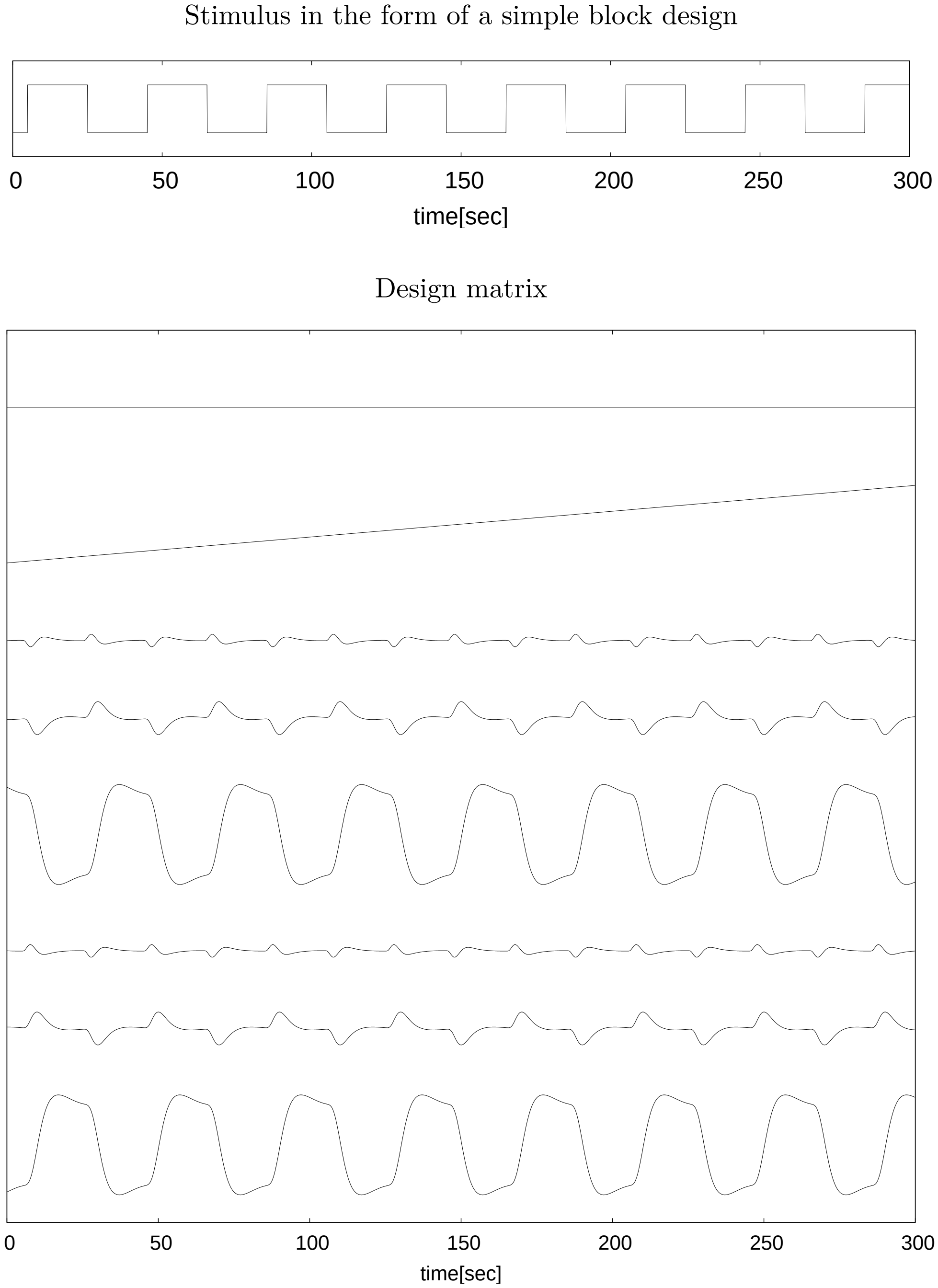

Figure 8.2: This figure shows an example of a block design stimulus and a design matrix. The picture at the top shows the stimulus. Every 20 seconds, the test person sees a moving pattern (when the curve is high). The lower graph shows the design matrix. Every curve represents a column in the design matrix. The curves are – from top to bottom: the constant column, the drift column, second derivative of the HRF convoluted with inverse stimulus, first derivative of the HRF convoluted with inverse stimulus, HRF convoluted with inverse stimulus, second derivative of the HRF convoluted with stimulus, first derivative of the HRF convoluted with stimulus, HRF convoluted with stimulus.

among many compute nodes within the QCDOC. Nevertheless, some communication between nodes was necessary for synchronizing the different tasks. An MPI implementation for the QCD was extremely helpful [91].

The basis setup is shown in Figure 8.3. From the MRI scanner – which is located in the Bezirksklinikum Regensburg – the data is transferred to a local PC next to the scanner. The local PC then copies the data using the popular secure copy tool `scp` to the frontend PC in the physics department. The frontend PC runs an NFS server and presents the data to the parallel application running on the QCDOC. The parallel application then fetches the data, computes the T-values and writes the output to the frontend PC.

The primary computational workload is the multi-parameter fit described in the previous section. The merging and generation of control files can easily be done via simple shell scripts. It turned out that I could reduce the noise in the data if I realigned and smoothed the data coming from the local PC. Realignment would correct if the test person moved in between the fMRI images. A convenient external tool for smoothing and realignment is the *AIR* software [92, 93]. No modifications to *AIR* were necessary. It ran fast enough as a single task on the frontend PC. The workflow of the parallel application is controlled via lock files on the frontend PC. This might seem clumsy, but there is no other way to communicate with a running application on the QCDOC, besides hacking the kernel.

Figure 8.4 shows a detailed flowchart of the setup. First, the MRI scanner transfers the fMRI images to the local PC via Ethernet. The local PC `dcmtk`, a piece of software able to receive DICOM images. On the local PC, the images are converted to the Analyze (ANLZ) format using `medcon`. The local PC then copies the ANLZ file to the frontend PC. On the frontend PC, the generation script polls if new data has arrived. If so, the generation script calls the *AIR* tool in order to smooth and realign the new data. After that, the generation script writes a configuration file. If the configuration file has been written, the generation script deletes a lock file. The parallel application that performs the multi-parameter fit polls the lock file. If the lock file is gone, the parallel application reads the new data, the configuration file, the design matrix and the contrast vector. The computation of the T-maps is then done in parallel. Every process writes its T-map separately to the frontend. One all processes have finished writing the output data, the parallel application writes a “done” file to the frontend PC. On the frontend, the assemble script polls the presence of the “done” file. If it is there, the assemble script produces a file containing the full T-map from the output files. Then the viewer application can be used to visualize the process. In fact, the viewer application polls a new T-map file has been produced and so the viewer can auto-update the T-map on the display.

All communication from the frontend PC to the parallel application words through configuration files and lock files, and all file operations are performed via NFS. The tasks running on the frontend PC run very fast - no parallelization on the frontend PC is necessary. As an example, Figure 8.5 shows the generation script and Figure 8.6 lists the code of the assemble script. Figure 8.7 shows the QCDOC setup in Regensburg. I want to emphasize that this setup is very flexible, since the design matrix and the contrast vector can be changed during the measurement. Both the design matrix and the contrast vector are simple ASCII files that are provided by the user.

8.5 A test case

In the test case, we ran a full fMRI session with a test person. The experimental design was the same as described before: the test person located in the MRI scanner saw a pattern of moving dots for 20 seconds, then the pattern remained motionless for 20 seconds, then started moving again for 20 seconds, and so on. The test person was not required to perform a specific action. The design matrix was the design matrix for a simple block design, but columns that consisted of the convolution of the block design with derivatives tp!

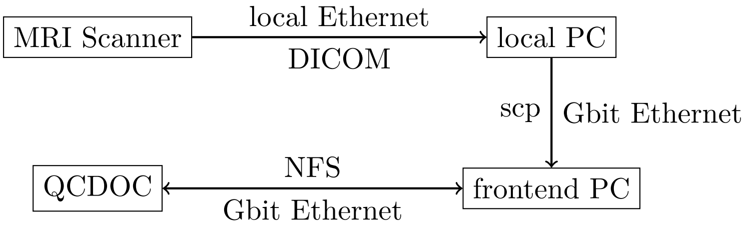

Figure 8.3: This chart shows the basic setup for parallel analysis of fMRI data. The transport layer of all data is Ethernet or Gbit Ethernet. From the MRI scanner, DICOM data is transported to a local PC. The data is then copied using `scp` to the frontend PC. The QCDOC then uses NFS to transport data from and to the frontend PC.

of the haemodynamic response function were excluded. Figure 8.8 shows how the columns of the design matrix looked like. As a reminder, the parallel application used singular value decomposition to find the best solution to $\boldsymbol{A\beta} = \boldsymbol{y}$, where $\boldsymbol{A}$ is the design matrix, $\boldsymbol{\beta}$ are the parameters we are trying to fit, and $\boldsymbol{y}$ is the measured data. There are four parameters, one for each column of the design matrix. Figure 8.9 shows the equation. The T-value then was computed as

$$T = \frac{\boldsymbol{c}^T \boldsymbol{\beta}}{\sqrt{\sigma^2\, \boldsymbol{c}^T \left(\boldsymbol{A}^T \boldsymbol{A}\right)^+ \boldsymbol{c}}} \quad \text{with} \quad \sigma^2 = \left|\left|\boldsymbol{A\beta} - \boldsymbol{y}\right|\right|^2 \quad \text{and} \quad \boldsymbol{c}^T = (1,\, -1,\, 0,\, 0) \tag{8.11}$$

The contrast vector excludes the fit to the constant column and the drift column from the computation of the T-value. This is natural, since we assume that a constant background of a global drift during the experiment is background noise or a systematic error. The contrast 1 in the third column and −1 in the fourth column says, that we measure a T-value for brain activities that is correlated with the stimulus and anti-correlated with the inverse of the stimulus.

During the measurement, the viewer application polls the produced T-maps and updates the display automatically. Moreover, it can be used in a way that the cutoff in the T-value is chosen automatically such that a certain percentage of the brain is highlighted. Figure 8.12 shows a screenshot of the viewer application for two different cutoffs. The background image of the brain can be chosen via a convenient standard dialog, and the combined picture – background image and T-map – can be saved to a file. See Figure 8.13.

Figure 8.10 shows the T-map evaluated after the experiment which lasted 800 seconds. I produced the image with the same viewer application that is also used during the experiment. For comparison, Figure 8.11 shows an analysis of the same data with the SPM tool. Both images are reasonably similar. The different scale of the two T-maps comes from the fact that SPM performs a very sophisticated post-processing of the data. This post-processing takes some time, of course. In contrast to that, the implementation of fMRI analysis on the QCDOC had a delay between measurement and generation of the T-map of roughly three seconds. While this is not quite a real-time application, it is pretty close.

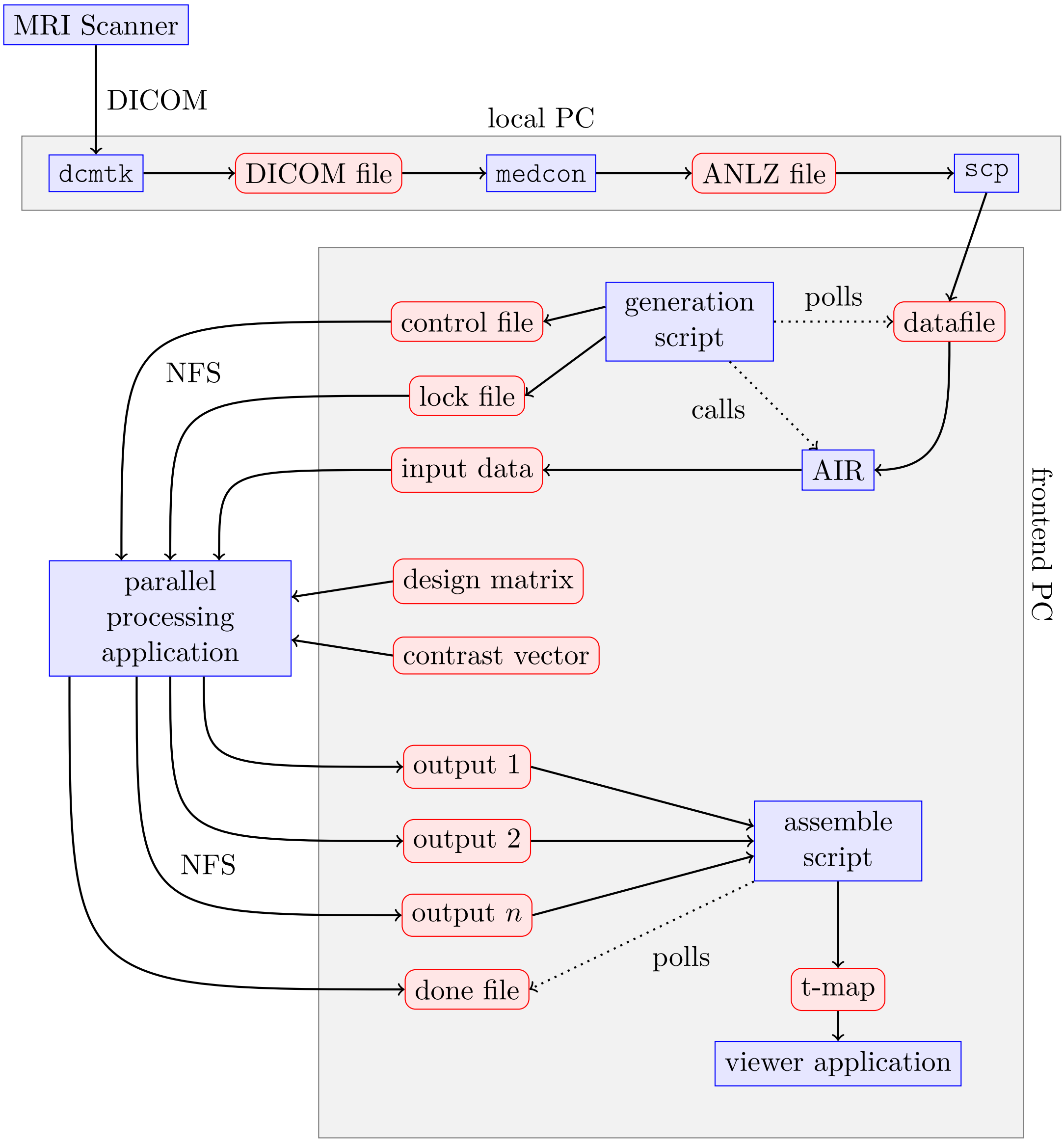

Figure 8.4: This flowchart shows the flow of information during a parallel analysis session of fMRI data. The DICOM data generated by the MRI scanner is transferred to a local PC using the `dcmtk` software. It is then converted to `anlz` format by `medcon` and copied to the frontend PC using `scp`. On the frontend, a script polls if new data has arrived and writes an control file. The script also calls the *AIR* program to realign and smooth the data. If the preprocessing is finished, the generation script clears the lock file. The parallel processing application starts a new run as soon as the lock file is removed and reads the data file and the input file via NFS. Every parallel process then writes a separate output file via NFS to the frontend PC. The "done" file signals that all output files have been written. There, the assemble script combines all output files into a file containing the t-map. A viewer application polls file containing the t-map for updates.

```
#!/bin/bash

first=$( basename $( ls MR*.img | head -n 1 ) .img )

runner=0
while true
do
    sleep 1

    for name in MR_*.img;
    do
  if test -e gs_ral_${name}
then continue
fi

if test -r ${name} -a -r $( basename ${name} .img ).hdr
then

            base=$( basename ${name} .img )
            rm -f air_out
            /host/sos28559/AIR/AIR5.2.5/alignlinear ${first}              ${base}  air_out -m 6
            /host/sos28559/AIR/AIR5.2.5/reslice      air_out          ral_${base}
            /host/sos28559/AIR/AIR5.2.5/gsmooth  ral_${base} 5 5 5 gs_ral_${base} -r
fi
    done

    touch svd-lock
    runner=$(( ${runner} + 1 ))
    xtensi=‘printf "%05d" ${runner}‘
cat << EOF > svd-input
svd-output-${xtensi}
64
64
64
32
300
1
0
EOF

#ls gigabit/m???-*.bin >>  svd-input
ls gs_ral_*.img >> svd-input

rm -f svd-lock

done
```

Figure 8.5: Code listing of the script generating the input files for the parallel processing application. The external tool *AIR* is used to align and smooth the fMRI data.

```
#!/bin/bash

while true;
do
    for name in svd-output-?????-written;
    do
        basen=‘basename ${name} "-written"‘;
        if [ ! -e "${basen}-all.dat" ];
        then
            cat ${basen}-????? >> "${basen}-all.dat";
        fi
    done
    sleep 1;
done
```

Figure 8.6: Code listing of the script assembling the output files. A simple concatenation is enough.

Figure 8.7: The top picture shows the QCDOC located in Regensburg. The fMRI analysis used one half on the machine at once. The bottom picture shows a single QCDOC node. One can see the two chips per node and the main memory located on the upper side of the node.

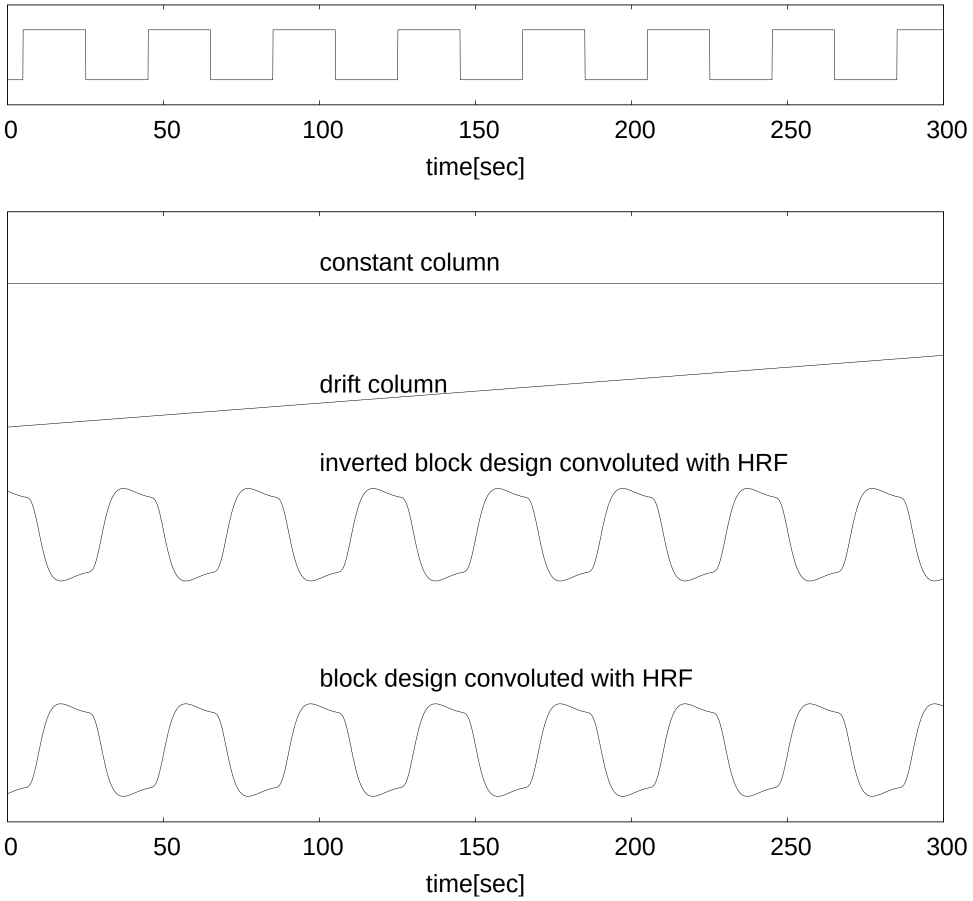

Figure 8.8: This figure shows the design matrix I used for the test case. It contains four columns: a constant column, a drift column, the convolution of the block design with the HRF and the convolution of the inverse block design with the HRF.

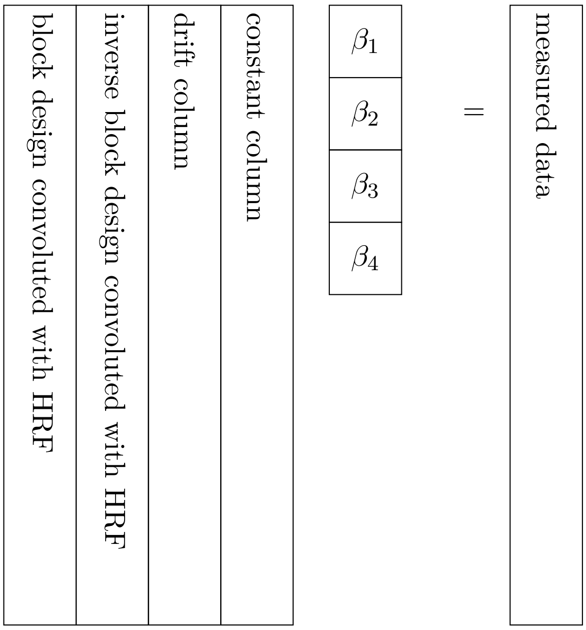

Figure 8.9: This figure shows the multi parameter fitting routine schematically. Typically, the design matrix, which consists of four columns in our test case, has much more rows than columns. The vector $\boldsymbol{\beta}$ is determined such that its components β_1 through β_4 provide the best possible fit of the model to the measured data $\boldsymbol{y}$. Since the system of linear equation is usually overdetermined, the above equation cannot be fulfilled exactly. However, the “solution” is the vector $\boldsymbol{\beta}$ that minimizes the 2-norm $||\boldsymbol{A\beta} - \boldsymbol{y}||^2$.

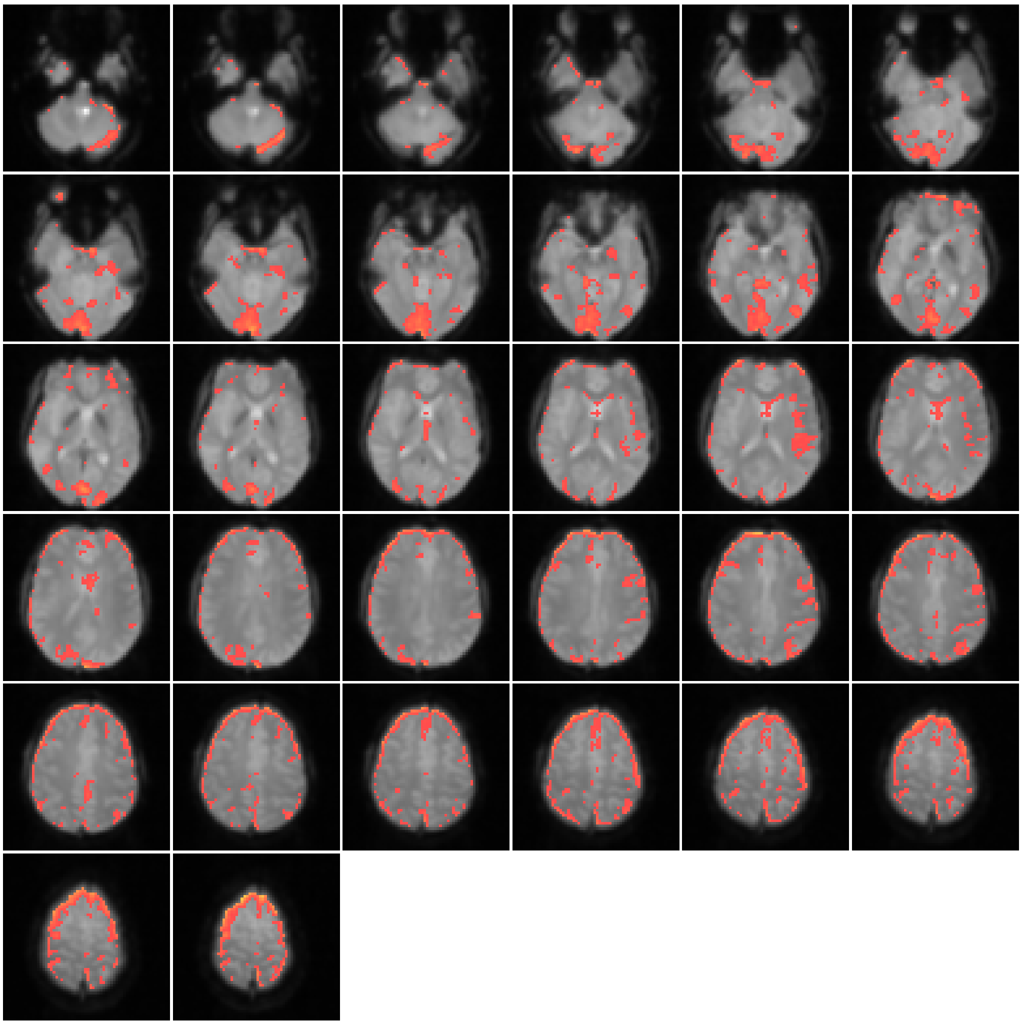

Figure 8.10: This figure shows an example of an fMRI measurement. The colored areas are those areas where the T-value is higher than a certain cutoff, in this case 3.35. The T-map is blended over a regular fMRI image of the brain. This picture has been produced with the viewer application.

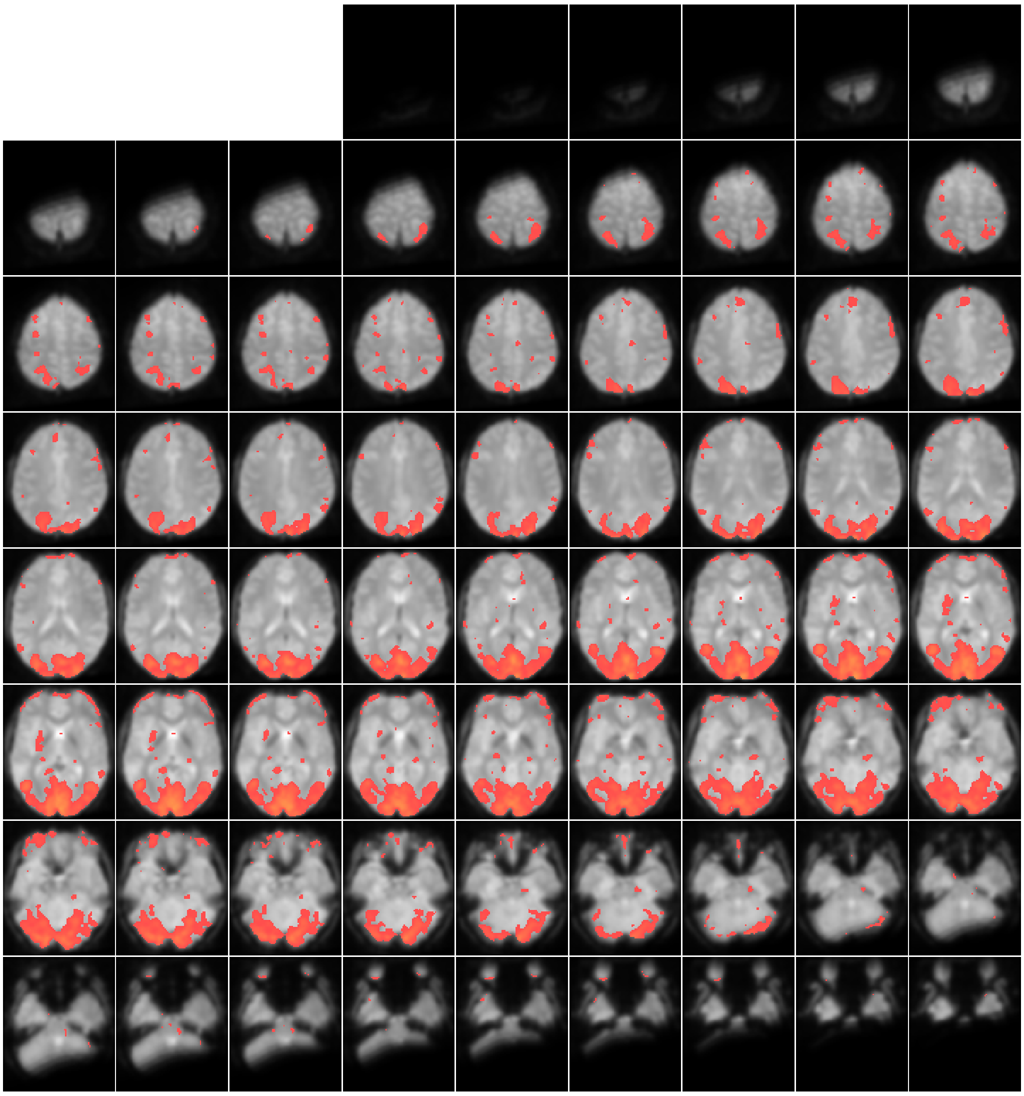

Figure 8.11: This figure shows an analysis of the test case with the SPM software. It is based on the same raw data as Figure 8.10. The resolution is different since SPM performs some quite sophisticated post-processing steps.

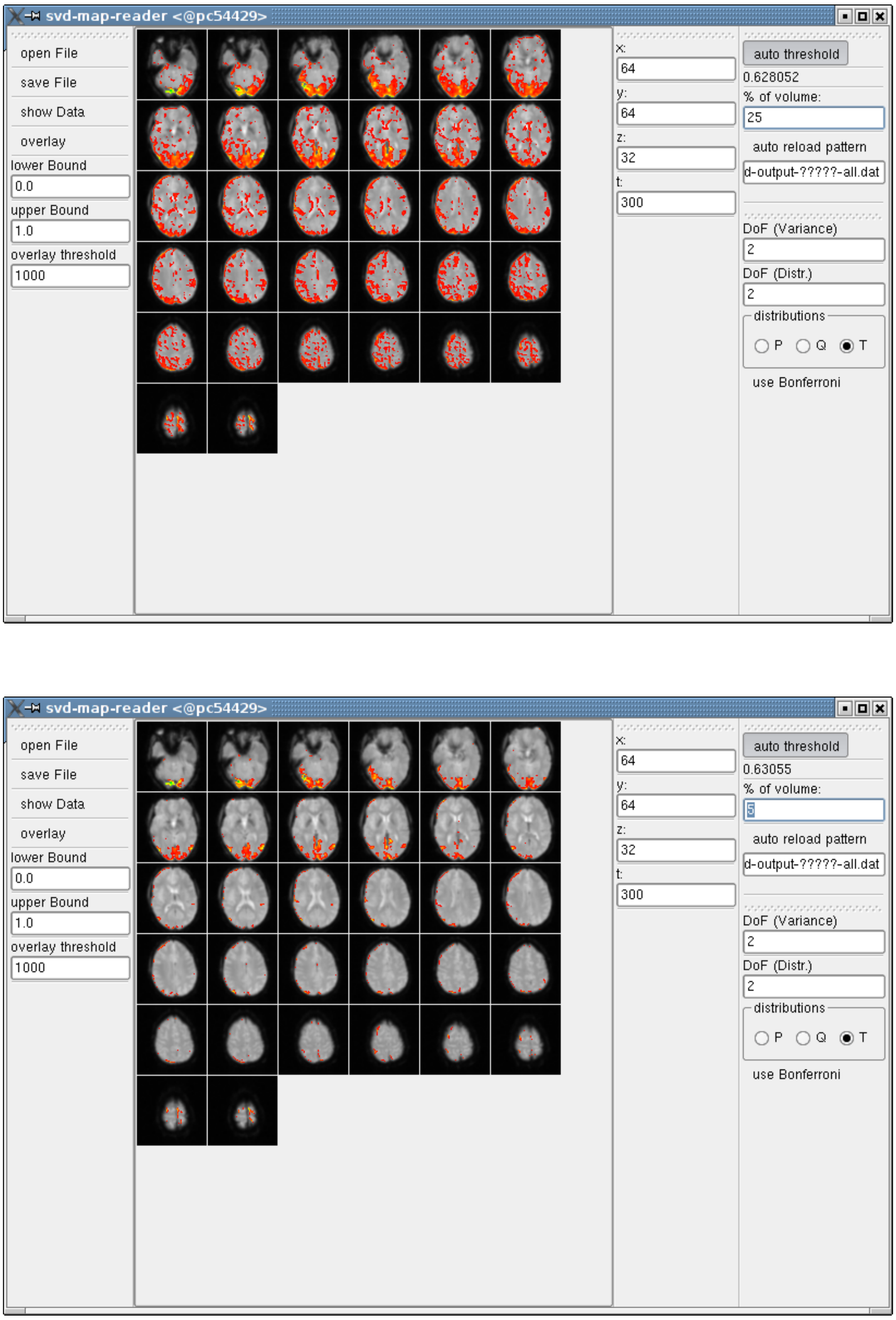

lower Bound: 0.0
upper Bound: 1.0
overlay threshold: 1000
x: 64
y: 64
z: 32
t: 300
0.628052
% of volume: 25
d-output-?????-all.dat
DoF (Variance): 2
DoF (Distr.): 2
○ P ○ Q ● T

lower Bound: 0.0
upper Bound: 1.0
overlay threshold: 1000
x: 64
y: 64
z: 32
t: 300
0.63055
% of volume: 5
d-output-?????-all.dat
DoF (Variance): 2
DoF (Distr.): 2
○ P ○ Q ● T

Figure 8.12: This figure shows two screenshots of the viewer application. In top image the cutoff in the T-values is chosen such that 25% of the brain volume are highlighted, in the bottom image only 5% of the brain volume are highlighted.

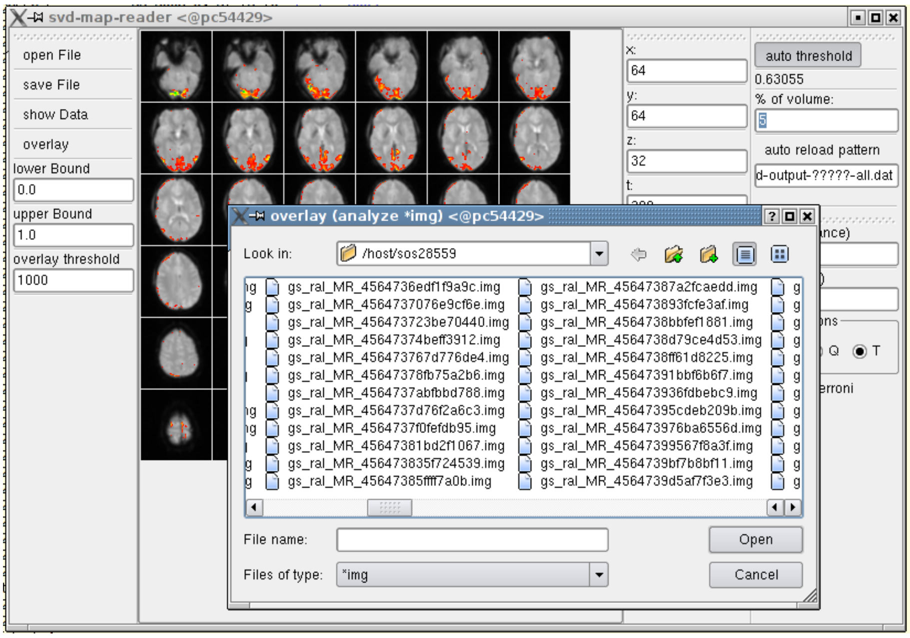

lower Bound: 0.0
upper Bound: 1.0
overlay threshold: 1000
x: 64
y: 64
z: 32
0.63055
% of volume: 5
d-output-?????-all.dat

Look in: /host/sos28559

gs_ral_MR_4564736edf1f9a9c.img
gs_ral_MR_4564737076e9cf6e.img
gs_ral_MR_456473723be70440.img
gs_ral_MR_4564737 4beff3912.img
gs_ral_MR_456473767d776de4.img
gs_ral_MR_4564737 8fb75a2b6.img
gs_ral_MR_4564737abfbbd788.img
gs_ral_MR_4564737d76f2a6c3.img
gs_ral_MR_4564737f0fefdb95.img
gs_ral_MR_45647381bd2f1067.img
gs_ral_MR_456473835f724539.img
gs_ral_MR_45647385ffff7a0b.img
gs_ral_MR_45647387a2fcaedd.img
gs_ral_MR_456473893fcfe3af.img
gs_ral_MR_4564738bbfef1881.img
gs_ral_MR_4564738d79ce4d53.img
gs_ral_MR_4564738ff61d8225.img
gs_ral_MR_45647391bbf6b6f7.img
gs_ral_MR_456473936fdbebc9.img
gs_ral_MR_45647395cdeb209b.img
gs_ral_MR_456473976ba6556d.img
gs_ral_MR_45647399567f8a3f.img
gs_ral_MR_4564739bf7b8bf11.img
gs_ral_MR_4564739d5af7f3e3.img

File name:
Files of type: *img

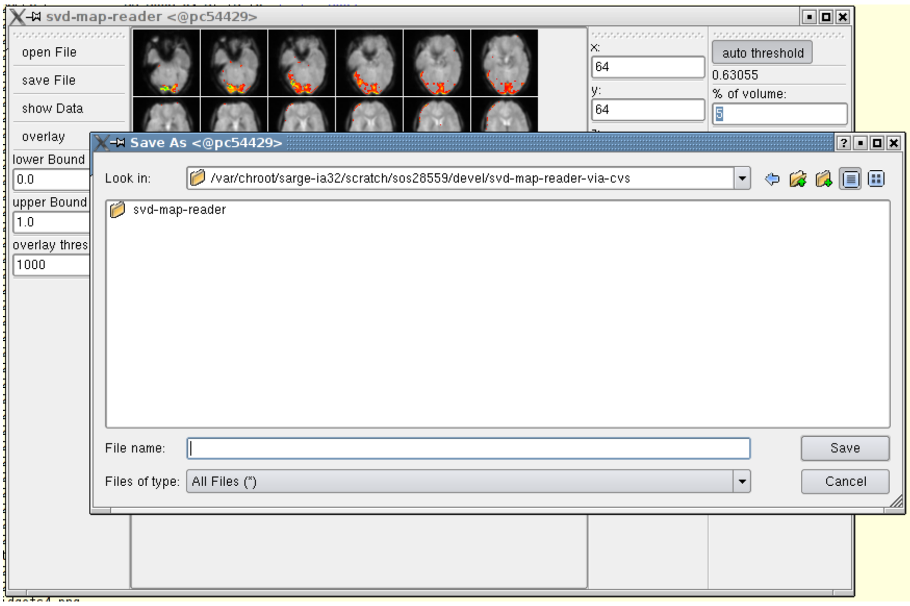

lower Bound: 0.0
upper Bound: 1.0
overlay thres: 1000
x: 64
y: 64
0.63055
% of volume: 5

Look in: /var/chroot/sarge-ia32/scratch/sos28559/devel/svd-map-reader-via-cvs

svd-map-reader

File name:
Files of type: All Files (*)

Figure 8.13: This figure shows screenshots of the standard file dialogs of the viewer application. The top image shows the dialog to select the background image, the bottom image shows how the current T-map can be saved to a file.

Chapter 9

Summary and Prospects

Topology on the lattice is a wide field. A thorough understanding is not yet reached, yet many results have been found and promising projects are underway. I hope that the work of this thesis will be useful for further developments.

The method of combined filtering provides a systematic approach to evaluate topological structures. Filtering based on smoothing techniques like cooling and various smearing algorithms had the notion of "reading the tea leaves." However, since three completely unrelated filtering methods, namely Dirac eigenmodes, Laplacian eigenmodes and APE smearing yield compatible results, I am convinced that filtering is a well grounded technique. The results obtained from filtered configurations indeed provide deeper insight into the topological structures of the gauge fields.

Based on the trusted results from filtering, I determined the cluster size distribution for thermalized quenched $SU(2)$ lattice gauge fields. For small watermarks – corresponding to a large threshold – the cluster distribution obeys a power law. Its exponent is significantly higher than the exponent expected for the dilute instanton gas. The dilute instanton gas can therefore be excluded as a model for the topological structures. While this does not come as a surprise, it is another important cross-check for the reliability of the filtering approach. Moreover, it means that filtering can be used to benchmark other models. A model that claims to explain the topological structures seen in thermalized configurations should reproduce the exponent of the power-law as found in this thesis. I would be exited to other members of the community to derive such exponents from various models analytically. Monopoles, calorons and vortices immediately come to my mind.

While the investigation of the $SU(2)$ model is vital for a thorough understanding of gauge field topology, the community should simultaneously investigate topology in other settings. Filtering works as well on $SU(3)$ configurations and today even unquenched $SU(3)$ configurations with good chiral properties are available. Filtering can be applied to those configurations as well, and the comparison with my results is surely interesting.

While the quest for a unified model for chiral symmetry breaking and confinement seems purely academic, other activities of the vibrant lattice QCD community can have immediate ramifications for the greater population. It is commonplace that lattice QCD calculations trigger an insatiable hunger for computing power and the development of ever faster and more scalable machines. I showed in one example – the QCDOC machine – that these machines can be used for other life sciences although they were once constructed as special-purpose machines. This prolific relationship of theoretical physics and other branches of science will not stop. New projects targeted at the development of the next generation of massively parallel computers are already underway.

I dare to make a bold prediction of the future of lattice QCD. Just as in collider physics, the machinery necessary for lattice QCD becomes more and more complex and expensive. A consolidation process seems inevitable. This applies both to the development and the maintenance of parallel computers in large computing centers as well as to software development. If lattice QCD wants to keep up with the pace of hardware development in collider physics or software development in solid state physics, then the community should focus on creating reusable open software libraries as well as reusable hardware designs. Tedious replication of common tasks might have a certain use in teaching but will not contribute to the overall scientific progress.

Bibliography

[1] T. Frankel, *The Geometry of Physics*, pp. 405,541,595. Cambridge University Press, 1997, ISBN 0-521-38753-1.

[2] H. R. Dullin, "Inflation of hamiltonian system: The spinning top in projective space," `chao-dyn/9604015`.

[3] M. A. Porter, "The hopf fibration and its applications," *Never published* (1999) URL: `http://www.its.caltech.edu/~mason/research/topology.ps`.

[4] T. Frankel, *The Geometry of Physics*, pp. 210–221. Cambridge University Press, 1997, ISBN 0-521-38753-1.

[5] T. Frankel, *The Geometry of Physics*, pp. 585,586. Cambridge University Press, 1997, ISBN 0-521-38753-1.

[6] M. E. Peskin and D. V. Schroeder, *An Introduction to quantum field theory*, pp. 659–676. In *The Advanced Book Program* [94], 1995. Reading, USA: Addison-Wesley (1995) 842 p.

[7] M. E. Peskin and D. V. Schroeder, *An Introduction to quantum field theory*, pp. 301–302. In *The Advanced Book Program* [94], 1995. Reading, USA: Addison-Wesley (1995) 842 p.

[8] S. Solbrig, "Chiral symmetry breaking and topological excitations in SU(2) Lattice Gauge Theory," diploma thesis, Univ. Regensburg, Universitätsstr. 31, 93053 Regensburg, 20xx04.

[9] K. Fujikawa, "A continuum limit of the chiral jacobian in lattice gauge theory," *Nucl. Phys.* **B546** (1999) 480–494, `hep-th/9811235`.

[10] R. A. Bertlmann, *Anomalies in quantum field theory.* The international series of monographs on physics, 91. Oxford University Press, 1996, ISBN 0-198-52047-6.

[11] M. F. Atiyah and I. M. Singer, "The index of elliptic operators. 5," *Annals Math.* **93** (1971) 139–149.

[12] K. G. Wilson, "CONFINEMENT OF QUARKS," *Phys. Rev.* **D10** (1974) 2445–2459, `doi: 10.1103/PhysRevD.10.2445`, URL: `http://link.aps.org/abstract/PRD/v10/p2445`.

[13] H. B. Nielsen and M. Ninomiya, "No go theorem for regularizing chiral fermions," *Phys. Lett.* **B105** (1981) 219.

[14] P. H. Ginsparg and K. G. Wilson, "A remnant of chiral symmetry on the lattice," *Phys. Rev.* **D25** (1982) 2649, `doi: 10.1103/PhysRevD.25.2649`, URL: `http://link.aps.org/abstract/PRD/v25/p2649`.

[15] H. Neuberger, "Exactly massless quarks on the lattice," *Phys. Lett.* **B417** (1998) 141–144, `hep-lat/9707022`, `doi: 10.1016/S0370-2693(97)01368-3`.

[16] H. Neuberger, "More about exactly massless quarks on the lattice," *Phys. Lett.* **B427** (1998) 353–355, `hep-lat/9801031`, `doi: 10.1016/S0370-2693(98)00355-4`.

[17] R. Narayanan and H. Neuberger, “Chiral fermions on the lattice,” *Phys. Rev. Lett.* **71** (1993) 3251–3254, `hep-lat/9308011`, `doi: 10.1103/PhysRevLett.71.3251`, URL: `http://link.aps.org/abstract/PRL/v71/p3251`.

[18] R. Narayanan and H. Neuberger, “Infinitely many regulator fields for chiral fermions,” *Phys. Lett.* **B302** (1993) 62–69, `hep-lat/9212019`, `doi: 10.1016/0370-2693(93)90636-V`.

[19] R. Narayanan and H. Neuberger, “A construction of lattice chiral gauge theories,” *Nucl. Phys.* **B443** (1995) 305–385, `hep-th/9411108`, `doi: 10.1016/0550-3213(95)00111-5`.

[20] C. Gattringer and I. Hip, “New approximate solutions of the ginsparg-wilson equation: Tests in 2-d,” *Phys. Lett.* **B480** (2000) 112–118, `hep-lat/0002002`.

[21] C. Gattringer, “A new approach to Ginsparg-Wilson fermions,” *Phys. Rev.* **D63** (2001) 114501, `hep-lat/0003005`, `doi: 10.1103/PhysRevD.63.114501`, URL: `http://link.aps.org/abstract/PRD/v63/e114501`.

[22] C. Gattringer, I. Hip, and C. B. Lang, “Approximate Ginsparg-Wilson fermions: A first test,” *Nucl. Phys.* **B597** (2001) 451–474, `hep-lat/0007042`.

[23] N. Metropolis, A. W. Rosenbluth, M. N. Rosenbluth, A. H. Teller, and E. Teller, “Equations of state calculations by fast computing machine,” *J. Chem. Phys.* **21** (1953) 1087–1091.

[24] N. Metropolis *et al.*, “Monte carlo calculations on intranuclear cascades. 2. high-energy studies and pion processes,” *Phys. Rev.* **110** (1958) 204–219.

[25] M. Lüscher and P. Weisz, “On-shell improved lattice gauge theories,” *Commun. Math. Phys.* **97** (1985) 59.

[26] M. Lüscher and P. Weisz, “Computation of the action for on-shell improved lattice gauge theories at weak coupling,” *Phys. Lett.* **B158** (1985) 250.

[27] Y. Aoki, G. Endrodi, Z. Fodor, S. D. Katz, and K. K. Szabo, “The order of the quantum chromodynamics transition predicted by the standard model of particle physics,” *Nature* **443** (2006) 675–678, `arXiv:hep-lat/0611014`, `doi: 10.1038/nature05120`.

[28] Z. Fodor, “QCD Thermodynamics,” *PoS* (2007) `arXiv:0711.0336 [hep-lat]`. PoS(LATTICE 2007)011.

[29] G. S. Bali, “Qcd forces and heavy quark bound states,” *Phys. Rept.* **343** (2001) 1–136, `hep-ph/0001312`.

[30] **APE** Collaboration, M. Albanese *et al.*, “Glueball masses and string tension in lattice qcd,” *Phys. Lett.* **B192** (1987) 163, `doi: 10.1016/0370-2693(87)91160-9`.

[31] M. Teper, “An improved method for lattice glueball calculations,” *Phys. Lett.* **B183** (1987) 345, `doi: 10.1016/0370-2693(87)90976-2`.

[32] S. O. Bilson-Thompson, D. B. Leinweber, and A. G. Williams, “Highly-improved lattice field-strength tensor,” *Ann. Phys.* **304** (2003) 1–21, `hep-lat/0203008`, `doi: 10.1016/S0003-4916(03)00009-5`.

[33] F. Niedermayer, “Exact chiral symmetry, topological charge and related topics,” *Nucl. Phys. Proc. Suppl.* **73** (1999) 105–119, `hep-lat/9810026`.

[34] M. Luscher, “Topology of lattice gauge fields,” *Commun. Math. Phys.* **85** (1982) 39.

[35] T. A. DeGrand, A. Hasenfratz, and T. G. Kovacs, “Revealing topological structure in the su(2) vacuum,” *Nucl. Phys.* **B520** (1998) 301–322, `hep-lat/9711032`.

[36] F. Bruckmann and E.-M. Ilgenfritz, “Laplacian modes probing gauge fields,” *Phys. Rev.* **D72** (2005) 114502, `hep-lat/0509020`.

[37] G. Münster and C. Kamp, “Distribution of instanton sizes in a simplified instanton gas model,” *Comput. Phys. Commun.* **147** (2002) 423–426, `doi: 10.1016/S0010-4655(02)00318-1`.

[38] G. ’t Hooft, “Computation of the quantum effects due to a four- dimensional pseudoparticle,” *Phys. Rev.* **D14** (1976) 3432–3450.

[39] P. Gerhold, E. M. Ilgenfritz, and M. Müller-Preussker, “An su(2) kvbll caloron gas model and confinement,” *Nucl. Phys.* **B760** (2007) 1–37, `hep-ph/0607315`, `doi: 10.1016/j.nuclphysb.2006.10.003`.

[40] E. M. Ilgenfritz, B. V. Martemyanov, M. Müller-Preussker, and A. I. Veselov, “Calorons and monopoles from smeared SU(2) lattice fields at non-zero temperature,” *Phys. Rev.* **D73** (2006) 094509, `hep-lat/0602002`, `doi: 10.1103/PhysRevD.73.094509`, URL: `http://link.aps.org/abstract/PRD/v73/e094509`.

[41] O. Miyamura, “Chiral symmetry breaking in gauge fields dominated by monopoles on su(2) lattices,” *Phys. Lett.* **B353** (1995) 91–95, `doi: 10.1016/0370-2693(95)00530-X`.

[42] S. Sasaki and O. Miyamura, “Existence of chiral-asymmetric zero modes in the background of qcd-monopoles,” *Nucl. Phys. Proc. Suppl.* **63** (1998) 507–509, `hep-lat/9709070`, `doi: 10.1016/S0920-5632(97)00816-5`.

[43] T. A. DeGrand and D. Toussaint, “Topological excitations and monte carlo simulation of abelian gauge theory,” *Phys. Rev.* **D22** (1980) 2478, `doi: 10.1103/PhysRevD.22.2478`, URL: `http://link.aps.org/abstract/PRD/v22/p2478`.

[44] M. I. G. Carrillo, *Modular Invariants for Manifolds with Boundary.* PhD thesis, Universitat Autònoma de Barcelona, 2001.

[45] K. Jänich, *Vektoranalysis.* Springer-Verlag, 2 ed., 1993, ISBN 3-540-57142-6.

[46] H. Reinhardt and M. Engelhardt, “Center vortices in continuum yang-mills theory,” `hep-th/0010031`.

[47] H. Reinhardt, “Topological charge of center vortices,” *Nucl. Phys. Proc. Suppl.* **119** (2003) 658–660, `arXiv:hep-th/0208116`, `doi: 10.1016/S0920-5632(03)01638-4`.

[48] H. Reinhardt, O. Schroeder, T. Tok, and V. C. Zhukovsky, “Quark zero modes in intersecting center vortex gauge fields,” *Phys. Rev.* **D66** (2002) 085004, `hep-th/0203012`, `doi: 10.1103/PhysRevD.66.085004`, URL: `http://link.aps.org/abstract/PRD/v66/e085004`.

[49] J. Gattnar *et al.*, “Center vortices and Dirac eigenmodes in SU(2) lattice gauge theory,” *Nucl. Phys.* **B716** (2005) 105–127, `hep-lat/0412032`, `doi: 10.1016/j.nuclphysb.2005.03.027`.

[50] L. Del Debbio, M. Faber, J. Greensite, and S. Olejnik, “Center dominance, center vortices, and confinement,” `hep-lat/9708023`.

[51] L. Del Debbio, M. Faber, J. Giedt, J. Greensite, and S. Olejnik, “Detection of center vortices in the lattice yang-mills vacuum,” *Phys. Rev.* **D58** (1998) 094501, `hep-lat/9801027`, `doi: 10.1103/PhysRevD.58.094501`, URL: `http://link.aps.org/abstract/PRD/v58/e094501`.

[52] K. Langfeld, “Confinement and the vortex vacuum of su(2) lattice gauge theory,” `hep-lat/9809003`.

[53] M. Engelhardt, “Center vortex model for the infrared sector of Yang-Mills theory: Quenched Dirac spectrum and chiral condensate,” *Nucl. Phys.* **B638** (2002) 81–110, `arXiv:hep-lat/0204002`, `doi: 10.1016/S0550-3213(02)00470-4`.

[54] M. Engelhardt, “Center vortex model for the infrared sector of Yang-Mills theory: Topological susceptibility,” *Nucl. Phys.* **B585** (2000) 614, `arXiv:hep-lat/0004013`, `doi: 10.1016/S0550-3213(00)00350-3`.

[55] M. Engelhardt, K. Langfeld, H. Reinhardt, and O. Tennert, “Deconfinement in su(2) yang-mills theory as a center vortex percolation transition,” *Phys. Rev.* **D61** (2000) 054504, `hep-lat/9904004`, `doi: 10.1103/PhysRevD.61.054504`, URL: `http://link.aps.org/abstract/PRD/v61/e054504`.

[56] P. de Forcrand and M. D’Elia, “On the relevance of center vortices to QCD,” *Phys. Rev. Lett.* **82** (1999) 4582–4585, `hep-lat/9901020`, `doi: 10.1103/PhysRevLett.82.4582`, URL: `http://link.aps.org/abstract/PRL/v82/p4582`.

[57] K. Langfeld, O. Tennert, M. Engelhardt, and H. Reinhardt, “Center vortices of yang-mills theory at finite temperatures,” *Phys. Lett.* **B452** (1999) 301, `hep-lat/9805002`, `doi: 10.1016/S0370-2693(99)00252-X`.

[58] M. Quandt, H. Reinhardt, and M. Engelhardt, “Center vortex model for SU(3) Yang-Mills theory,” *PoS* **LAT2005** (2006) 320, `arXiv:hep-lat/0509114`.

[59] T. Hashimoto *et al.*, “Magnetic configurations in SU(3) lattice near deconfining transition: charge and fermionic zero mode in cooling stage,” *Nucl. Phys. Proc. Suppl.* **17** (1990) 189–193, `doi: 10.1016/0920-5632(90)90235-M`.

[60] G. ’t Hooft, “Symmetry breaking through bell-jackiw anomalies,” *Phys. Rev. Lett.* **37** (1976) 8–11.

[61] A. A. Belavin, A. M. Polyakov, A. S. Shvarts, and Y. S. Tyupkin, “Pseudoparticle solutions of the yang-mills equations,” *Phys. Lett.* **B59** (1975) 85–87.

[62] T. Schäfer and E. V. Shuryak, “Instantons in qcd,” *Rev. Mod. Phys.* **70** (1998) 323–426, `hep-ph/9610451`, `doi: 10.1103/RevModPhys.70.323`, URL: `http://link.aps.org/abstract/RMP/v70/p323`.

[63] T. Banks and A. Casher, “Chiral symmetry breaking in confining theories,” *Nucl. Phys.* **B169** (1980) 103.

[64] T. DeGrand, A. Hasenfratz, and T. G. Kovacs, “Topological structure in the su(2) vacuum,” *Nucl. Phys. Proc. Suppl.* **63** (1998) 528–530, `hep-lat/9709095`.

[65] B. J. Harrington and H. K. Shepard, "Periodic Euclidean Solutions and the Finite Temperature Yang-Mills Gas," *Phys. Rev.* **D17** (1978) 2122, `doi: 10.1103/PhysRevD.17.2122`.

[66] T. C. Kraan and P. van Baal, "Periodic instantons with non-trivial holonomy," *Nucl. Phys.* **B533** (1998) 627–659, `hep-th/9805168`, `doi: 10.1016/S0550-3213(98)00590-2`.

[67] K.-M. Lee and C.-h. Lu, "SU(2) calorons and magnetic monopoles," *Phys. Rev.* **D58** (1998) 025011, `arXiv:hep-th/9802108`, `doi: 10.1103/PhysRevD.58.025011`.

[68] E.-M. Ilgenfritz, P. Gerhold, M. Müller-Preussker, B. V. Martemyanov, and A. I. Veselov, "Topological clusters in SU(2) gluodynamics at finite temperature and the evidence for KvB calorons," *PoS* **LAT2005** (2006) 306, `arXiv:hep-lat/0509171`.

[69] D. Diakonov and V. Petrov, "Confining ensemble of dyons," *Phys. Rev.* **D76** (2007) 056001, `arXiv:0704.3181 [hep-th]`, `doi: 10.1103/PhysRevD.76.056001`, URL: `http://link.aps.org/abstract/PRD/v76/e056001`.

[70] P. Gerhold, "An SU(2) KvB caloron gas model and confinement," diploma thesis, Humboldt-Universität zu Berlin, 2005, URL: `http://pha.physik.hu-berlin.de/thesis/dipl-gerhold.html`.

[71] M. Wagner, *The pseudoparticle approach in SU(2) Yang-Mills theory.* PhD thesis, Friedrich-Alexander-Universität Erlangen-Nürnberg, Schlossplatz 4, 91054 Erlangen, Germany, 2006, URL: `http://alk.physik.uni-erlangen.de/theses/data/Dis-2006-02.ps.gz`. link retrieved on 2008/05/03.

[72] M. Wagner and F. Lenz, "The pseudoparticle approach for solving path integrals in gauge theories," *PoS* **LAT2005** (2006) 315, `arXiv:hep-lat/0510083`.

[73] F. Lenz, J. W. Negele, and M. Thies, "Confinement from merons," *Phys. Rev.* **D69** (2004) 074009, `arXiv:hep-th/0306105`, `doi: 10.1103/PhysRevD.69.074009`.

[74] J. V. Steele, "Can merons describe confinement?," `arXiv:hep-lat/0007030`.

[75] J. P. Hornak, "The Basics of NMR a hypertext book on nuclear magnetic resonance spectroscopy." online hypertext, 1997, URL: `www.cis.rit.edu/htbooks/nmr`.

[76] J. P. Hornak, "The Basics of MRI, a hypertext book on magnetic resonance imaging." online hypertext, 1997, URL: `www.cis.rit.edu/htbooks/mri`.

[77] R. Penrose, "A Generalized inverse for matrices," *Proc. Cambridge Phil. Soc.* **51** (1955) 406–413.

[78] G. H. Golub and C. F. Van Loan, *Matrix Computations.* Johns Hopkins University Press, 3rd ed., 1996, ISBN 0-8018-5414-8.

[79] T. F. Chan, "An improved algorithm for computing the singular value decomposition," *ACM Transactions on Mathematical Software* **8** (1982) 72–83.

[80] M. Galassi, M. Davies, J. Theiler, B. Gough, G. Jungman, M. Booth, and F. Rossi, *GNU Scientific Library Reference Manual - Revised Second Edition.* Network Theory Limited, 15 Royal Park, Bristol BS8 3AL, United Kingdom, 2006, ISBN 0-9541617-3-4, URL: `http://www.gnu.org/software/gsl/manual/gsl-ref.ps.gz`.

[81] E. Anderson, Z. Bai, C. Bischof, S. Blackford, J. Demmel, J. Dongarra, J. D. Croz, A. Greenbaum, S. Hammarling, A. McKenney, and D. Sorensen, *LAPACK Users' Guide.* SIAM, third ed., 1999, ISBN 0-89871-447-8.

[82] O. S., L. T. M., K. A. R., and T. D. W., "Brain magnetic resonance imaging with contrast dependent on blood oxygenation," *Proceedings of the National Academy of Science of the U.S.A.* **87** (1990) 9868–9872.

[83] K. Friston, C. Frith, R. Frackowiak, and R. Turner, "Characterizing dynamic brain responses with fmri," *NeuroImage* **2** (1995) 166–172.

[84] K. Friston, W. Penny, and O. David, "Modelling brain responses," in *International Review of Neurobiology, Neuroimaging, Part A*, M. Glabus, ed. Elsevier, 2005.

[85] K. Friston, J. Ashburner, S. Kiebel, T. Nichols, and W. Penny, eds., *Statistical Parametric Mapping: The Analysis of Functional Brain Images.* Academic Press, 2007, ISBN 978-0123725608.

[86] G. Flandin and K. Friston, "Statistical parametric mapping," *Scholarpedia* **3** (2008), no. 4, 6232. URL: `http://www.scholarpedia.org/article/Statistical_parametric_mapping_(SPM)` .

[87] D. Veltman and C. Hutton, "Spm99 manual," tech. rep., Wellcome Department of Imaging Neuroscience, 2000.

[88] **QCDOC** Collaboration, P. A. Boyle, C. Jung, and T. Wettig, "The QCDOC supercomputer: Hardware, software, and performance," *ECONF* **C0303241** (2003) THIT003, `arXiv:hep-lat/0306023`.

[89] D. Chen *et al.*, "QCDOC: A 10-teraflops scale computer for lattice QCD," *Nucl. Phys. Proc. Suppl.* **94** (2001) 825–832, `arXiv:hep-lat/0011004`, `doi: 10.1016/S0920-5632(01)01014-3`.

[90] P. A. Boyle *et al.*, "QCDOC: Project status and first results," *J. Phys. Conf. Ser.* **16** (2005) 129–139, `doi: 10.1088/1742-6596/16/1/017`.

[91] M. Creutz. source code, URL: `http://thy.phy.bnl.gov/~creutz/qcdoc/mpi/`. retrieved on 2008/04/27.

[92] R. P. Woods, S. T. Grafton, C. J. Holmes, S. R. Cherry, and J. C. Mazziotta, "Automated image registration: I. General methods and intrasubject, intramodality validation," *Journal of Computer Assisted Tomography* **22** (1998) 139–152.

[93] R. P. Woods, S. T. Grafton, J. D. G. Watson, N. L. Sicotte, and J. C. Mazziotta, "Automated image registration: II. Intersubject validation of linear and nonlinear models," *Journal of Computer Assisted Tomography* **22** (1998) 153–163.

[94] M. E. Peskin and D. V. Schroeder, *An Introduction to quantum field theory.* The Advanced Book Program. Perseus Books Publishing, L.L.C., 1995, ISBN 0-201-50397-2.

List of Figures

List of Tables

Acknowledgments

Numerous people supported me during the work for this thesis in various ways, and all of them are very special to me.

I like to thank all those who supported my work: Prof. Andreas Schäfer, my advisor, for making this work possible in the first place and for many scientific discussions. Falk Bruckmann, who Laplace-filtered many configurations, for discussions on filtering and other topics. Christof Gattringer, for insights about the Chirally Improved operator. Pierre van Baal, for discussions on calorons, topology and other topics. My dear friend Jennifer Farkas, for keeping me entertained and for spotting typos. Martin Deser, for moral support. Prof. Michael Müller-Preussker and Michael Ilgenfritz as joint authors of several publications for contributing to filtering. Marc Wagner for the pseudo-particle configurations. Philipp Gerhold for providing the caloron model configurations. The DFG and BMBF for supporting my work financially. My colleagues Dieter Hierl, Niko Warkentin, Michael Hartung, Christian Hagen and Jaques Bloch for numerous discussions about physics and computers. Meinulf Göckeler, my office mate during the whole time. Prof. Tilo Wettig for discussions and a thorough introduction to parallel hardware, especially to the QCDOC. Prof. Gunnar Bali for discussions, especially about quark potentials and general relativity. Prof. Mark W. Greenlee for cooperation in the fMRI project. Roland Rutschmann for lots of help with the setup for the fMRI project. The Bezirksklinikum Regensburg for letting us use the T3 MRI scanner. Robin Heidemann from Siemens AG for setting the MRI scanner. Monika Maschek and Heidi Decock for taking care of all the administrate issues. My brothers Armin and Jochen Solbrig, for moral support. A dog named Koda for emotional comfort. Tanja Friedrich for lighten up my mood during stressful times and companionship. Finally, my mother Gerda Solbrig for financial support and being a wonderful mother.

typeset using XeLaTeX 0.996